



Unione Europea



La tua
Campania
cresce in
Europa



DI
C
Ma
PI

Dipartimento
di Ingegneria Chimica,
dei Materiali e della
Produzione Industriale
Università degli Studi
di Napoli Federico II



Ph.D. course in
Industrial product and process Engineering
Ph.D thesis

***A microfluidic platform to design crosslinked
hydrogel nanoparticles for enhanced MRI***

Coordinator:
Prof. Giuseppe Mensitieri

Candidate
Maria Russo

Supervisors:
Prof. Paolo Antonio Netti
Enza Torino, Ph.D.

TABLE OF CONTENT

BACKGROUND, AIM OF THE WORK AND MAJOR FINDINGS.....	1
REFERENCES	11
I. CHAPTER I – CONTROLLED NANOPRECIPITATION TO SYNTHESIZE HYALURONIC ACID NANOPARTICLES (HANPS) IN A MICROFLUIDIC FLOW FOCUSING SYSTEM	17
I.1 BACKGROUND	18
I.1.1 <i>Biopolymeric nanoparticles for therapy and diagnostics</i>	18
I.1.2 <i>Nanoprecipitation and advantages of microfluidic systems</i>	21
I.1.3 <i>Hydrodynamic Flow Focusing in Microfluidics</i>	27
I.1.4 <i>Aim of the Chapter 1</i>	30
I.2 CASE STUDY	31
I.2.1 <i>Experimental Section</i>	31
I.2.1.1 Materials.....	31
I.2.1.2 Microfluidic set-up for flow focusing (FF) approach.....	32
I.2.1.3 Production of Hyaluronic Acid Nanoparticles (HANPs) by nanoprecipitation in microfluidics.....	34
I.2.1.4 HANPs purification and recovery.....	34
I.2.1.5 HANPs size characterization	35
I.2.1.6 Scanning Electron Microscopy.....	36
I.2.2 <i>Results and Discussion</i>	37
I.2.2.1 Diffusive mixing time in Hydrodynamic Flow Focusing approach	37
I.2.2.2 Synthesis of Hyaluronic Acid Nanoparticles (HANPs) by Hydrodynamic Flow Focusing	39
I.2.2.3 Influence of the non solvent on the HANPs characteristics.....	40
I.2.2.4 Influence of Flow Rate Ratio and polymer concentration and on HANPs characteristics.....	41
I.2.2.5 Comparison between the traditional and microfluidic nanoprecipitation.....	48
I.2.2.6 Application of the proposed approach to additional materials...	49
I.3 CONCLUSIONS	50
I.4 REFERENCES.....	53
II. CHAPTER II - A MICROFLUIDIC PLATFORM TO CONTROL THE INTERFERENCE OF GD-DTPA IN THE DESIGN OF CROSSLINKED HYALURONIC ACID NANOPARTICLES (CHANPS) FOR MRI APPLICATION .	57

II.1	BACKGROUND	58
II.1.1	<i>Introduction</i>	58
II.1.2	<i>Aim of Chapter 2</i>	62
II.2	CASE STUDY	63
II.2.1	<i>Experimental Section</i>	63
II.2.1.1	Materials	63
II.2.1.2	Study of Gd-DTPA interference on the nanoprecipitation	64
II.2.1.3	Preparation of crosslinked Hyaluronic Acid Nanoparticles (cHANPs)	65
II.2.1.4	Fourier transform Infrared spectroscopy (FT-IR)	65
II.2.1.5	Effect of the surfactant concentrations and pH conditions on the system parameters	66
II.2.1.6	Stability and swelling behaviour of the cHANPs	66
II.2.1.7	Loading capability and Encapsulation efficiency of Gd-DTPA in cHANPs	67
II.2.1.8	Preparation and characterization of PEGylated cHANPs	68
II.2.1.9	Quantification of fluorophore concentration	69
II.2.2	<i>Results and Discussion</i>	69
II.2.2.1	Successful conditions to produce cHANPs for MRI through a Microfluidic Flow-Focusing platform	69
II.2.2.2	Interference of Gd-based Contrast Agents on the nanoprecipitation and strategies to control the flow focusing pattern	70
II.2.2.3	Crosslinking and Swelling behaviour of cHANPs	77
II.2.2.4	Loading Capability, Encapsulation Efficiency and Surface properties of Gd-loaded cHANPs	84
II.2.2.5	General observation about the interference of Gd-based CAs on Nucleation and Growth in Microfluidics	85
II.2.2.6	Simultaneous encapsulation of other agents	89
II.2.2.7	PEGylation of cHANPs	90
II.3	ANOTHER CASE STUDY: PRELIMINARY RESULTS	92
II.3.1	<i>Synthesis of PEGylated crosslinked nanoparticles by nanoprecipitation in microfluidics in a one-step manner</i>	92
II.3.2	<i>Fourier Transform Infrared (FT-IR)</i>	95
II.4	CONCLUSIONS	97
II.5	REFERENCES	98

III. CHAPTER III - GD-DTPA LOADED CHANPS FOR ENHANCED IN VITRO AND IN VIVO MRI ANALYSIS 101

III.1	BACKGROUND	102
-------	------------------	-----

III.1.1	Introduction.....	102
III.1.2	Aim of Chapter 3	105
III.2	CASE STUDY	106
III.2.1	Experimental Section.....	106
III.2.1.1	Materials.....	106
III.2.1.2	In vitro cytotoxicity.....	107
III.2.1.3	In vitro MRI.....	107
III.2.1.4	Sorption of Gd-DTPA	109
III.2.1.5	In vitro stability in plasma	110
III.2.1.6	Quantification of carboxyl groups on the surface of cHANPs....	110
III.2.1.7	Direct conjugation with PEG-NH ₂ -Dye.....	111
III.2.1.8	Indirect conjugation streptavidin-biotin-peptide	111
III.2.1.9	Direct conjugation with peptide.....	112
III.2.1.10	Quantification of PEG concentration	112
III.2.1.11	BCA assay	113
III.2.1.12	In vivo MRI	113
III.2.2	Results and Discussion.....	116
III.2.2.1	In vitro cytotoxicity.....	116
III.2.2.2	In vitro MRI.....	118
III.2.2.3	Sorption of Gd-DTPA	125
III.2.2.4	Direct conjugation with PEG-NH ₂ -dye	126
III.2.2.5	Direct conjugation with peptide pA20-36	129
III.2.2.6	Indirect conjugation with peptide pA20-36.....	129
III.2.2.7	Toxicity study in vivo	130
III.2.2.8	In vivo MRI.....	130
III.2.2.9	In vivo biodistribution study.....	137
III.3	ANOTHER CASE STUDY.....	139
III.3.1	In vitro MRI of Gd-loaded PEGylated cHANPs	139
III.4	CONCLUSIONS	140
III.5	REFERENCES.....	142

IV. CHAPTER IV - IMPACT OF BIOPOLYMER MATRICES ON RELAXOMETRIC PROPERTIES OF CONTRAST AGENTS: THE DEFINITION OF HYDRODENTICITY

IV.1	BACKGROUND	148
IV.1.1	Introduction.....	148
IV.1.2	Aim of Chapter 4	150
IV.2	CASE STUDY.....	153
IV.2.1	Experimental Section.....	153
IV.2.1.1	Materials.....	153

IV.2.1.2	Sample preparation	153
IV.2.1.3	Water self-diffusion coefficient	154
IV.2.1.4	Isothermal Titration Calorimetry	154
IV.2.1.5	Relaxometric measurement.....	155
IV.2.1.6	Swelling Ratio and Hydrogel parameters	155
<i>IV.2.2</i>	<i>Results and Discussion.....</i>	<i>156</i>
IV.2.2.1	Diffusion Coefficient	156
IV.2.2.2	Isothermal Titration Calorimetry	160
IV.2.2.3	Time-Domain Relaxometry	163
IV.2.2.4	Theoretical interpretation of the enhanced Relaxivity	168
IV.2.2.5	Study of hydrogel structural parameters enhancing relaxometric properties of Gd-based CAs within cHANPs	172
IV.2.2.6	Definition of Hydrodenticity as a property referring to the Hydrogels/Gd-based CAs interaction	178
IV.3	CONCLUSIONS	181
IV.4	REFERENCES.....	184
MAIN CONCLUSIONS AND PERSPECTIVES		191
V.	APPENDIX.....	196
V.1	ICP-MS RESULTS.....	196
V.2	CALCULATIONS OF THE HYDROGEL NETWORK PARAMETERS	201
V.3	REFERENCES.....	207
LIST OF ABBREVIATIONS		208
COMMUNICATIONS TO CONGRESS/CONFERENCES:		210
PUBLICATIONS ALONG THREE YEARS.....		212
PROJECT ACTIVITIES.....		214
COLLABORATIONS		215
OTHER ACTIVITIES		216

Background, Aim of the work and Major Findings

Nowadays, medical imaging techniques play a central role in clinical diagnoses and the follow-up after treatment, particularly in an oncological context. Magnetic Resonance Imaging (MRI) is a routinely applied diagnostic imaging tool because of its not invasive nature and its ability to obtain three-dimensional tomographical information of soft tissues. Furthermore, it can be used for visualizing functions of cardiac, brain, and central nervous system, as well as detecting tumor¹⁻³.

However, this technique suffers from the lack of sensitivity and information obtained from a simple unenhanced MR image and, consequently, more than 35% of all clinical MRI scans utilize Contrast Agents (CAs)⁴ to improve these aspects by selectively relaxing the water molecules near the complex. Commonly available MRI CAs come from paramagnetic compounds as gadolinium (Gd^{3+}) chelates^{3,5} and superparamagnetic iron oxide (SPIO) conjugates, a nanoparticulate MRI probe^{6,7}. For Gd-based CAs, they enhance the signal in T_1 -weighted images, otherwise SPIO conjugates provide a strong contrast effect in T_2 -weighted images. T_1 -weighted MRI CAs utilize paramagnetic metal ions to enhance the contrast in an MR image by positively influencing the relaxation rates of water protons in the immediate surroundings of the tissue in which they localize. The ability of CAs to effectively enhance image contrast depends on their relaxivity (longitudinal r_1 ; transversal r_2) and

the level of accumulation at the target site⁸. The relaxivity is defined as the rate of change in relaxation times of the water protons per mM concentration of metal ions. Larger is the relaxivity of a given CA, larger will be the induced relaxation time (T_1 , T_2) shortening. In details, spin-lattice relaxation time T_1 and spin-spin relaxation time T_2 may be shortened considerably in presence of paramagnetic species. While shortening of T_1 leads to increase in signal intensity, shortening of T_2 produces broader lines with decreased intensity. The net result is a nonlinear relationship between signal intensity and the concentration of the CAs. Indeed, at low concentrations, an increase of the amount of the CA provides an increase in signal intensity due to effect on T_1 until the optimal concentration is reached. However, a further increase in concentration reduces the signal because of effect on T_2 producing a negative contrast effect. This peculiar behavior dictates their use in clinical practice, preferring CAs that have a relatively greater effect on T_1 than on T_2 .

In these perspectives, the possibility to have a CA that could work at low concentration but without giving over its signal intensity and, therefore, positive contrast effect is of great interest.

Among different CAs, Gd chelates based ones, owing to its enhanced stability and paramagnetic properties, are used in up to 30% of clinical MRI scans and are considered clinically approved for human use.

However, their effectiveness remains limited owing to nephrotoxicity effects⁹, lack of tissue specificity, low relaxivity, short in vivo circulation time and poor specificity which restraints its application. Furthermore, McDonald et al.¹⁰ have recently reported results about progressive Gd deposition in various central nervous system after repeated intravenous administration of CAs, even if these signal intensity changes are not specific and can be seen with several other pathologic conditions.

In effect, Food and Drug Administration (FDA) has alarmed the medical community and has recommended the health care professionals to limit the use of Gd-based CAs unless necessary, with potential negative impact on the early diagnosis of several pathologies. Despite the valuable role of the CAs for MRI, this case history confirms the need to build up a biocompatible system with higher relaxivity able to protect the chelate around Gd ions from transmetallation phenomena and control the accumulation and the clearance of the Gd-based CAs in a specific organ.¹¹⁻¹⁵

The effectiveness of a Gd-chelate as an MRI CA is usually assessed in vitro by measuring the corresponding relaxivity r_1 and r_2 . As stated by Solomon–Bloembergen-Morgan (SBM) theory,^{16,17} high relaxivity can be achieved by fine and accurate control of the characteristic

parameters that regulate the dipolar interaction between water protons and Gd-based CAs:¹⁸ the number of water molecules (q) in the Inner Sphere (IS), i.e. those present in the coordination sites of the Gd ion, and their residence lifetime (τ_M); the rotational correlation time of the metal complex (τ_R); the diffusion correlation time (τ_D) of the water molecules in the Outer Sphere (OS), i.e. those diffusing nearby the metal complex.

According to these parameters and by exploiting the versatile properties of nano- and bio-materials^{19,20}, several nanostructured CAs with enhanced relaxivity have been investigated.²¹⁻²⁶

In particular, nanoparticle-based T_1 -weighted MRI CAs can be classified as 1) Gd-chelate grafted organic/inorganic nanoparticles^{22,27,28}; 2) nanoparticles encapsulating Gd^{27,29,30}; 3) Gd-based unusual nanometer-sized architectures, such as dendrimers and micelles³¹⁻³⁶. Among these classes, grafting of metal nanoparticles with Gd³⁺ chelates reach values of $r_1 \sim 60 \text{ mM}^{-1}\text{s}^{-1}$ at 1.5T^{37,38}, although their colloidal stability and toxicity are still a challenge³⁹⁻⁴⁴. However, attempts to exploit “rigidification”⁴⁵ and “confinement”⁸ of metal chelates seem to be the most effectiveness to enhance the effect of Gd-based CAs without the chemical modification of the chelate, compared to other strategies based on bio-conjugation or encapsulation⁴⁶.

Research focusing on polymeric hybrid nanosystems, nanoparticles, nanospheres and nanocapsules, for bioengineering, nanomedicine and

theranostic applications has undergone drastic transformations in the past few decades. The interest of these nanosystems particularly relies on the new dimensions and new potentials they offered regarding their enhanced interactions with micro- or macro-environments due to a higher available surface-volume ratio of the nanostructure. In fact, they are able to penetrate living tissues, and encapsulate, protect and deliver the drug into specific targeted sites. In addition, nanocarriers can also be used to stabilize CAs with poor aqueous solubility⁴⁷. Furthermore, systems with monodisperse size under 100 nm are likely to improve delivery functions⁴⁸ to the tissues, stability of the metal chelates, and also provide enhanced relaxometric properties of the Gd-based CAs. In fact, it is also highly interesting to have monodisperse size of core material, which is one of the most important parameters for imaging⁴⁹. Conventionally, for example, SPIO are produced by the solution-phase chemical reduction of ionic iron precursors, which often results in the formation of polydispersed and poorly crystalline iron oxide nanoparticles with inferior magnetic properties⁵⁰. For polymeric nanoparticles encapsulating or conjugating CAs, the main ways to produce are solvent evaporation, salting-out, emulsification, solvent diffusion process, supercritical fluids that replace the solvent in the precipitation techniques, polymerization, and nanoprecipitation^{51,52}. Among several techniques, nanoprecipitation represents a very powerful approach to produce polymeric nanoparticles in batch processes⁵³ even if polydispersity due to

aggregation effects challenges in the complete removal of the solvents, in particular for high polymer–solvent affinities, and low loadings of hydrophilic compounds⁵⁴. Indeed, the inherent variability and complexity of conventional batch precipitation processes often make it problematic to produce particles with well-defined physicochemical and functional attributes^{52,53}.

To circumvent this issue to obtain high-quality MRI imaging, different procedures for producing size- and shape-controlled nanoparticles are being explored. Microfluidics has demonstrated its ability to improve size- and composition- control in the field of nanoparticle synthesis^{55,56}. Microfluidic technologies are adapted to tightly control the nanoprecipitation, the mixing rate between solvent and non-solvent phase, and clearly showed advantageous results in term of the final particle properties, i.e. size, polydispersity, etc., due to the process's ability to accurately control process parameters and thus enables efficient, continuous and tunable mixing^{55,57-62}.

As dominantly used core materials in MRI contrast agents, SPIO have been prepared by continuous flow microfluidic devices⁶³. Such microfluidic platforms could have the potential to profoundly improve development of MRI-based molecular imaging CAs.

But, even if, in the recent years, a great effort has been made to apply microfluidic technologies to the production of SPIO for MRI and to the production of polymeric nanoparticles for other applications, the

exploitation of the microfluidic approaches to support the design of hydrogel nanostructures for MRI is still lacking.

Recently, in our work published on *Interface Focus* “*Impact of biopolymer matrices on relaxometric properties of contrast agents*”⁶⁴, we have explored the impact of crosslinked and un-crosslinked biopolymer matrices on relaxometric properties of CAs where the contribution to the enhancement of CAs is highlighted and attributed to the reduced mobility of water within the hydrogel. The proposed approach for characterizing polymer-based CAs could be applied to study the mechanisms involved in several combinations of different types of polymers and metal ions.

The idea is that the knowledge of these complex systems could be scaled to nanoscale dimensions, inspiring the development of a new class of nanostructured MRI CAs with highly tunable relaxometric properties.

Moreover, the possibility to modulate the properties of the nanoparticles through a microfluidic system to impact the relaxometric properties of the CAs without chemical modification of the chelates has not been tested^{55,65,66} and could be investigated to obtain a new class of MRI approaches based on rational polymer nanostructures.

In these perspectives, in another work recently published by *Scientific Reports* “*A Microfluidic Platform to design crosslinked Hyaluronic Acid Nanoparticles (cHANPs) for enhanced MRI*”⁶⁷, a controlled

nanoprecipitation in a microfluidic flow focusing approach is used to synthesize intravascularly-injectable and biocompatible hydrogel nanoparticles as low as 35 nm in which a clinically relevant MRI-CAs, Gd-DTPA, is entrapped. By fine-tuning the mixing of all species, nanoprecipitation behaviour and crosslinking reaction are adjusted very precisely simultaneously, leading to relaxivity values about 12 times larger than that of free CAs clinically available, at the common field of clinical MRI, 1.5 Tesla. This approach is optimized to perform a crosslinking reaction able to retain the Gd-CAs in the polymer matrix of the precipitated morphology. The proposed methodology has the goal to introduce microfluidic strategies to modulate the nanoprecipitation playing on the hydrophilic-lipophilic properties of the surfactants or the pH solution conditions to optimize relaxometric performances of the MRI CAs.

A multidisciplinary study of the interference of the Gd-DTPA in the polymer conformation is reported for the first time and could add significant advances to the fundamental knowledge of the interaction between the Gd-chelates and hydrogels structures.

The developed microfluidic strategies allow a fine tuning of the hydrogel structure, and it can be easily applied to different polymer and materials involved in nanomedicine field. Additional strengths of the proposed work, compared to the other investigations related to the formation of nanostructures, are also the achieved nanoparticles size

of 35 nm and the low polydispersity, as so the controlled degradation and release behaviors.

Preliminary in vivo results clearly show the improvement of the MRI and confirm the stability of NPs ensuring no leakage of Gd-DTPA during the time course of the relaxation measurements. Gd-entrapped cHANPs could potentially provide tissue specificity and reduce nephrotoxicity and, at the same time, they have the capability to retain Gd-based contrast agents to boost the MR signal without the chemical modification of the chelates. Furthermore, cHANPs could ensure an improvement of the time window for clinical imaging acquisitions due to the reduction of long scan time and rapid renal clearance.

Starting from the observation of a peculiar swelling behavior and in vitro relaxometric properties of the cHANPs, we have also proposed an explanation of how the hydrogel structural parameters can be used to improve the relaxometric properties of CAs.

In our last work under revision “*Hydrodenticity to enhance relaxivity of Gd-DTPA within crosslinked Hyaluronic Acid Nanoparticles (cHANPs)*”, we report how the water dynamics in a hydrogel matrix can interfere with the relaxation properties of the Gd-based CAs irrespective of NPs size or way of production. For the first time, the new concept of Hydrodenticity is here defined to intend the peculiar environment within the nanostructures composed by the ternary system, hydrogel/water/CAs able to improve the relaxometric properties. Parameters related to the hydrodenticity are individuated

and explained, supported by the literature, and a theoretical explanation is fully provided by the consolidated Flory-Rhener theory. In this case, the microfluidics is not the main actor but the approach, as presented in the Chapter I, becomes a tool to prove that Hydrodenticity can be modulated to obtain desired crosslink density, mesh size, hydrophilicity and loading capability, playing on the biodegradable behavior and relaxometric properties of the Gd-loaded nanostructures. In this work, Hydrodenticity refers to the status of the hydrated Gd-DTPA with the coordination water subjected to osmotic pressure deriving from elastodynamics equilibrium of swollen gels. The capability to control these parameters within the nanoparticles can be applied to define a new class of medical devices useful to improve the properties of CAs for MRI.

We firmly believe that our findings could lead to direct benefits of the clinical field due to the utilization and improvement of completely biocompatible and FDA approved products without their chemical modifications, the ease of the synthesis, the nature of the materials, and the scalability of the proposed process, as reported in the next Chapters.

References

- 1 Caravan, P. Strategies for increasing the sensitivity of gadolinium based MRI contrast agents. *Chemical Society Reviews* **35**, 512-523, doi:10.1039/b510982p (2006).
- 2 Mansfield, P. Snapshot magnetic resonance imaging (nobel lecture). *Angewandte Chemie-International Edition* **43**, 5456-5464, doi:10.1002/anie.200460078 (2004).
- 3 Caravan, P., Ellison, J. J., McMurry, T. J. & Lauffer, R. B. Gadolinium(III) chelates as MRI contrast agents: Structure, dynamics, and applications. *Chemical Reviews* **99**, 2293-2352, doi:10.1021/cr980440x (1999).
- 4 Xue, S. H., Qiao, J. J., Pu, F., Cameron, M. & Yang, J. J. Design of a novel class of protein-based magnetic resonance imaging contrast agents for the molecular imaging of cancer biomarkers. *Wiley Interdisciplinary Reviews-Nanomedicine and Nanobiotechnology* **5**, 163-179, doi:10.1002/wnan.1205 (2013).
- 5 Na, H. B., Song, I. C. & Hyeon, T. Inorganic Nanoparticles for MRI Contrast Agents. *Advanced Materials* **21**, 2133-2148, doi:10.1002/adma.200802366 (2009).
- 6 Weissleder, R. *et al.* SUPERPARAMAGNETIC IRON-OXIDE - ENHANCED DETECTION OF FOCAL SPLENIC TUMORS WITH MR IMAGING. *Radiology* **169**, 399-403 (1988).
- 7 Weissleder, R., Reimer, P., Lee, A. S., Wittenberg, J. & Brady, T. J. MR RECEPTOR IMAGING - ULTRASMALL IRON-OXIDE PARTICLES TARGETED TO ASIALOGLYCOPROTEIN RECEPTORS. *American Journal of Roentgenology* **155**, 1161-1167 (1990).
- 8 Sethi, R. *et al.* Enhanced MRI relaxivity of Gd³⁺-based contrast agents geometrically confined within porous nanoconstructs. *Contrast Media & Molecular Imaging* **7**, 501-508, doi:10.1002/cmml.1480 (2012).
- 9 Penfield, J. G. & Reilly, R. F., Jr. What nephrologists need to know about gadolinium. *Nature Clinical Practice Nephrology* **3**, 654-668, doi:10.1038/ncpneph0660 (2007).
- 10 McDonald, R. J. *et al.* Intracranial Gadolinium Deposition after Contrast-enhanced MR Imaging. *Radiology* **275**, 772-782, doi:10.1148/radiol.15150025 (2015).
- 11 Veisheh, O. *et al.* Specific Targeting of Brain Tumors with an Optical/Magnetic Resonance Imaging Nanoprobe across the Blood-Brain Barrier. *Cancer Res.* **69**, 6200-6207, doi:10.1158/0008-5472.can-09-1157 (2009).
- 12 Kircher, M. F. *et al.* A brain tumor molecular imaging strategy using a new triple-modality MRI-photoacoustic-Raman nanoparticle. *Nat. Med.* **18**, 829-U235, doi:10.1038/nm.2721 (2012).

- 13 Chertok, B. *et al.* Iron oxide nanoparticles as a drug delivery vehicle for MRI monitored magnetic targeting of brain tumors. *Biomaterials* **29**, 487-496, doi:10.1016/j.biomaterials.2007.08.050 (2008).
- 14 Cole, A. J., David, A. E., Wang, J., Galban, C. J. & Yang, V. C. Magnetic brain tumor targeting and biodistribution of long-circulating PEG-modified, cross-linked starch-coated iron oxide nanoparticles. *Biomaterials* **32**, 6291-6301, doi:10.1016/j.biomaterials.2011.05.024 (2011).
- 15 Kabiri, M. & Unsworth, L. D. Application of Isothermal Titration Calorimetry for Characterizing Thermodynamic Parameters of Biomolecular Interactions: Peptide Self-Assembly and Protein Adsorption Case Studies. *Biomacromolecules* **15**, 3463-3473, doi:10.1021/bm5004515 (2014).
- 16 Solomon, I. Relaxation processes in a system of two spins. *Physical Review* **99**, 559 (1955).
- 17 Bloembergen, N. Proton relaxation times in paramagnetic solutions. *The Journal of Chemical Physics* **27**, 572-573 (1957).
- 18 Xue, S., Qiao, J., Pu, F., Cameron, M. & Yang, J. J. Design of a novel class of protein-based magnetic resonance imaging contrast agents for the molecular imaging of cancer biomarkers. *Wiley Interdisciplinary Reviews-Nanomedicine and Nanobiotechnology* **5**, 163-179, doi:10.1002/wnan.1205 (2013).
- 19 Boccaccini, A. R., Keim, S., Ma, R., Li, Y. & Zhitomirsky, I. Electrophoretic deposition of biomaterials. *Journal of the Royal Society Interface* **7**, S581-S613, doi:10.1098/rsif.2010.0156.focus (2010).
- 20 Chavez-Valdez, A. *et al.* TiO₂-PLLA nanocomposite coatings and free-standing films by a combined electrophoretic deposition-dip coating process. *Composites Part B-Engineering* **67**, 256-261, doi:10.1016/j.compositesb.2014.07.001 (2014).
- 21 Huang, M., Huang, Z. L., Bilgen, M. & Berkland, C. Magnetic resonance imaging of contrast-enhanced polyelectrolyte complexes. *Nanomedicine-Nanotechnology Biology and Medicine* **4**, 30-40, doi:10.1016/j.nano.2007.10.085 (2008).
- 22 Rotz, M. W. *et al.* High Relaxivity Gd(III) - DNA Gold Nanostars: Investigation of Shape Effects on Proton Relaxation. *Acs Nano* **9**, 3385-3396, doi:10.1021/nn5070953 (2015).
- 23 Wang, Z. T. *et al.* Water-soluble amorphous iron oxide nanoparticles synthesized by a quickly pestling and nontoxic method at room temperature as MRI contrast agents. *Chemical Engineering Journal* **235**, 231-235, doi:10.1016/j.cej.2013.09.042 (2014).
- 24 Wang, G. S., Ma, Y. Y., Wei, Z. Y. & Qi, M. Development of multifunctional cobalt ferrite/graphene oxide nanocomposites for magnetic resonance imaging and controlled drug delivery. *Chemical Engineering Journal* **289**, 150-160, doi:10.1016/j.cej.2015.12.072 (2016).
- 25 Lakshmanan, S., Holmes, W. M., Sloan, W. T. & Phoenix, V. R. Nanoparticle transport in saturated porous medium using magnetic

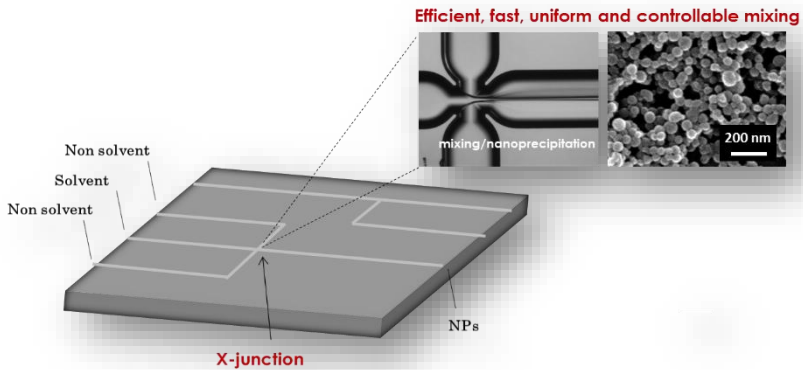
- resonance imaging. *Chemical Engineering Journal* **266**, 156-162, doi:10.1016/j.cej.2014.12.076 (2015).
- 26 Ma, L. L. *et al.* Small Multifunctional Nanoclusters (Nanoroses) for Targeted Cellular Imaging and Therapy. *Acs Nano* **3**, 2686-2696, doi:10.1021/nn900440e (2009).
- 27 Zhu, D., Liu, F., Ma, L., Liu, D. & Wang, Z. Nanoparticle-Based Systems for T-1-Weighted Magnetic Resonance Imaging Contrast Agents. *International Journal of Molecular Sciences* **14**, 10591-10607, doi:10.3390/ijms140510591 (2013).
- 28 Sandiford, L. *et al.* Bisphosphonate-Anchored PEGylation and Radiolabeling of Superparamagnetic Iron Oxide: Long-Circulating Nanoparticles for in Vivo Multimodal (T1 MRI-SPECT) Imaging. *Acs Nano* **7**, 500-512, doi:10.1021/nn3046055 (2013).
- 29 Chen, K. J. *et al.* A small MRI contrast agent library of gadolinium(III)-encapsulated supramolecular nanoparticles for improved relaxivity and sensitivity. *Biomaterials* **32**, 2160-2165, doi:10.1016/j.biomaterials.2010.11.043 (2011).
- 30 Santra, S. *et al.* Gadolinium-encapsulating iron oxide nanoprobe as activatable NMR/MRI contrast agent. *ACS nano* **6**, 7281-7294 (2012).
- 31 Felton, C. *et al.* Magnetic nanoparticles as contrast agents in biomedical imaging: recent advances in iron- and manganese-based magnetic nanoparticles. *Drug Metabolism Reviews* **46**, 142-154 (2014).
- 32 Kim, T. *et al.* Mesoporous Silica-Coated Hollow Manganese Oxide Nanoparticles as Positive T-1 Contrast Agents for Labeling and MRI Tracking of Adipose-Derived Mesenchymal Stem Cells. *Journal of the American Chemical Society* **133**, 2955-2961, doi:10.1021/ja1084095 (2011).
- 33 Xu, W. *et al.* Paramagnetic nanoparticle T-1 and T-2 MRI contrast agents. *Physical Chemistry Chemical Physics* **14**, 12687-12700, doi:10.1039/c2cp41357d (2012).
- 34 Cheng, Z. L., Thorek, D. L. J. & Tsourkas, A. Gadolinium-Conjugated Dendrimer Nanoclusters as a Tumor-Targeted T-1 Magnetic Resonance Imaging Contrast Agent. *Angewandte Chemie-International Edition* **49**, 346-350, doi:10.1002/anie.200905133 (2010).
- 35 Huang, C. H., Nwe, K., Al Zaki, A., Brechbiel, M. W. & Tsourkas, A. Biodegradable Polydisulfide Dendrimer Nanoclusters as MRI Contrast Agents. *Acs Nano* **6**, 9416-9424, doi:10.1021/nn304160p (2012).
- 36 Park, J. H. *et al.* Hyaluronic acid derivative-coated nanohybrid liposomes for cancer imaging and drug delivery. *Journal of Controlled Release* **174**, 98-108, doi:10.1016/j.jconrel.2013.11.016 (2014).
- 37 Ferreira, M. F. *et al.* Gold nanoparticles functionalised with stable, fast water exchanging Gd³⁺ chelates as high relaxivity contrast agents for MRI. *Dalton Transactions* **41**, 5472-5475, doi:10.1039/c2dt30388d (2012).
- 38 Lartigue, L. *et al.* Cooperative Organization in Iron Oxide Multi-Core Nanoparticles Potentiates Their Efficiency as Heating Mediators and MRI

- Contrast Agents. *Acs Nano* **6**, 10935-10949, doi:10.1021/nn304477s (2012).
- 39 Chen, R. *et al.* Parallel Comparative Studies on Mouse Toxicity of Oxide Nanoparticle- and Gadolinium-Based T1 MRI Contrast Agents. *Acs Nano* **9**, 12425-12435, doi:10.1021/acsnano.5b05783 (2015).
- 40 Di Corato, R. *et al.* High-Resolution Cellular MRI: Gadolinium and Iron Oxide Nanoparticles for in-Depth Dual-Cell Imaging of Engineered Tissue Constructs. *Acs Nano* **7**, 7500-7512, doi:10.1021/nn401095p (2013).
- 41 Huang, J. *et al.* Effects of Nanoparticle Size on Cellular Uptake and Liver MRI with Polyvinylpyrrolidone-Coated Iron Oxide Nanoparticles. *Acs Nano* **4**, 7151-7160, doi:10.1021/nn101643u (2010).
- 42 Lee, G. Y. *et al.* Theranostic Nanoparticles with Controlled Release of Gemcitabine for Targeted Therapy and MRI of Pancreatic Cancer. *Acs Nano* **7**, 2078-2089, doi:10.1021/nn3043463 (2013).
- 43 Sancey, L. *et al.* Long-Term in Vivo Clearance of Gadolinium-Based AGuIX Nanoparticles and Their Biocompatibility after Systemic Injection. *Acs Nano* **9**, 2477-2488, doi:10.1021/acsnano.5b00552 (2015).
- 44 Zhou, Z. *et al.* Surface and Interfacial Engineering of Iron Oxide Nanoplates for Highly Efficient Magnetic Resonance Angiography. *Acs Nano* **9**, 3012-3022, doi:10.1021/nn507193f (2015).
- 45 Port, M. *et al.* Impact of rigidification on relaxometric properties of a tricyclic tetraazatriacetic gadolinium chelate. *Contrast Media & Molecular Imaging* **1**, 121-127, doi:10.1002/cmmi.99 (2006).
- 46 Courant, T. *et al.* Hydrogels Incorporating GdDOTA: Towards Highly Efficient Dual T1/T2 MRI Contrast Agents. *Angewandte Chemie-International Edition* **51**, 9119-9122, doi:10.1002/anie.201203190 (2012).
- 47 Anton, N. *et al.* A new microfluidic setup for precise control of the polymer nanoprecipitation process and lipophilic drug encapsulation. *Soft Matter* **8**, 10628-10635, doi:10.1039/c2sm25357g (2012).
- 48 Mitragotri, S. & Lahann, J. Physical approaches to biomaterial design. *Nature Materials* **8**, 15-23, doi:10.1038/nmat2344 (2009).
- 49 Yoo, B. & Pagel, M. D. An overview of responsive MRI contrast agents for molecular imaging. *Frontiers in Bioscience-Landmark* **13**, 1733-1752, doi:10.2741/2796 (2008).
- 50 Lu, A. H., Salabas, E. L. & Schuth, F. Magnetic nanoparticles: Synthesis, protection, functionalization, and application. *Angewandte Chemie-International Edition* **46**, 1222-1244, doi:10.1002/anie.200602866 (2007).
- 51 Fessi, H., Puisieux, F., Devissaguet, J. P., Ammoury, N. & Benita, S. NANOCAPSULE FORMATION BY INTERFACIAL POLYMER DEPOSITION FOLLOWING SOLVENT DISPLACEMENT. *International Journal of Pharmaceutics* **55**, R1-R4, doi:10.1016/0378-5173(89)90281-0 (1989).
- 52 Mora-Huertas, C. E., Fessi, H. & Elaissari, A. Polymer-based nanocapsules for drug delivery. *International Journal of Pharmaceutics* **385**, 113-142, doi:10.1016/j.ijpharm.2009.10.018 (2010).

- 53 Schubert, S., Delaney, J. T., Jr. & Schubert, U. S. Nanoprecipitation and nanoformulation of polymers: from history to powerful possibilities beyond poly(lactic acid). *Soft Matter* **7**, 1581-1588, doi:10.1039/c0sm00862a (2011).
- 54 Quintanar-Guerrero, D., Allemann, E., Doelker, E. & Fessi, H. Preparation and characterization of nanocapsules from preformed polymers by a new process based on emulsification-diffusion technique. *Pharmaceutical Research* **15**, 1056-1062 (1998).
- 55 Karnik, R. *et al.* Microfluidic platform for controlled synthesis of polymeric nanoparticles. *Nano Letters* **8**, 2906-2912, doi:10.1021/nl801736q (2008).
- 56 Capretto, L. *et al.* Mechanism of co-nanoprecipitation of organic actives and block copolymers in a microfluidic environment. *Nanotechnology* **23**, 16, doi:10.1088/0957-4484/23/37/375602 (2012).
- 57 Knopp, E. A. & Cowper, S. E. Nephrogenic systemic fibrosis: Early recognition and treatment. *Seminars in Dialysis* **21**, 123-128, doi:10.1111/j.1525-139X.2007.00399.x (2008).
- 58 Lim, J. M. *et al.* Parallel microfluidic synthesis of size-tunable polymeric nanoparticles using 3D flow focusing towards in vivo study. *Nanomedicine-Nanotechnology Biology and Medicine* **10**, 401-409, doi:10.1016/j.nano.2013.08.003 (2014).
- 59 Lim, J.-M. *et al.* Ultra-High Throughput Synthesis of Nanoparticles with Homogeneous Size Distribution Using a Coaxial Turbulent Jet Mixer. *ACS Nano* **8**, 6056-6065, doi:10.1021/nn501371n (2014).
- 60 Lazarus, L. L., Yang, A. S. J., Chu, S., Brutchey, R. L. & Malmstadt, N. Flow-focused synthesis of monodisperse gold nanoparticles using ionic liquids on a microfluidic platform. *Lab on a Chip* **10**, 3377-3379, doi:10.1039/c0lc00297f (2010).
- 61 Conde, A. J. *et al.* Continuous flow generation of magnetoliposomes in a low-cost portable microfluidic platform. *Lab on a Chip* **14**, 4506-4512, doi:10.1039/c4lc00839a (2014).
- 62 Herranz-Blanco, B. *et al.* Microfluidic assembly of multistage porous silicon-lipid vesicles for controlled drug release. *Lab on a Chip* **14**, 1083-1086, doi:10.1039/c3lc51260f (2014).
- 63 Weng, C. H., Huang, C. C., Yeh, C. S., Lei, H. Y. & Lee, G. B. Synthesis of hollow, magnetic Fe/Ga-based oxide nanospheres using a bubble templating method in a microfluidic system. *Microfluidics and Nanofluidics* **7**, 841-848, doi:10.1007/s10404-009-0442-5 (2009).
- 64 Ponsiglione, A. M., Russo, M., Netti, P. A. & Torino, E. Impact of biopolymer matrices on relaxometric properties of contrast agents. *Interface Focus* **6**, 20160061 - 20160061, doi:http://dx.doi.org/10.1098/rsfs.2016.0061 (2016).
- 65 Capretto, L., Carugo, D., Mazzitelli, S., Nastruzzi, C. & Zhang, X. Microfluidic and lab-on-a-chip preparation routes for organic nanoparticles and vesicular systems for nanomedicine applications. *Advanced Drug Delivery Reviews* **65**, 1496-1532, doi:10.1016/j.addr.2013.08.002 (2013).

- 66 Souza Bicudo, R. C. & Andrade Santana, M. H. Production of hyaluronic acid (HA) nanoparticles by a continuous process inside microchannels: Effects of non-solvents, organic phase flow rate, and HA concentration. *Chemical Engineering Science* **84**, 134-141, doi:10.1016/j.ces.2012.08.010 (2012).
- 67 Russo, M., Bevilacqua, P., Netti, P. A. & Torino, E. A Microfluidic Platform to design crosslinked Hyaluronic Acid Nanoparticles (cHANPs) for enhanced MRI. *Scientific Reports* **6**, 37906, doi:10.1038/srep37906 <http://www.nature.com/articles/srep37906#supplementary-information> (2016).

I. CHAPTER I – Controlled nanoprecipitation to synthesize Hyaluronic Acid Nanoparticles (HANPs) in a microfluidic Flow Focusing system



Graphical Abstract I-1. Efficient, fast, uniform and controllable mixing to produce Hyaluronic Acid Nanoparticles (HANPs) through nanoprecipitation in a microfluidic system.

Abstract

A new microfluidic-based process is presented to synthesize Hyaluronic Acid Nanoparticles for potential application in diagnosis and therapy. A controlled nanoprecipitation in a flow focusing configuration is used to allow a continuous and controlled production of nanoparticles, overcoming the limits of common batch processes, and guaranteeing an instantaneous formulation and absence of purification step. By fine-tuning the mixing of all species and the processing parameters, nanoprecipitation behavior is adjusted very precisely to obtain a monodisperse collection of Hyaluronic Acid Nanoparticles under 50 nm. Furthermore, the solvent and the non solvent flow rates can be varied to adjust nanoparticles properties, opening new possibilities for nanoparticle production by nanoprecipitation.

I.1 Background

I.1.1 Biopolymeric nanoparticles for therapy and diagnostics

Over the past decade, a growing interest has been dedicated on polymeric nanoparticles (NPs) for application in therapy and diagnosis to treat different types of diseases¹. Compared with conventional drug/agents vehicles, such as liposomes or micelles, polymeric NPs have been shown to increase the stability of drugs and to control their release properties, owing to their tailored sizes, morphologies, and the possibility to use biodegradable polymers^{2,3}.

Polymeric nanoparticles are defined as particulate dispersions or solid particles with a size in the range of 10-200 nm⁴. There has been a considerable research interest in drug delivery using particulate delivery systems as carriers for small and large molecules. Particulate systems like nanoparticles have been used as a physical approach to alter and improve the pharmacokinetic and pharmacodynamic properties of various types of drug molecules. Several methods to prepare polymeric nanoparticles have been developed and classified according to whether the particle formation involves a polymerization reaction or nanoparticles form directly from a macromolecule or preformed polymer^{5,6}.

Polymers used in the preparation of nanoparticles should be compatible with the body in terms of adaptability (nontoxicity and nonantigenic) and should be biodegradable and biocompatible.

Natural polymers used include chitosan, gelatin, sodium alginate, albumin, hyaluronic acid. There are also many Synthetic polymers for example Polylactides (PLA), Polyglycolides (PGA), Polylactide co-glycolides (PLGA), Polyanhydrides, Polyorthoesters, Poly glutamic acid, Poly malic acid, Poly(methyl methacrylate), Poly(vinyl alcohol), Poly(acrylic acid), Poly acrylamide, Poly(ethylene glycol), Poly(methacrylic acid)⁷.

The properties of polymeric NPs must be optimized depending on the application. In order to achieve the properties of interest, the mode of preparation plays a key role. Thus, it is highly advantageous to choose techniques to obtain polymeric NPs with the desired properties for a particular application. The main experimental ways for generating polymeric NPs can be namely listed as: solvent evaporation, salting-out, emulsification-solvent diffusion process, supercritical fluids that replace the solvent in the precipitation techniques, polymerization, and nanoprecipitation.

Among several biopolymer-based batch processes, it has been already reported that nanoprecipitation represents a very promising and powerful approach in producing nanoparticles⁸ since it is a simple, fast, and reproducible method, and also widely used to produce NPs. Polymeric and pure drug NPs were first prepared through nanoprecipitation by Fessi and coworkers².

The main principle driving the process is a fast mixing of a material solution (polymer and/or pure drug/contrast agents in a solvent) with

a non-solvent of the material. Herein, ideally, the solvent should be miscible with the non-solvent. The structure material (i.e. polymer and/or drug) should be free-soluble in the solvent and insoluble in the non-solvent. Controlling the size of the NPs passes through the optimization of process parameters as well as the formulation and physicochemical parameters, like the chemical nature of the solvent and non-solvent, the respective solubility of the material in both phases, their concentrations, the surfactant properties of the polymer and/or drug. In fact, the solvent transfer is one of the main parameters governing the nanoprecipitation⁹, likely related to the miscibility between solvent and non-solvent which controls the speed of the mass transfer. The usefulness of this simple technique is limited to water-miscible solvents, in which the diffusion rate is enough to produce spontaneous emulsification. Then, even though some water-miscible solvents provoke a certain instability when mixed in water, spontaneous emulsification is not observed if the coalescence rate of the formed droplets is sufficiently high.

On the other hand, the literature reviewed that it is possible to tune this transfer with microfluidic approaches, which eventually improve the control on the NPs characteristics¹⁰⁻¹².

Microfluidics, the science and technology of manipulating nanoliter volumes in microscale fluidic channels, has impacted a wide range of fields including biological analysis, chemical synthesis and processes, single cell analysis, and tissue engineering^{13,14}.

From 1998, a very intense research was initiated and has now drastically widened the application of microfluidic systems,¹⁵ but in the recent years, microfluidic systems were adapted to control the mixing rate between solvent and non-solvent phase, and clearly showed advantageous results in term of NPs size control, compared to classical batch processes^{16,17}. The earliest example has reported the fine control of the mixing of two phases at nanoliters level within few microseconds with a flow focusing silicon-based micromixer¹⁸. This method was later adapted for the nanoprecipitation of PLGA (polylactic-co-glycolic acid) derivative NPs, providing the pioneer report on the controlled nanoprecipitation in microfluidic setup¹⁹. These works initiate a great research effort to explore the potentials of such novel microfluidic platforms for the elaboration of polymer and pure drug NPs by nanoprecipitation²⁰.

1.1.2 Nanoprecipitation and advantages of microfluidic systems

Literature reviews¹⁶ report two theoretical explanation about the formation of polymeric NPs by nanoprecipitation³: a dispersion mechanism such as the spinodal decomposition, which is classified as a “mechanical mechanism”, and the well-known nucleation and growth mechanism. In the first case, the solvent solution is broken into small chunks of fluids which are dispersed into the non-solvent solution^{21,22}. In the nucleation and growth mechanism²³, nuclei are first produced when the polymer reaches a supersaturation state due to the

solvent diffusion into the non-solvent solution. Then, the nuclei grow by molecular deposition of polymer chains at their surface^{24,25}.

Lince et al. (2008)²⁵ indicated that the process of particle formation in the nanoprecipitation method consists of three phases: nucleation, growth and aggregation. The rate of each step determines the particle size and the driving force of these phenomena is supersaturation, which is defined as the ratio of polymer concentration over the solubility of the polymer in the solvent mixture. The split between the nucleation and the growth phases is the crucial factor for monodisperse particle formation. Ideally, operating conditions should allow a high nucleation rate strongly dependent on supersaturation and low growth rate. The second theory is based on Gibbs–Marangoni effect, that explained rapid nanoparticle formation as a process due to differences in surface tension, since a liquid with a high surface tension (aqueous phase) pulls more strongly on the surrounding liquid than one with a low surface tension (organic phase solvent). These differences between surface tensions cause interfacial turbulence and thermal inequalities in the system, leading to the continuous formation of eddies of solvent at the interface of both liquids. Consequently, violent spreading is observed due to mutual miscibility between the solvents, the solvent flows away from regions of low surface tension and the polymer tends to aggregate on the oil surface and forms nanocapsules. According to this explanation, nanocapsule formation

is due to polymer aggregation in stabilized emulsion droplets, while apparently the nucleation and growth steps are not involved²⁶.

However, polydispersity due to the aggregation effects, complete removal of the solvents, in particular for high polymer–solvent affinities, and a low loading of hydrophilic compounds are still a challenging task²⁶ for the nanoprecipitation technique. Indeed, the inherent variability and complexity of conventional batch processes often make it challenging to produce particles with well-defined physicochemical and functional attributes^{3,8}.

Recently, the literature has shown that it is possible to precisely tune this transfer with microfluidic tools, which eventually enhance the control on the NPs size.

Microfluidics²⁷ refers to a set of technologies that control the flow of minute amounts of liquids or gasses typically measured in nano and picoliters in a miniaturized system. Microfluidic devices are designed to manipulate fluids in microchannels with significantly reduced consumption of reagents and demonstrate intrinsically efficient heat and mass transfer due to high surface-area-to-volume ratios. In fact, micrometer scale of the flow channels in microfluidic systems increases the surface to volume ratio, and is, therefore, advantageous for many applications. For microfluidic system, the specific Reynolds number ($Re = 1 \rho v/\eta$) of liquid flows in such microchannels is very small, typically smaller than 100. In such low Reynolds number regimes, turbulent mixing does not occur, and hence diffusive species

mixing plays an important role but is an inherently slow process. Consequently, the aim of microfluidic mixing schemes is to enhance the mixing efficiency such that a thorough mixing performance can be achieved within shorter mixing channels, which can reduce the characteristic size of microfluidic devices. Furthermore, the development of efficient mixing schemes is essential for increasing the throughput of microfluidic systems. Indeed, increasing the contact area between the species to be mixed is one of the most efficient means of enhancing the diffusive mixing effect²⁸. Accordingly, previous studies presented mixing schemes by feeding the samples of interest through discrete via holes, cantilever plate-valves or multi-channels in the microfluidic device. An alternative approach is to increase the contact area between the mixing species by designing the microchannel configurations so that the species are folded multiple times as they flow along the mixing channel. Efficient mixing and rapid chemical reaction at the nanoliter to picoliter scales allow microfluidic devices to better control the synthesis parameters and thus the nanoparticle sizes and properties. The miniaturization of synthesis systems provides new opportunities for advanced chemical synthesis, and also enables a broad range of biological and medical applications¹⁷. Microfluidics has impacted a wide variety of fields including biological analysis, chemical synthesis, single cell analysis, and tissue engineering¹³.

The use of microfluidic devices for nanoparticle synthesis is advantageous in many aspects, including enhanced processing accuracy and efficiency; flexibility for multi-step platform design; rapid turnaround results for fine tuning properties of synthesized nanoparticles, cost savings from reduced consumption of source materials and reagents, and safer operation and environmental friendliness since the process consumes much reduced hazardous chemicals and reagents. Microfluidic devices can generate homogeneous emulsions particles in a controllable manner. Microfluidic systems have been used for various applications such as the production of single and double emulsions and nanoparticles with numerous advantages on size control, the economy of reagents, among others. A relevant question, however, is that these systems operate with flow rates on a scale of $\mu\text{L}/\text{min}$ and often take hours to produce a few milliliters of solution. Thus, on one hand the systems are accurate to produce homogeneous particles with low consumption of reactants in a continuous flow, on the other hand, they have low productivity. Droplet generation in a microfluidic system is a well-understood and studied phenomena, which is attracting increasing attention owing to a variety of potential applications in biology, medicine, chemistry and a wide range of industries. Microfluidic devices can produce monodisperse droplets through a number of different methods including jets, T-junctions, cross-flowing, co-flowing and flow focusing devices. However, both mechanisms

require an efficient mixing between the polymer and non solvent solutions. In the case of nucleation and growth process, which is the process likely to be encountered with microfluidic systems, the faster the mixing, the smaller are the NPs.

Compared with conventional nanoprecipitation batch methods, advantages of microfluidic system lay in their excellent ability to manipulate nanoliter flows. Microfluidic systems such as micromixers can drastically reduce the mixing path of solvent and non-solvent down to few tens of micrometers, resulting in a very fast mixing achieved by diffusion within few milliseconds down to microseconds¹⁸. Thus, due to this fast and efficient mixing, different physicochemical properties of NPs can be obtained by controlling the ratio of flow rates of the non-solvent to the solvent solution or by changing the configuration of the micromixer. It usually results in the production of smaller particles compared to conventional methods²⁹. In addition, microfluidic systems are usually operated in continuous flow which supports the potential of NPs production at large scale. Another advantage of continuous production is the possibility to maintain over time the same quality of the product, a much important feature for the pharmaceutical industry. Furthermore, the laminar flow ensures predictable and reproducible mixing conditions across fluidic interfaces³⁰.

1.1.3 Hydrodynamic Flow Focusing in Microfluidics

The hydrodynamic flow focusing (HFF) is another method to reduce the diffusion path and so it is an efficient strategy to enhance the mixing³¹, but has virtually no limitation. Microfluidic devices based on HFF widely used to prepare NPs by nanoprecipitation^{19,30}. In the HFF, a middle sample solution (injected from the middle inlet) flows within the sheath of outer fluids (injected from the side inlets), which constrain laterally the inner sample flow to achieve a smaller stream and thinner lamination width²⁸. The extent of the width decrease of the focused stream depends on the volumetric flow rate ratio between the sample flow and sheath flows. The greater the flow rate difference, the greater the degree of width reduction. Mixing time is inversely proportional to the square of the diffusion path length (in this case represented by the focused stream width), therefore, decreasing the stream width results in faster mixing²⁸. This effect results in a better control of the NPs characteristics like smaller size and narrow size distribution. Note that the flow focusing extent can be controlled by the ratio of the flow rates of the main inlet flow to the side flows.

The HFF mixing principle was first introduced by Knight et al. in 1998¹⁸ and then adapted in 2008¹⁹ for the production of amphiphilic PLGA-b-poly(ethylene glycol) (PEG) NPs, for which acetonitrile served as the polymer solvent. When PLGA was added to the final PLGA-PEG polymer, the microfluidic system showed a better control on the NPs size compared to the batch process. Indeed, for the HFF technology, the size increased from 24 nm to only 34 nm when the

PLGA weight content was increased from 0 to 20 wt %, whereas for the batch method, the NPs size increased from 30 to 105 nm. Interestingly, when Karnik et al.¹⁹ admixed the polymer solution with a model drug (docetaxel, Dtxl) to get drug loaded PLGA-PEG NPs, drug encapsulation efficiency was increased from 20 to 50 % wt compared with the batch method. They also found that the final NPs size increased when Dtxl was added to the polymer solution. Thus, authors investigated the water/acetonitrile ratio (so-called cloud point) at which polymer precipitated by gradually adding water to a solution of the polymer with or without Dtxl in acetonitrile. Polymer alone was observed to precipitate for a water/acetonitrile ratio of 25% v/v, the presence of Dtxl shifted this value up to 45% v/v. It indicates that Dtxl starts precipitating after the polymer. Hence, a rapid mixing may yield to slightly lower drug encapsulation efficiencies as some drug may be 'locked out' of the NPs that have already been formed before the drug starts to precipitate. Capretto et al.³⁰ proposed a Y-type HFF setup that was used to prepare β -carotene loaded Pluronic F127 copolymer NPs by nanoprecipitation using tetrahydrofuran (THF) solution and water as solvent and non-solvent, respectively. When only Pluronic F127 was used, a mean NPs diameter of 130 nm was obtained. When β -carotene was used alone, it was found that β -carotene precipitated immediately due to its higher hydrophobicity. As a result, aggregation of big particles completely blocked microchannel. When both β -carotene and copolymer composed the solvent solution, obtained NPs

showed a much smaller size, of around 70 nm. Thus, it is clearly demonstrated that the composition of polymer solution has a significant influence on final NPs size as well as the superiority of the microfluidic approach compared to its batch counterpart, in terms of potential to control the NPs size. Palocci et al.³² proposed a novel HFF microfluidic device by assembling commercial stainless steel microcapillary tubes with cross junctions. Dexamethasone was used to get drug-loaded PLGA NPs (35–350 nm). Encapsulation efficiency was found to reach values up to 93%, whereas by the batch method, encapsulation efficiency reached a ceiling value of only 60%. To increase the throughput production of HFF micromixers, Kang et al.³³ designed a three-layered poly(dimethyl siloxane) micromixer comprising 100 parallel flow focusing microchannels. The parallel flow focusing micromixer was then adopted to prepare NPs, similarly using PLGA-PEG amphiphilic polymer. The results indicated the device was quite robust in producing reproducible highly monodisperse NPs regardless the molecular weight of both copolymers and their weight content compared to the batch method. Lim et al.³⁴ reported the same structure to synthesise NPs. According to the results of Kang et al.³³, monodisperse NPs obtained from high molecular weight polymers were difficult to prepare by a batch method due to uncontrollable mixing process resulting in NPs aggregation. Thus, in order to use higher molecular weight polymers and to increase the polymer weight content in solvent solution as well

as to avoid unexpected clogging, a 3D flow focusing geometry was developed by Rhee et al.^{35,36} This 3D HFF micromixer was successfully used for the production of NPs from PLGA95K-PEG5K having a high molecular weight and introduced at weight content up to 5% w/v in acetonitrile. Sun et al.³⁷ proposed another 3D HFF micromixer based on the original concept of ‘origami chip’ and applied this new device to the production of doxorubicin-loaded PLGA NPs. The resulting NPs sizes obtained with the flat system (i.e. 2D device) were compared to those produced with the double spiral and arc systems. While the minimum size obtained with the former was 100 nm, in the same condition of flow rates, the last two systems produced much more monodisperse NPs sizes around 70 nm which was attributed to the significant reduction in mixing time (from 29 s down to 15 s) as simulated by computational fluid dynamics (CFD). Encapsulation efficiency of doxorubicin had reached 50 wt%. Souza Bicudo et al.³⁸ described a process for the production of Hyaluronic Acid (HA) crosslinked nanoparticles by nanoprecipitation at the interface of organic solvent/water phases. HA nanoparticles were crosslinked with adipic dihydrazide (ADH) and chloride carbodiimide (EDCL) and presented sizes ranging from 140 to 460 nm, depending on operational conditions.

1.1.4 Aim of the Chapter 1

In this chapter, we first have introduced theoretical considerations about the advantages of nanoprecipitation through mixing strategies

in microfluidics, which play a key role in the generation of high-quality nanoparticles, compared to batch production processes. Later, we have highlighted several representative microfluidic systems for controlled synthesis of nanoparticles with particular attention to Hydrodynamic Focusing approaches.

In this perspective, we present our work based on the design of a microfluidic platform to synthesize Hyaluronic Acid Nanoparticles (HANPs) under 50 nm. Herein, we demonstrate that rapid and tunable hydrodynamic flow focusing in microfluidics can be used to obtain HANPs with the defined size of about 50 nm and lower polydispersity. The proposed Microfluidic approach allows a continuous and controlled production of nanoparticles, overcoming the limits of common batch processes, and guaranteeing an instantaneous formulation and absence of purification step. Furthermore, our approach is also able to manipulate and modify the nanoparticle characteristics by fine-tuning the processing parameters such as flow rates or polymer concentration³⁹.

I.2 Case Study

I.2.1 Experimental Section

I.2.1.1 Materials

Sodium Hyaluronate ($M_w = 42$ kDa) was purchased from Bohus Biotech (Sweden). Acetone (CHROMASOLV, for HPLC, $\geq 99.8\%$; molecular formula CH_3COCH_3 ; $M_w = 58.08$), Ethanol (ACS reagent,

$\geq 99.5\%$ (200 proof), absolute; molecular formula $\text{CH}_3\text{CH}_2\text{OH}$; $M_w = 46.07$) were purchased by Sigma-Aldrich Co. The water, used for synthesis and characterization, was purified by distillation, deionization, and reverse osmosis (Milli-Q Plus).

1.2.1.2 Microfluidic set-up for flow focusing (FF) approach

A quartz microfluidic device “X- Junction Chip, $190\ \mu\text{m}$ ”, purchased from Dolomite Centre Ltd, was used to perform all the experiments. The device has a flow focusing geometry with a 90° angle between the inlets to enhance the diffusion process (Figure I-1a and b).

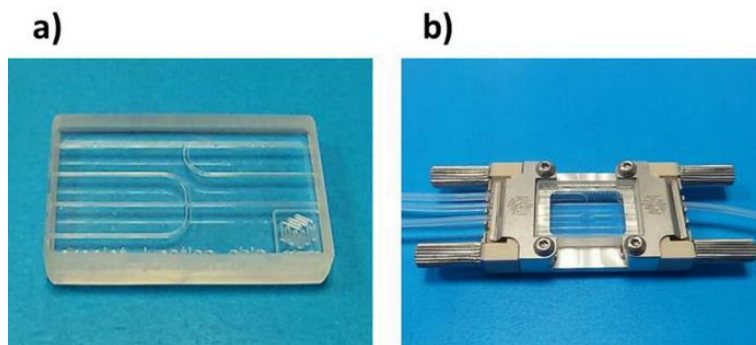


Figure I-1. Microfluidic Device. a) “Droplet Junction Chip $190\ \mu\text{m}$ ” with two configurations T- and X- junction, which can be used in combination. b) Droplet Junction Chip is compatible with Chip Interface H for fluidic connections.

The experimental set-up was summarized in (Figure I-2). The device was connected to 2.5-5 mL glass syringes (Microsyringes ILS Innovative Labor System) with FEP tubing ($1/16'' \times 0.25\ \text{mm}$) controlled by the syringe pumps (Low Pressure Syringe pumps, Nemesys system). Three-way isolation ETFE valves, connecting glass

syringe with the microfluidic device, make the automatic fill-in of the syringes feasible, thus allowing a continuous dispensing of reagents. The linkage between FEP tubes and microdevice is carried out through a specially designed connection with PTFE connectors. The flow focusing behaviour on the microchannel was observed using an Optical Fluorescence Microscope (Olympus IX71) with a 4 or 10 x scanning objective.

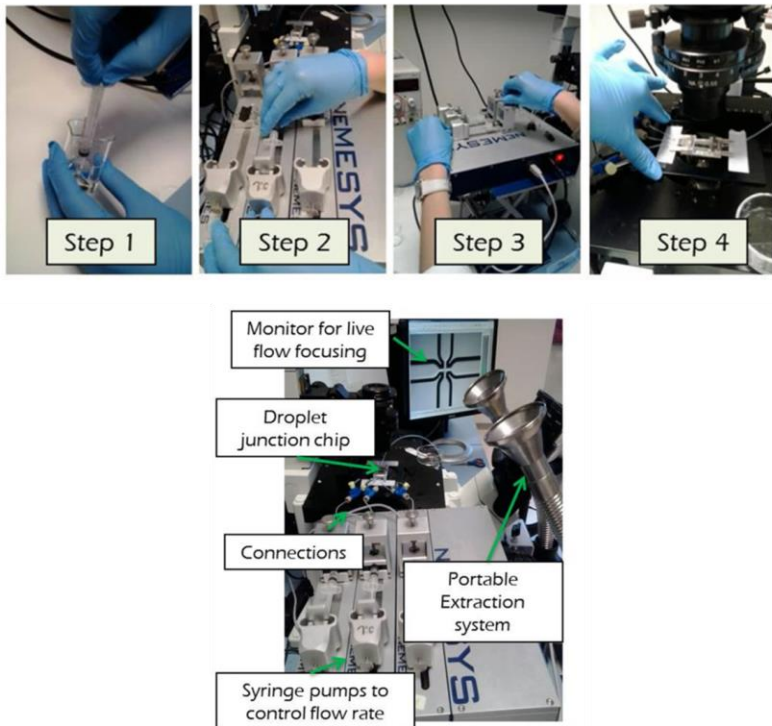


Figure I-2. Experimental set-up. The microdevice is connected to glass syringe controlled by Nemesys system. The flow focusing behaviour is observed using an Optical Fluorescence Microscope.

1.2.1.3 Production of Hyaluronic Acid Nanoparticles (HANPs) by nanoprecipitation in microfluidics

Different flow rates were tested, and the influence of the Flow Rate Ratio FR^2 , defined as the ratio of Volume Flow Rate Solvent and Volume Flow Rate Non-Solvent, was determined. For the feasibility study, a 5 mL aqueous solution containing HA concentrations ranging from 0.01 to 0.1% wt/v was used to explore the effects of the nanoprecipitation by flow focusing exclusively due to the concentration of the polymer. The initial solution was kept under continuous stirring for at least 4 hr and then injected through the middle channel. The flow rate of the middle channel was changed from 5 to 100 $\mu\text{L}/\text{min}$. Acetone or Ethanol, used as non-solvent and injected through the side channels, were laterally injected to induce nanoprecipitation by a non-solvent extraction. The flow rates of the side channels were ranged from 50 $\mu\text{L}/\text{min}$ to 300 $\mu\text{L}/\text{min}$, increasing each step of 10 $\mu\text{L}/\text{min}$. Precipitated nanoparticles were collected in a Petri glass containing about 25 mL of non-solvent and kept under continuous stirring. Each experiment was repeated at least 10 times.

1.2.1.4 HANPs purification and recovery

Purification was performed by a solvent gradient dialysis (Spectra Por Cellulose Membrane 6 – Mw cut-off MWCO 50.000) or by ultracentrifugation. A typical procedure consisted of loading collected samples into the dialysis tube and keeping the solution under continuous stirring at 130 rpm. Water was slowly added to the solution creating a concentration gradient and avoiding aggregation and

diffusion phenomena across the membrane. The recovery was performed at 15° C, at 80000 rpm for 45 min (ultracentrifugation).

1.2.1.5 HANPs size characterization

Following the purification of HANPs, Dynamic light scattering (DLS) was used to determine nanoparticle size and surface charge (Zeta sizer, Zeta Potential Malvern). DLS measures the light scattered from a laser that passes through a colloidal solution and by analyzing the modulation of the scattered light intensity as a function of time, the hydrodynamic size of particles and particle agglomerates can be determined. Larger particles will diffuse slower than smaller particles and the DLS instrument measures the time dependence of the scattered light to generate a correlation function that can be mathematically linked to a particle size. DLS is a valuable tool for determining and measuring the agglomeration state of nanoparticles as a function of time or suspending solution. The wavelength of the laser is 630 nm and the scattering angle used is 173°. The cuvettes used are the 12mm square glass cuvettes for 90° sizing (PCS8501). An ideal sample submission for DLS analysis has a volume of 1-2 mL.

In DLS analysis, the z-Average value represented the mean value of the hydrodynamic diameter of the particle, while the polydispersity index measured the width of the particle size distribution.

The formula for Polydispersity is:

$$Pdl = \left(\frac{\sigma}{d}\right)^2$$

where the polydispersity (PdI) = the square of the standard deviation/mean diameter. If the polydispersity index is > 0.1 , if the cumulants fit error is > 0.001 , or if the Result quality is Poor, then the data is more suspect and further analysis should be done to determine if valid data has been generated.

Nanoparticles Tracking Analysis measurements were performed with a NanoSight (NanoSight, Malvern), equipped with a sample chamber with a 640-nm laser and a Viton fluoroelastomer O-ring. The samples were injected in the sample chamber with a sterile syringe until the liquid reached the tip of the nozzle. All measurements were performed at room temperature. The samples were measured for 40s with manual shutter and gain adjustments. Three measurements of the same sample were performed for all samples.

1.2.1.6 Scanning Electron Microscopy

After these treatments, a hundred microliters of purified samples were deposited on a polycarbonate Isopore Membrane Filter (0.015, 0.05, 0.1 and 0.2 μm) by ultrafiltration vacuum system. The precipitated or deposited particles were coated with gold-palladium, and their morphology was observed by ULTRA PLUS Field Emission Scanning Electron Microscope (FE-SEM Carl Zeiss, Germany) with an accelerating voltage of 10-20 kV and using a lens detector. Samples for SEM applications need extremely thin, grain-free, uniform coatings to eliminate charging and to improve contrast on low density

materials. The device used was 208HR High Resolution Sputter Coated (Cressington).

1.2.2 Results and Discussion

1.2.2.1 Diffusive mixing time in Hydrodynamic Flow Focusing approach

The mixing time τ_{mix} is a key parameter for the formation of NPs through nanoprecipitation, which directly affects the size characteristics of the NPs produced⁴⁰. By adjusting the width of the focused stream (w_f) the mixing process can be controlled, providing a direct means for the control of particle characteristics, as demonstrated previously⁴¹. Indeed, it is the diffusion of the solvent and non solvent molecules in and out the focused stream that cause the diffusive mixing, and in turn the solvent jump, which drives the nanoprecipitation process⁴¹. Hydrodynamic focusing reduces the width of the focused stream (w_f) and consequently the distance over which the molecules diffuse, which represents the diffusion length for liquids to mix^{31,42}.

As reported by Capretto²⁸, according to the mass conservation principle, the volume of sample liquid that passes through the middle channel Q_2 must match the volume of the focused stream Q_f :

$$Q_2 = v_2 w_2 h = v_f w_f h = Q_f$$

$$w_f = \frac{Q_2}{v_f h}$$

w_f and w_2 represent the width of the focused stream and middle channel, respectively. Q_2 and Q_f are the volumetric flow rates of the middle channel and focused stream, respectively. h is the height of the channels, and v_2 and v_f are the average velocity of the flow in the middle channel and of the focused stream, respectively.

This equation provides a simple guideline for predicting the focused stream width. However, it does not reflect the effect of other factors such as device structure, channel surface, and fluidic property, which could affect the focusing process. In this respect, Lee et al.⁴³ proposed a similar model in which the effect of the density of the different fluids is taken into account, where w_f can be represented by:

$$w_f = \frac{Q_I}{Q_I + Q_E} \cdot \left(w_b + \frac{\pi}{2} h \right) \cdot a$$

where Q_I and Q_E are the flow rates of the middle stream and the total side streams respectively; w_b and h are the bottom width and height, respectively of the main channel; a is a factor dependent on channel geometries and the viscosity.

Consequently, the theoretical mixing time (τ_{mix}) was basically calculated as¹⁹:

$$\tau_{mix} \approx \frac{w_f^2}{4D} \approx \frac{\left(w_b + \frac{\pi}{2} h \right)^2 \cdot a^2}{4D \left(1 + \frac{1}{R} \right)^2}$$

Where D is the Diffusion coefficient of the solvent and R is the ratio of the flow rate of the focused stream to the total flow rate of the sheath flow.

In our microfluidic experiment, at standard process conditions, w_f is resulting in an average τ_{mix} of 46 ms therefore allowing the creation of homogeneous starting conditions for nanoprecipitation in which the role of mixing was not convoluted with the kinetics of aggregation.

1.2.2.2 Synthesis of Hyaluronic Acid Nanoparticles (HANPs) by Hydrodynamic Flow Focusing

Controlled nanoprecipitation of NPs relies on minimizing the mixing time to ensure a homogeneous environment during nucleation and growth of the NPs⁴⁴. This is realized by a fast solvent shifting, from organic to non-solvent, which provides a high level of supersaturation for all species, leading to nucleation and diffusion-limited aggregation of precipitates⁴⁵. An effective way to obtain controllable, fast and predictable mixing is the use of a microfluidic device architecture that allows the creation of a hydrodynamic focusing flow pattern.

In the flow-focused nanoprecipitation^{30,42,46}, the continuous phase, flowing through two side channels, meets the dispersed phase in the main channel, where the dispersed phase becomes compressed, and the solvents mutually diffuse promoting the precipitation of the solute and, therefore, the production of nanoparticle morphologies.

Figure I-3 shows a schematic of the microfluidic device used to synthesized Hyaluronic Acid (HA) NPs by nanoprecipitation of a hydrogel solution induced through a flow focusing approach.

HA dissolved into the aqueous solution flowing from the middle channel, mixed with non solvent flowing from the two side channels,

by achieving a stable hydrodynamic flow focusing along the main channel.

HA nanoparticles were formed at the interface between the organic phase and water in a laminar flow. As water diffuses into the non solvent phase, a supersaturated HA solution was formed at the interface between the phase, leading to HA nanoprecipitation.

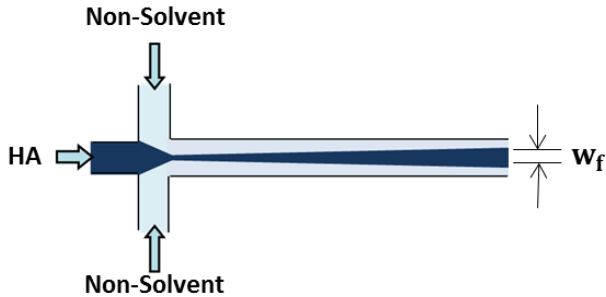


Figure I-3. Nanoprecipitation of HANPs. Schematic representation of the microfluidic device consisting of three inlets creating a hydrodynamic flow focusing with a middle stream of water and two side streams of non solvent. The width of the focused central stream (w_f) can be varied by altering the volumetric flow rates of the three inlets.

1.2.2.3 Influence of the non solvent on the HANPs characteristics

In order to better control the Nanoprecipitation process in our microfluidic device, the influence of the organic solvent (non solvent) has been studied. In fact, to improve the mixing process, all experiments were conducted using Acetone and Ethanol as non solvent.

Results show that the viscosity effects are crucial at the micrometer scale, and the different types of organic solvents also affected the flow field inside the microchannel.

Acetone presents the lower viscosity value (0.35 mPa s), thus its flow resistance is lower. The lower viscosity facilitates water transfer to the organic phase, leading to narrower streams. On the other hand, in the experiments with Ethanol the polydispersity is higher compared with Acetone. In fact, Ethanol extracts the water more slowly and thus it destabilizes the entire hydrodynamic focusing.

Finally, Acetone is preferred because it has a greater affinity with water and then a more rapid extraction, so Nucleation is favored to the Growth, obtaining smaller and monodisperse NPs. The affinity between water and the organic solvents can be analyzed by the Interaction (X) and Hansen Solubility $\Delta\delta$ parameters³⁸ as reported in Souza Bicudo et al.³⁸.

The affinity leads to a higher nanoprecipitation rate and consequently to smaller nanoparticles.

1.2.2.4 Influence of Flow Rate Ratio and polymer concentration and on HANPs characteristics

Flow rate conditions play a key role and Flow conditions of greater interest are selected analyzing the values of z- Average and of PDI obtained by Dynamic Light Scattering (DLS). We compared the effects of varying the flow rates on the mean diameter and the polydispersity of the HANPs.

Different flow rates are tested and results are presented in terms of the already defined Flow Rate Ratio FR^2 . Nanoparticle size varies from 35 nm to 500 nm, on the dependence of FR^2 ranging from 0.2 to 0.6 (as showed in Table I-1).

In DLS measurement, the z-Average value represents the mean value of the hydrodynamic diameter of the particle, while the polydispersity index measures the width of the particle size distribution related to the standard deviation σ .

Solvent Flow Rate [$\mu\text{L}/\text{min}$]	Non Solvent Flow Rate [$\mu\text{L}/\text{min}$]	Flow Rate Ratio S/NS	z-Average [nm]	PDI	SD (\pm) [nm]
40	100	0.4	218.2	0.138	40.58
	80	0.5	364.6	0.130	65.83
	60	0.67	480.8	0.087	70.99
	50	0.8	523.2	0.152	101.92
	30	1.3	1001.3	0.083	144.46
30	100	0.3	35	0.264	9
	80	0.37	86.5	0.199	19.30
	60	0.5	246	0.098	38.46
	50	0.6	341.8	0.157	67.74
	40	1	684.4	0.386	212.57
	30	1.5	890.1	0.721	377.78
20	100	0.2	40	0.242	9.83
	80	0.25	53	0.172	10.99
	60	0.3	58	0.169	11.92
	50	0.4	128.9	0.144	24.46
	30	0.6	197.7	3.706	190.3
	20	1	491.5	0.598	190

Table I-1. Dynamic Light Scattering Results at different FR^2 in terms of z-Average and Standard Deviation

Indeed, through the increase of the Non-Solvent Flow Rate and, therefore, the reduction of FR^2 , a more stable and narrow hydrodynamic focusing is achieved (Figure I-4a).

Our attention is focused on “easier to process” and high yield process parameters where the fast extraction of the solvent promotes nucleation to the detriment of growth leading to the production of almost monodisperse nanoparticles. Results are confirmed by low standard deviation values (Table I-1).

Moreover, the presence of precipitate in the mixing channel and the width of hydrodynamic focusing are considered. As already reported by Capretto et al., the mixing time strongly influences the formation of the nanoparticles by providing a high level of supersaturation for all species, when a stable hydrodynamic flow focusing is achieved along the main channel. In our system, a higher FR^2 increases the width of the middle stream, requiring a longer time to perform the mixing by diffusion and the non-solvent extraction by means of the nearby streams. This effect results in a larger amount of solvent in the final mixture possibly causing core swelling, hence the formation of large NPs (Figure I-4). Therefore, the selected optimal conditions provide fine focusing and absence of a precipitate in the mixing channel even for several hours (Figure I-4a).

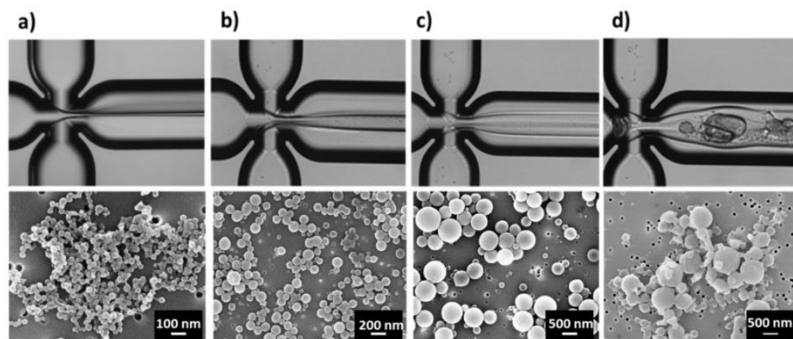


Figure I-4. Optical Fluorescence Microscope images of Flow focusing at several FR^2 : a) 0.3; b) 0.4; c) 0.8; d) 1.5 and FE-SEM images, respectively.

Furthermore, surface properties analysis of the HANPs is conducted to assess the promising delivery functions. HANPs have a negative surface charge of -50 mV ($\pm 4.5 \text{ mV}$) which can be attributed to the presence of carboxylic end group of the polymer on the nanoparticle surface, proposing their availability to future decorations of the nanoparticles.

We also examined the effect of polymer composition on nanoprecipitation by adding different amounts of HA.

The increased size of the NPs at higher initial polymer concentration could be explained as an effect of viscosity increasing and diffusivity decreasing. This observation can be explained by taking into consideration various phenomena associated with the supersaturation level and fluidic conditions.

A higher polymer concentration corresponds to a higher supersaturation level and faster nucleation and growth kinetics, therefore, stabilization occurs when growing NPs reach a larger size.

In addition, the more significant number of nuclei formed at higher concentrations could lead to particle aggregation before the stabilization takes place, thus forming larger NPs.

Furthermore, it has also been suggested that the increased viscosity of the organic phase at higher species concentrations might hinder the diffusion of solvent and non-solvent, requiring a longer mixing time and hence affecting the NP size and size distribution. Thus, Hyaluronic Acid concentration (C_{HA}) also affects the nanoprecipitation, and most of our experiments are conducted at a constant C_{HA} , 0.05% wt/v, allowing a longer stability of the system.

Quasi-monodisperse nanoparticles are obtained even for all FR^2 lower than 0.4 (Table 1). However, the value of FR^2 of 0.3 (obtained at 30 $\mu\text{L}/\text{min}$ -solvent flow rate – and at 100 $\mu\text{L}/\text{min}$ – non solvent flow rate) and C_{HA} of 0.05% wt/v is considered as an optimal condition (Figure I-5a and b). This choice is explained by the prolonged stability of the hydrodynamic flow focusing, the absence of massive precipitation and a higher yield in terms of nanoparticle collection and monodispersity. These preferred optimal values are selected as “standard conditions” and are used for the following evaluation steps. Field Emission Scanning Electron Microscopy (FE-SEM) images of the collected morphologies at size vs FR^2 and size vs C_{HA} are reported in Figure I-5c, d, and e.

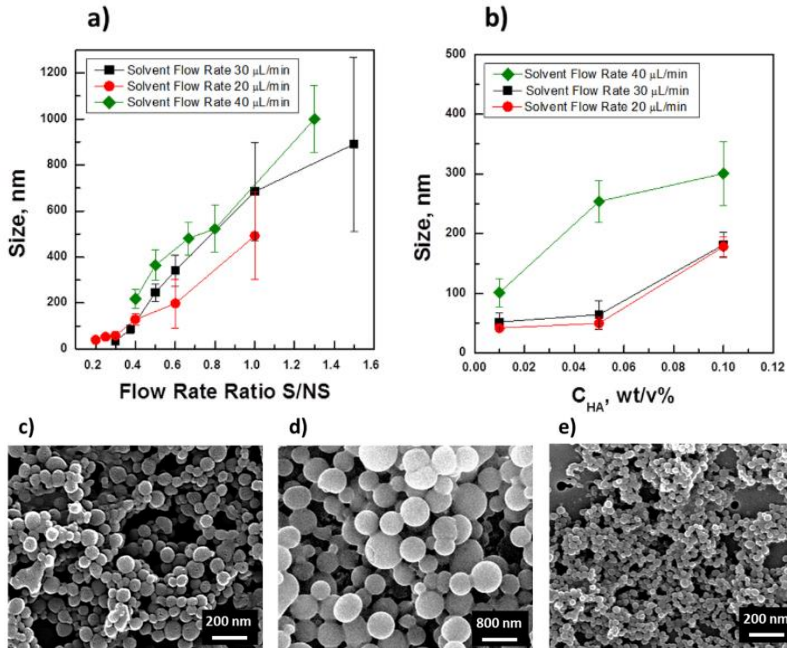


Figure I-5. Feasibility Study. a) Nanoparticles Size versus different Flow Rate Ratio FR^2 at constant Solvent Flow Rate: 30 $\mu\text{L}/\text{min}$ (- ■ -); 20 $\mu\text{L}/\text{min}$ (- ● -); 40 $\mu\text{L}/\text{min}$ (- ◆ -) for Hyaluronic Acid concentration C_{HA} of 0.05% wt/v. b) Nanoparticles Size versus C_{HA} (0.01% wt/v; 0.05% wt/v; 0.1% wt/v), at FR^2 of 0.3, obtained at Solvent Flow Rate 30 $\mu\text{L}/\text{min}$ (- ■ -); 20 $\mu\text{L}/\text{min}$ (- ● -); 40 $\mu\text{L}/\text{min}$ (- ◆ -). Field Emission Scanning Electron Microscopy (FE-SEM) images of Nanoparticles at FR^2 of c) 0.4; d) 1.5; e) 0.3.

To assess aggregation phenomena and stability, cHANPs have been tested by Nanoparticles Tracking Analysis (NTA) to evaluate if they are more suitable for onward development. NTA is a powerful characterization technique that complements DLS and is particularly valuable for analyzing polydisperse nanosized particles and their concentration. NTA measurements are performed with a NanoSight (NanoSight, Malvern), equipped with a sample chamber with a 640-

nm laser and a Viton fluoroelastomer O-ring. The samples are injected in the sample chamber with a sterile syringe until the liquid reached the tip of the nozzle. All measurements are performed at room temperature. The samples are measured for 40s with manual shutter and gain adjustments. Three measurements of the same sample are performed for all samples. The mean size and SD values obtained by the NTA software correspond to the arithmetic values calculated with the size of the nanoparticles analyzed by the software.

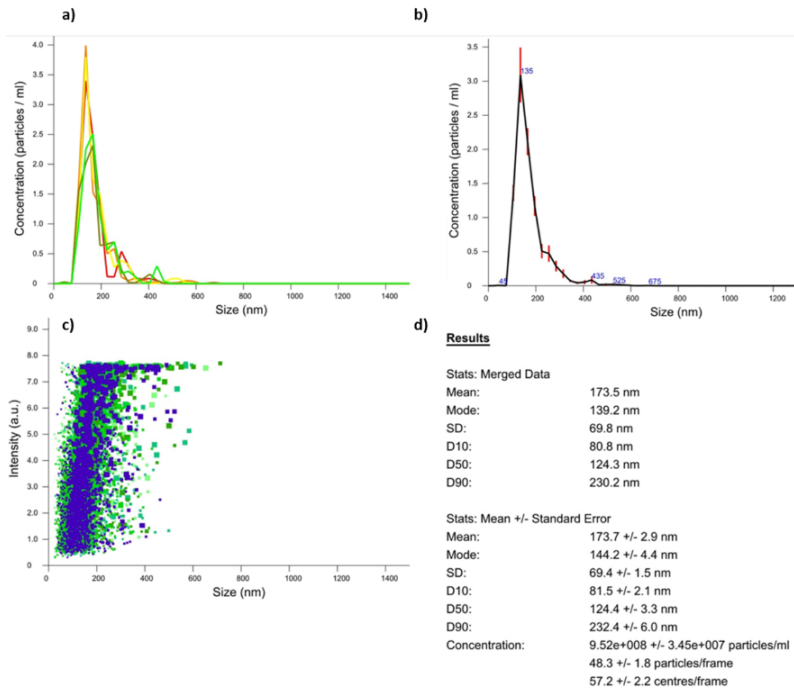


Figure I-6. Nanoparticles Tracking Analysis. Size distribution of cHANPs obtained through Nanoparticles Tracking Analysis. (a), (b) Concentration (particles/mL) versus size; (c) intensity (arbitrary unit) versus size; (d) summarized results.

1.2.2.5 Comparison between the traditional and microfluidic nanoprecipitation

Comparison between the traditional and microfluidic nanoprecipitation regarding nucleation and growth by diffusion is qualitatively reported in Figure I-7a and Figure I-7b . In the traditional nanoprecipitation, the mixing time drives the formation of nanoparticles of a certain size (Figure I-7a).

In the flow-focused nanoprecipitation, when a stable and thin hydrodynamic flow focusing is achieved along the main channel, the mixing time can be extremely reduced, and a fast extraction occurs at the nozzle section by providing a high level of mixing for all species (Figure I-7b).

In our microfluidic system, a high molecular weight polymer solution is added to the middle channel and focused by the non-solvent lateral flows. In these conditions, a rapid increase in the concentration of free polymer chains into the solution takes place, inducing a “burst nucleation” which makes other free polymer chains in solution unavailable. Indeed, during this “effective nucleation”, an increase in the rate of nucleation into the main channel produces a strong dilution of the polymer chains that limits the diffusion of the chains through the solution; consequently, reducing the growth by diffusion (Figure I-7b).

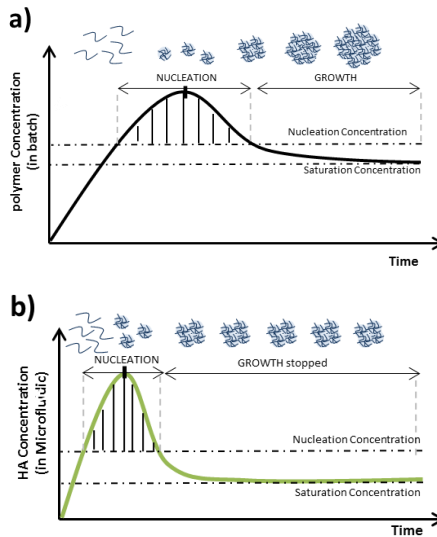


Figure I-7. Comparison between nanoprecipitation in bulk and in microfluidics. Interpretation of the nucleation and growth phenomena a) in a traditional batch system; b) in a microfluidic device. Panel a) shows the well-known thermodynamics related to the batch processes reported in the table for different polymers-solvent-non solvent systems. Panel b) represents the interpretation of the thermodynamics when nanoprecipitation occurs in a microfluidic device and a stable focused stream produces monodisperse nanoparticle by an *effective nucleation*.

1.2.2.6 Application of the proposed approach to additional materials

The exceptional strength of the proposed work, compared to the other investigations related to the formation of nanostructures, is also the ability to generalize our approach to other biomaterials. Our definition of the FR^2 and of the range of concentration enable to let unvaried the experimental process parameters even for other polymers such as polysaccharides, which are soluble in water or hydrophilic, selected from the group consisting of dextran, chitosan,

carboxymethylcellulose, glycosaminoglycans, including hyaluronic acid, derivatives and mixtures.

Results show that our microfluidic approach can be applied to various other polymers maintaining unchanged process parameters in terms of optimal FR² and range concentration to obtain easily several polysaccharide nanoparticles in a one step manner

I.3 Conclusions

The microfluidic synthesis is an emerging approach for the development of controllable nanoparticles for therapy and imaging. Because of the fast mixing and precise fluid control in microchannels, the monodisperse nanoparticles of complex structures can be continuously generated in a one-step manner.

Herein we demonstrate that microfluidics is a useful technology for nanoprecipitation synthesis of smaller and more homogeneous HANPs as compared to bulk synthesis. Microfluidics enables control over the rate of mixing, and in conjunction with controlling precursor composition, it may be used to tune nanoparticle size, homogeneity, and eventually drug loading and release.

Our work suggests that microfluidic synthesis of nanoparticles by controlled nanoprecipitation may enable better control over the physicochemical properties of nanoparticles and may prove to be useful in the emerging field of nanomedicine. A microfluidic-based approach has been used to produce a monodisperse collection of HA nanoparticles under 50 nm through a controlled Nanoprecipitation in a

microfluidic flow focusing approach. Our findings are interesting to investigate how the microfluidic environment determines the NPs size and stabilization, to facilitate further application of this rapidly growing technique. The influence of the process parameters, such as non solvent, HA concentration, Flow rate Ratio (FR^2) were examined on the controllability of NPs size and on the kinetics and mechanism of the nanoprecipitation process. It has been shown that when HA concentration increases the average particle diameter increased and the size distribution became wider. Typically, the microfluidics enables a fast mixing in the microchannels promoting the formation of nanomaterials at laminar flow condition. In our system, we have individuated a threshold value FR^2 of 0.3 below which it is possible to obtain more monodisperse and stable nanoparticles as low as 50 nm than the ones produced by similar bulk and microfluidic approaches. Furthermore, this threshold value is valid for high molecular weight polymers and at several polymer concentrations and different solvent/non-solvent couples. Our approach has the potential advantage of being able to generate a wider range of slot sizes of hydrogel structure while maintaining monodispersity compared to the similar bulk system. Furthermore, the flexibility of the process enable the tuning of the nanoparticles' size for a specific disease through changes of the hydrodynamic boundary conditions. The knowledge of this parameter will aid the proper selection of stabilizer type, concentration, and process parameters to obtain stable NP batches.

Moreover, the presented results extend the knowledge of the role that microfluidic reactors exert in controlling and tuning NP characteristics.

Nevertheless, optimization of a NP formulation depends on the specific properties and requirements of the systems, our results and the defined parameters and range of parameters represent a valid tool to approach the problem of nanoprecipitation in microfluidic.

Furthermore, these results with Hyaluronic Acid NPs could be potentially translated into a variety of similar polymer combinations, and be useful in the emerging fields of microfluidic formation of organic NPs and nanomedicine.

I.4 References

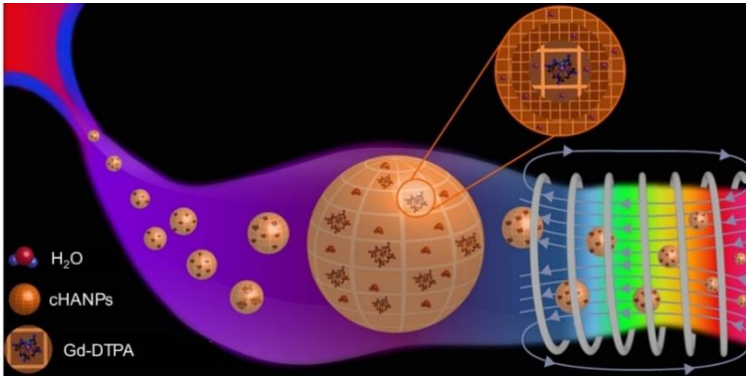
- 1 Choi, H. S. & Frangioni, J. V. Nanoparticles for Biomedical Imaging: Fundamentals of Clinical Translation. *Molecular Imaging* **9**, 291-310, doi:10.2310/7290.2010.00031 (2010).
- 2 Fessi, H., Puisieux, F., Devissaguet, J. P., Ammoury, N. & Benita, S. NANOCAPSULE FORMATION BY INTERFACIAL POLYMER DEPOSITION FOLLOWING SOLVENT DISPLACEMENT. *International Journal of Pharmaceutics* **55**, R1-R4, doi:10.1016/0378-5173(89)90281-0 (1989).
- 3 Mora-Huertas, C. E., Fessi, H. & Elaissari, A. Polymer-based nanocapsules for drug delivery. *International Journal of Pharmaceutics* **385**, 113-142, doi:10.1016/j.ijpharm.2009.10.018 (2010).
- 4 Kaur, V., Garg, T., Rath, G. & Goyal, A. K. Therapeutic potential of nanocarrier for overcoming to P-glycoprotein. *Journal of Drug Targeting* **22**, 859-870, doi:10.3109/1061186x.2014.947295 (2014).
- 5 Rao, J. P. & Geckeler, K. E. Polymer nanoparticles: Preparation techniques and size-control parameters. *Progress in Polymer Science* **36**, 887-913, doi:10.1016/j.progpolymsci.2011.01.001 (2011).
- 6 Quintanar-Guerrero, D., Allemann, E., Fessi, H. & Doelker, E. Preparation techniques and mechanisms of formation of biodegradable nanoparticles from preformed polymers. *Drug Development and Industrial Pharmacy* **24**, 1113-1128, doi:10.3109/03639049809108571 (1998).
- 7 PK, G. in *Indian J Biochem Biophys* (2000).
- 8 Schubert, S., Delaney, J. T., Jr. & Schubert, U. S. Nanoprecipitation and nanoformulation of polymers: from history to powerful possibilities beyond poly(lactic acid). *Soft Matter* **7**, 1581-1588, doi:10.1039/c0sm00862a (2011).
- 9 Chen, J. F., Zheng, C. & Chen, G. T. Interaction of macro- and micromixing on particle size distribution in reactive precipitation. *Chemical Engineering Science* **51**, 1957-1966, doi:10.1016/0009-2509(96)00053-x (1996).
- 10 Jahn, A., Vreeland, W. N., Gaitan, M. & Locascio, L. E. Controlled vesicle self-assembly in microfluidic channels with hydrodynamic focusing. *Journal of the American Chemical Society* **126**, 2674-2675, doi:10.1021/ja0318030 (2004).
- 11 Jahn, A. *et al.* Microfluidic Mixing and the Formation of Nanoscale Lipid Vesicles. *Acs Nano* **4**, 2077-2087, doi:10.1021/nn901676x (2010).
- 12 Jahn, A. *et al.* Preparation of nanoparticles by continuous-flow microfluidics. *Journal of Nanoparticle Research* **10**, 925-934, doi:10.1007/s11051-007-9340-5 (2008).
- 13 Mae, K. Advanced chemical processing using microspace. *Chemical Engineering Science* **62**, 4842-4851, doi:10.1016/j.ces.2007.01.012 (2007).

- 14 Valencia, P. M., Farokhzad, O. C., Karnik, R. & Langer, R. Microfluidic technologies for accelerating the clinical translation of nanoparticles. *Nature Nanotechnology* **7**, 623-629, doi:10.1038/nnano.2012.168 (2012).
- 15 DeMello, J. & DeMello, A. Microscale reactors: nanoscale products. *Lab on a Chip* **4**, 11N-15N, doi:10.1039/b403638g (2004).
- 16 Ding, S. K., Anton, N., Vandamme, T. F. & Serra, C. A. Microfluidic nanoprecipitation systems for preparing pure drug or polymeric drug loaded nanoparticles: an overview. *Expert Opinion on Drug Delivery* **13**, 1447-1460, doi:10.1080/17425247.2016.1193151 (2016).
- 17 Lee, L.-H. H. A. P. in *Journal of Medical and Biological Engineering* (2007).
- 18 Knight, J. B., Vishwanath, A., Brody, J. P. & Austin, R. H. Hydrodynamic focusing on a silicon chip: Mixing nanoliters in microseconds. *Physical Review Letters* **80**, 3863-3866, doi:10.1103/PhysRevLett.80.3863 (1998).
- 19 Karnik, R. *et al.* Microfluidic platform for controlled synthesis of polymeric nanoparticles. *Nano Letters* **8**, 2906-2912, doi:10.1021/nl801736q (2008).
- 20 Anton, N. *et al.* A new microfluidic setup for precise control of the polymer nanoprecipitation process and lipophilic drug encapsulation. *Soft Matter* **8**, 10628-10635, doi:10.1039/c2sm25357g (2012).
- 21 Galindo-Rodriguez, S., Allemann, E., Fessi, H. & Doelker, E. Physicochemical parameters associated with nanoparticle formation in the salting-out, emulsification-diffusion, and nanoprecipitation methods. *Pharmaceutical Research* **21**, 1428-1439, doi:10.1023/B:PHAM.0000036917.75634.be (2004).
- 22 Hessel, V., Lowe, H. & Schonfeld, F. Micromixers - a review on passive and active mixing principles. *Chemical Engineering Science* **60**, 2479-2501, doi:10.1016/j.ces.2004.11.033 (2005).
- 23 Thanh, N. T. K., Maclean, N. & Mahiddine, S. Mechanisms of Nucleation and Growth of Nanoparticles in Solution. *Chemical Reviews* **114**, 7610-7630, doi:10.1021/cr400544s (2014).
- 24 Aubry, J., Ganachaud, F., Addad, J. P. C. & Cabane, B. Nanoprecipitation of Polymethylmethacrylate by Solvent Shifting: 1. Boundaries. *Langmuir* **25**, 1970-1979, doi:10.1021/la803000e (2009).
- 25 Lince, F., Marchisio, D. L. & Barresi, A. A. Strategies to control the particle size distribution of poly-epsilon-caprolactone nanoparticles for pharmaceutical applications. *Journal of Colloid and Interface Science* **322**, 505-515, doi:10.1016/j.jcis.2008.03.033 (2008).
- 26 Quintanar-Guerrero, D., Allemann, E., Doelker, E. & Fessi, H. Preparation and characterization of nanocapsules from preformed polymers by a new process based on emulsification-diffusion technique. *Pharmaceutical Research* **15**, 1056-1062 (1998).
- 27 Badilescu, S. & Packirisamy, M. Microfluidics-Nano-Integration for Synthesis and Sensing. *Polymers* **4**, 1278-1310, doi:10.3390/polym4021278 (2012).

- 28 Capretto, L., Cheng, W., Hill, M. & Zhang, X. Micromixing Within Microfluidic Devices. *Microfluidics: Technologies and Applications* **304**, 27-68, doi:10.1007/128_2011_150 (2011).
- 29 Tsuji, H., Mizuno, A. & Ikada, Y. Properties and morphology of poly(L-lactide). III. Effects of initial crystallinity on long-term in vitro hydrolysis of high molecular weight poly(L-lactide) film in phosphate-buffered solution. *Journal of Applied Polymer Science* **77**, 1452-1464, doi:10.1002/1097-4628(20000815)77:7<1452::aid-app7>3.0.co;2-s (2000).
- 30 Capretto, L. *et al.* Mechanism of co-nanoprecipitation of organic actives and block copolymers in a microfluidic environment. *Nanotechnology* **23**, 16, doi:10.1088/0957-4484/23/37/375602 (2012).
- 31 Zhang, Z., Zhao, P., Xiao, G., Lin, M. & Cao, X. Focusing-enhanced mixing in microfluidic channels. *Biomicrofluidics* **2**, doi:10.1063/1.2894313 (2008).
- 32 Chronopoulou, L., Sparago, C. & Palocci, C. A modular microfluidic platform for the synthesis of biopolymeric nanoparticles entrapping organic actives. *Journal of Nanoparticle Research* **16**, doi:10.1007/s11051-014-2703-9 (2014).
- 33 Kang, X. *et al.* Mass production of highly monodisperse polymeric nanoparticles by parallel flow focusing system. *Microfluidics and Nanofluidics* **15**, 337-345, doi:10.1007/s10404-013-1152-6 (2013).
- 34 Lim, J. M. *et al.* Parallel microfluidic synthesis of size-tunable polymeric nanoparticles using 3D flow focusing towards in vivo study. *Nanomedicine-Nanotechnology Biology and Medicine* **10**, 401-409, doi:10.1016/j.nano.2013.08.003 (2014).
- 35 Rhee, M. *et al.* Synthesis of Size-Tunable Polymeric Nanoparticles Enabled by 3D Hydrodynamic Flow Focusing in Single-Layer Microchannels. *Advanced Materials* **23**, H79-H83, doi:10.1002/adma.201004333 (2011).
- 36 Valencia, P. M. *et al.* Single-Step Assembly of Homogenous Lipid - Polymeric and Lipid - Quantum Dot Nanoparticles Enabled by Microfluidic Rapid Mixing. *Acs Nano* **4**, 1671-1679, doi:10.1021/nn901433u (2010).
- 37 Sun, J. S. *et al.* A microfluidic origami chip for synthesis of functionalized polymeric nanoparticles. *Nanoscale* **5**, 5262-5265, doi:10.1039/c3nr01289a (2013).
- 38 Souza Bicudo, R. C. & Andrade Santana, M. H. Production of hyaluronic acid (HA) nanoparticles by a continuous process inside microchannels: Effects of non-solvents, organic phase flow rate, and HA concentration. *Chemical Engineering Science* **84**, 134-141, doi:10.1016/j.ces.2012.08.010 (2012).
- 39 Russo, M., Bevilacqua, P., Netti, P. A. & Torino, E. A Microfluidic Platform to design crosslinked Hyaluronic Acid Nanoparticles (cHANPs) for enhanced MRI. *Scientific Reports* **6**, 37906, doi:10.1038/srep37906 <http://www.nature.com/articles/srep37906#supplementary-information> (2016).

- 40 Kwon, G. S., Kuldipkumar, A., Tan, Y. T. F. & Andes, D. Polymeric micelles for the delivery of polyene antibiotics. *Abstracts of Papers of the American Chemical Society* **226**, U463-U463 (2003).
- 41 Lo, C. T., Jahn, A., Locascio, L. E. & Vreeland, W. N. Controlled Self-Assembly of Monodisperse Niosomes by Microfluidic Hydrodynamic Focusing. *Langmuir* **26**, 8559-8566, doi:10.1021/la904616s (2010).
- 42 Capretto, L., Carugo, D., Mazzitelli, S., Nastruzzi, C. & Zhang, X. Microfluidic and lab-on-a-chip preparation routes for organic nanoparticles and vesicular systems for nanomedicine applications. *Advanced Drug Delivery Reviews* **65**, 1496-1532, doi:10.1016/j.addr.2013.08.002 (2013).
- 43 Hung, C. I. *et al.* Hydrodynamic focusing for a micromachined flow cytometer. *Journal of Fluids Engineering-Transactions of the Asme* **123**, 672-679 (2001).
- 44 Capretto, L., Carugo, D., Cheng, W., Hill, M. & Zhang, X. L. Continuous-flow production of polymeric micelles in microreactors: Experimental and computational analysis. *Journal of Colloid and Interface Science* **357**, 243-251, doi:10.1016/j.jcis.2011.01.085 (2011).
- 45 Brick, M. C., Palmer, H. J. & Whitesides, T. H. Formation of colloidal dispersions of organic materials in aqueous media by solvent shifting. *Langmuir* **19**, 6367-6380, doi:10.1021/la034173o (2003).
- 46 Hood, R. R. & DeVoe, D. L. High-Throughput Continuous Flow Production of Nanoscale Liposomes by Microfluidic Vertical Flow Focusing. *Small* **11**, 5790-5799, doi:10.1002/smll.201501345 (2015).

II. CHAPTER II - A Microfluidic Platform to control the interference of Gd-DTPA in the design of crosslinked Hyaluronic Acid Nanoparticles (cHANPs) for MRI application



Graphical Abstract II-1. A Microfluidic flow focusing approach to design Gd-loaded cHANPs to be used in MRI field.

Abstract

A microfluidic flow focusing approach is proposed to synthesize crosslinked Hyaluronic Acid NanoParticles (cHANPs) down to 50 nm to be used in Magnetic Resonance Imaging (MRI). By fine tuning of the process parameters, microfluidic strategies based on hydrophilic-lipophilic balance (HLB) of the surfactants and pH conditions are reported to overcome interference in the precipitation derived from the presence of Gd-DTPA. Results are discussed regarding the role of the contrast agents on the nucleation and growth phenomena, and the competition between nanoprecipitation behavior and crosslinking reaction to optimize the entrapment of Gd-DTPA within cHANPs.

II.1 Background

II.1.1 Introduction

Microfluidic techniques allow preparing micro and nanoparticles having a specific narrow size distribution and further enable to perform high encapsulation efficiency and strong crosslinking reaction with ease^{1,2}. In effect, among the several advantages that microdimension of microfluidic tools provides there are also the ability to use rapidly products libraries of different materials by changing composition and flow rates; and the production of particles having coefficient of variation is less than 5% and high encapsulation efficiency; furthermore, parallelization on microfluidic chips allows high throughput and multiple analysis and reaction at a time. In this perspective, Karnik et al.³ synthesized biodegradable PLGA–PEG polymeric nanoparticles through a hydrodynamic flow focusing by nanoprecipitation where particle size and drug loading can be varied by flow rates, polymer composition and concentration. A nano-suspension of hydrocortisone was prepared using a microfluidic nanoprecipitation approach⁴. An axisymmetric flow focusing microchip was utilized to synthesize crosslinked alginate microparticles and nanoparticles using aqueous alginate droplets as templates, followed by the shrinkage of the drops due to the water diffusion to the continuous phase⁵. These authors go forward 2 years later^{6,7} with a similar flow focusing microfluidic device controlling the nanoprecipitation, showing that the co-encapsulation of hydrophilic

and hydrophobic anticancer drugs with high encapsulation efficiency, platinum prodrug, and docetaxel, respectively. They also indicate that modifying the surface of the resulting nanoparticles, by grafting A10 aptamer on the carboxylic function, gives rise to a specific targeting of prostate cancer cells up to the modification of the nuclear DNA by cisplatin. Very recent studies on such technology reported potential *in vivo* applications with hybrid/ PLGA nanoparticles designed as therapeutic and imaging agents⁸. Nanoparticle core encapsulated cytotoxic agent (doxorubicin) and lipid shell containing the anti-angiogenic drug. Contrasting properties were obtained using gold nanocrystals entrapped in the core as well as a dye (Cy7) grafted onto the surface. The authors showed the sustained release of the two drugs, with a longer time for the doxorubicin (encapsulated in the core), as well as *in vivo* the passive accumulation of the nanoparticles in the tumor. Detection was achieved through fluorescent modality, although the gold concentration was too low to allow a signal detection in CT. In another detailed microfluidic study, Capretto et al.⁹ presented the formation of block copolymer stabilized NPs (hybrid NPs), by examining the effects of operational fluidic conditions and the feed concentration of polymers and actives on the size characteristics and the polymer coverage of the organic actives. Pluronic F127 was used as a model block copolymer while highly hydrophobic β -carotene was used as a model drug. Results demonstrated the existence of competitive reactions leading to the formation of two types of

nanoparticles, i.e., either with or without loading β -carotene in the core-shell structure. Other microfluidic-based nanoprecipitation processes are reported using another biocompatible and biodegradable polymer that is chitosan, but this time playing on the aqueous solubility of the polymer as a function of the pH. Chitosan presents a pKa around 6.2 at room temperature, and thus, once solubilized at low pH, the mixing with a basic solution through microfluidic channels may induce the polymer nanoprecipitation. This idea was reported in recent articles^{10,11}, using hydrophobically modified chitosan, that is, by grafting palmitic acid on primary amines of chitosan with activation of acid by N-hydroxysuccinimide esters. The produced nanoparticles were ranging in size between 50 and 300 nm, and served to precisely encapsulate and release active hydrophobic principle (paclitaxel) over 1 week.

Nanoprecipitation processes in such devices open new advantages and new benefits regarding size control and also drug encapsulation control and improvement.

Starting from the observation of the Chapter 1, through microfluidics, we aim to achieve a fine-tuning of the mixing process among all species, and consequently, a tight control of their nanoprecipitation behaviour, of the crosslinking reaction, and of the encapsulation efficiency of a Magnetic Resonance Imaging (MRI) Contrast Agents (CAs), Gd-DTPA.

To date, Gd-based CAs are the most used in the clinical MRI with over 10 million contrast enhanced MRI scans every year, because of their relatively high stability and inertness in the body even if they still lack in tissue specificity and exhibit low relaxivity¹². Several strategies have been investigated to develop better contrast agents using nanotechnology. However, the exploitation of the microfluidic approaches to support the design of nanostructures entrapping clinically approved CAs for MRI is still missing.

Regarding the crosslinking strategy to adopt for Hyaluronic Acid Nanoparticles, several mechanisms have been reported in the literature¹³. The effectiveness of four different reagents, glutaraldehyde (GTA), 1-ethyl-3-(3-dimethylaminopropyl) carbodiimide (EDC), poly(ethylene glycol) diglycidyl ether (EX 810), and divinyl sulfone (DVS) as crosslinkers for cast hyaluronic acid (HA) films has been studied by Collins et al.¹³. The functional groups, which are mainly responsible for crosslinking of HA molecules are the hydroxyl and carboxyl groups. Hydroxyl groups may be crosslinked via an ether linkage and carboxyl groups via an ester linkage. If desired, the HA may be chemically modified prior to crosslinking to form other chemically reactive groups. Thus, for example, HA may be treated with acid or base such that it will undergo at least partial deacetalization, resulting in the presence of free amino groups. GTA-crosslinked films were found to be of low stability compared with those treated with EDC, EX 810, and DVS, due to in part residual acid

catalyst and also to molecular weight. Swelling studies showed that both the molecular weight of the films and the crosslinker type influenced the crosslink density of the films. DVS was found to be fastest reacting crosslinker¹⁴⁻¹⁶. The degree of swelling of DVS crosslinked gels can be controlled through swelling medium salt content and pH and this may be of value for drug release purposes. The EDC crosslinker system made gels of medium stability and to some degree stability is determined by the HA molecular weight¹⁴. However, the only one literature study that uses microfluidic approach to crosslink hyaluronic acid (HA) nanoparticles is represented by Souza Bicudo et al.¹⁷. They described a process to produce HA crosslinked nanoparticles by nanoprecipitation at the interface of organic solvent/water phases. HA nanoparticles were crosslinked with adipic dihydrazide (ADH) and chloride carbodiimide (EDCL) and presented sizes ranging from 140 to 460 nm, depending on operational conditions. Taking into consideration the observation about the stability and the high-speed reaction, we have selected DVS as the crosslinking agent for HA. Furthermore, even if DVS is highly reactive and toxic, the biocompatibility of the HA-DVS hydrogel has extensively been confirmed by histological analysis¹⁸.

II.1.2 Aim of Chapter 2

In this Chapter 2, we match a flow focused nanoprecipitation to an efficient crosslinking reaction based on Divinyl Sulfone (DVS) to entrap the relevant clinical Gd-DTPA in crosslinked Hyaluronic Acid

Nanoparticles (cHANPs) able to potentially increase its relaxometric properties without the chemical modification of the chelate. By fine tuning all process parameters, specific microfluidic strategies are developed based on the hydrophilic-lipophilic balance (HLB) of the surfactants and pH conditions, to overcome the interference of Gd-DTPA in the polymer precipitation phenomena. Interferences of the contrast agent in the flow focusing approach are reported for the first time, and different strategies are proposed to improve the encapsulation efficiency from 10% to 89% of the metal compound, at specific conditions. The developed strategies, allowing a fine tuning of the formulations, can be easily applied to other materials involved in nanomedicine field. The proposed approach has the objective to introduce microfluidic strategies to modulate the nanoprecipitation playing on the hydrophilic-lipophilic properties of the surfactants or the pH solution conditions¹⁹.

II.2 Case Study

II.2.1 Experimental Section

II.2.1.1 Materials

Materials used for cHANPs preparation were the same presented in Chapter 1. Sodium Hyaluronate ($M_w = 42$ kDa) was purchased from Bohus Biotech (Sweden). Hyaluronate Thiol (HA-SH), MW 50 kDa, and mPEG-Vinylsulfone (PEG-VS), MW 2kDa, were purchased from Creative PEGWorks. Diethylenetriaminepentaacetic acid

gadolinium(III) dihydrogen salt hydrate Gd-DTPA ($M_w = 547.57$ g/mol); Span80; Tween21; Tween85, Divinyl Sulfone (or Vinyl Sulfone) contains <650 ppm hydroquinone as inhibitor; purity 97%; density 1.117 g/ml at 25°C (lit.); molecular formula $C_4H_6O_2S$; $M_w = 118.15$ mp), Sodium Hydroxide NaOH (ACS reagent, $\geq 97.0\%$, $M_w = 40.00$), Gadolinium Chloride Solution $GdCl_3$ ($M_w = 263.61$), Sodium Chloride NaCl (ACS reagent, $\geq 99.0\%$, $M_w = 58.44$), ATTO633 652 g/mol were purchased by Sigma-Aldrich Co. Polyethylene glycole (PEG) – Fluorescein isothiocyanate (FITC) ($M_w = 1$ kDa) is purchased from Nanocs; HRP-conjugated Streptavidin, EDC (1-Ethyl-3-(3 dimethylaminopropyl)-carbodiimide) and N-hydroxysuccinimide (NHS) were purchased from Sigma Aldrich Co. The water, used for synthesis and characterization, was purified by distillation, deionization, and reverse osmosis (Milli-Q Plus).

II.2.1.2 Study of Gd-DTPA interference on the nanoprecipitation

The influence of the Gadolinium on nanoprecipitation was also evaluated. The entrapping of $GdCl_3$ or Gd-DTPA was exploited at several weight ratios HA/Gd ranging from 1:0.05 to 1:10, adding the metal complex to the HA aqueous solution. Loading capability and encapsulation efficiency were calculated by Induced Coupled Plasma (ICP-MS) - NexION 350. Nanoparticles were suspended in a solution of deionized (DI) water at a concentration of 150.000 particles/mL. All data were collected and processed using the Syngistix Nano

Application Module. Gd was measured at m/z 157 using a 100 μ s dwell time with no settling time.

II.2.1.3 Preparation of crosslinked Hyaluronic Acid Nanoparticles (cHANPs)

As already presented in the Introduction, literature studies report that the chemical reaction between HA and DVS is performed at high pH values (0.2 M NaOH, 0.1 M NaCl, $\text{pH} > 13$)^{14,20,21}. In our microfluidic system, a study on the reagents was conducted to create, at the nozzle section, sulfonyl bis-ethyl linkages between the hydroxyl groups of the polymer chains forming nanoparticles. Several experiments are carried out to study the effect of NaCl and NaOH to promote the reaction and to reduce growth's step suddenly after the nucleation phase. The crosslinking agent was injected alternatively into the middle channel or in the side channels at different concentrations, ranging from 0 to 20% v/v and from 0 to 8% v/v, respectively. In some strategies, the device is heated at 35°C through a heat chamber. In our system, the occurrence of the solvent extraction produces the dilution of water into the mainstream, slightly increasing the reaction time. For these reasons, to promote the crosslinking reaction, purification and dialysis in water of the collected nanoparticles are performed after 4 hr that nanoparticles have been kept under continuous stirring.

II.2.1.4 Fourier transform Infrared spectroscopy (FT-IR)

Fourier transform infrared spectra (FT-IR)^{20,21} were collected from Nicolett 6700 FT-IR spectrometer (Thermo Scientific). All the IR

spectra of the specimen were collected at 0.09 cm^{-1} resolution with 2 min interval. The characteristic peaks for DVS, which exhibit absorptions at 1310 cm^{-1} (S=O asymmetric stretching vibrations), 1130 cm^{-1} (S=O symmetric stretching vibrations) and 794 cm^{-1} (S–C stretching vibrations) and through the ether bond at 1255 cm^{-1} (C–O–C stretching vibrations).

Furthermore, thiolated HA, mPEG-Vinylsulfone and PEGylated cHANPs were analyzed to confirm if the reaction has taken place. Spectra were recorded and analyzed for signal assignation.

II.2.1.5 Effect of the surfactant concentrations and pH conditions on the system parameters

All experimental conditions were tested by adding NaOH and NaCl to the HA solution at the concentrations ranging from 0.1 M to 0.3 M and 0.02 and 0.2 M, respectively.

Alternately, three surfactants were tested at different reagent concentrations for all experimented flow rates. Tween 85 (ranging from 0.5% v/v to 1% v/v), Tween 21 (ranging from 0.5% v/v to 3% v/v) and Span 80 (ranging from 0.5% v/v to 1.5% v/v) were mixed to the non-solvent or to the aqueous solution. Experiments were conducted without the addition of DVS.

II.2.1.6 Stability and swelling behaviour of the cHANPs

Because of the clinical relevance of Gd-DTPA and, on the contrary, the high cytotoxicity of the GdCl_3 , stability studies were optimized only on Gd-DTPA. The Gd-DTPA loaded cHANPs were mixed with

150 μL of Phosphate Buffered Saline (PBS). The nanoparticles were kept under shaking at 150 rpm at 37°C. The solution was divided into two equal parts and observed at 12, 24, 48, 96 and 172 hr post incubation. ICP-MS was used to assess a one-half of the solution for the total concentration of Gd^{3+} ions loaded within the nanoparticles. The other half of the solution was filtered using 0.45 μm filter, and the filtrate was analyzed for Gd^{3+} ions.

II.2.1.7 Loading capability and Encapsulation efficiency of Gd-DTPA in cHANPs

The lyophilization of cHANPs was performed using a freeze-dryer Christ, 1-4LSC. Briefly, a freezing step was conducted for 3 hr at 80 °C. A cooling profile of 1 °C/min was applied, sublimation at a shelf temperature of 6 °C and pressure of 0.85 mbar for at least 24 hr²². Finally, a secondary drying at 25 °C and 0.03 mbar was performed for 5-6 hr. Trehalose or sucrose ranging from 1-3% wt/v was added as cryoprotector if necessary. Dried particles were also observed by Field Emission-SEM. The quantification of drug loading and the encapsulation efficiency was determined by weighing a certain amount of particles, typically 1 mg, into each of three 1.5 mL ultracentrifuge tubes. Dry particles were collected at the bottom of the tube by performing a quick spin-down (80,000 rpm – 45 minutes – 15°C). Two methods were utilized to solubilize the compound contained in the particles: dissolving the particles in a solvent or swelling the particles to allow the release of the compound into

solution by shaking at 37°C for 1hr. The equations used to determine the loading capability **LC** and the encapsulation efficiency **EE** are²³:

$$\% \text{LC} = C_i V_i / m_{np_s}$$

$$\% \text{EE} = (C_i V_i / m_{np_s}) / (m_{Gd} / (m_{Gd} + m_{HA}))$$

II.2.1.8 Preparation and characterization of PEGylated cHANPs

Carbodiimide chemistry is used for conjugation of PEG to hyaluronic acid nanoparticles. Carboxyl groups on the surface of the NPs are activated by re-suspending the NPs in PBS and reacting with EDC and NHS. MES buffer is used because it has no amine or carboxyl groups that could compete in the reaction. NPs are then ultracentrifuged to remove excess EDC/NHS and the water-soluble isourea by product. Activated NPs are re-suspended in PBS buffer and reacted with NH₂-PEG-FITC. NPs are again centrifuged and washed with PBS buffer to remove unbound PEG. Qualitative characterization of PEGylated cHANPs is carried out by Stimulated Emission Depletion (STED), while the PEG chains, attached to the HA backbone, is qualitatively estimated by the bicinchoninic acid (BCA) assay²⁴, which results to be extremely precise and sensitive being able to detect the amount of protein of 0.5 µg/mL. The bicinchoninic acid under alkaline conditions is an extremely sensitive reagent, stable and specific for the Cu⁺, and form with it a compound of the intensity of purple colour that it is proportional to the amount of protein. The variation of the intensity is determined by absorbance measurements in a

spectrophotometer at 562 nm. As expected, 150 μL of the nanoparticle suspension were reacted with an equal amount of the working reagent solution and the mixture was incubated at 37 ° C for 2 hr. The results were compared with a BSA calibration curve and the concentration value was then extrapolated by a straight line of calibration obtained using bovine serum albumin samples of known concentration (0 - 40 $\mu\text{g}/\text{ml}$). All measurements were performed in triplicate.

II.2.1.9 Quantification of fluorophore concentration

The concentration of the fluorophore encapsulated within the cHANPs was measured by Spectrofluorimetry (EnSpire Multimode Plate Reader PerkinElmer). Different concentrations of the cHANPs suspension were investigated and compared with a calibration line. Each measurement was made in triplicate.

II.2.2 Results and Discussion

II.2.2.1 Successful conditions to produce cHANPs for MRI through a Microfluidic Flow-Focusing platform

As presented in Chapter 1, in the flow focused nanoprecipitation^{9,25,26}, the non solvent phase, flowing through two side channels, focuses the solvent phase in the main channel inducing the mutual diffusion of all solvents and promoting the precipitation of the solute and, therefore, the production of HANPs. The value of FR^2 of 0.3 (obtained at 30 $\mu\text{L}/\text{min}$ -solvent flow rate – and 100 $\mu\text{L}/\text{min}$ – non-solvent flow rates) and C_{HA} of 0.05% wt/v are considered as “standard process conditions” for all the experiments.

II.2.2.2 Interference of Gd-based Contrast Agents on the nanoprecipitation and strategies to control the flow focusing pattern

We next investigate the role of Gd-based contrast agents, GdCl₃ and Gd-DTPA, on the nanoprecipitation. The effect of the metal compounds is observed, and a comparison is made regarding the stability of the flow-focusing in the presence of these two CAs; furthermore, their influence on the morphology is also reported.

Figure II-1 reports a change in nanoparticle size obtained, at the standard conditions, by varying the concentration of CAs (C_{CAs}), Gd-DTPA and GdCl₃, alternately.

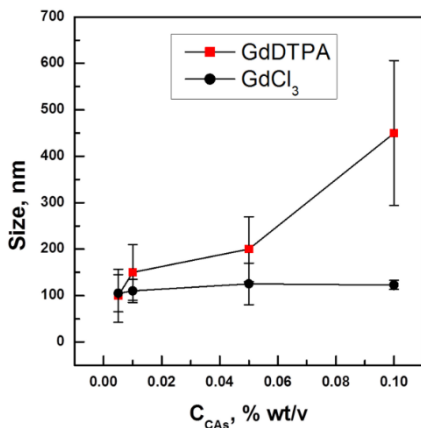


Figure II-1. Influence of Gadolinium based compounds. Nanoparticles size versus different C_{CAs}: (Gd-DTPA (- ■ -); GdCl₃ (- ● -)); at *standard conditions* showing how the stability of the hydrodynamic flow-focusing is compromised when Gd-DTPA is added to the solvent phase. No interference is observed in presence of GdCl₃ at different concentration.

A strong influence of Gd-DTPA on the focused stream and, therefore, on the precipitation is observed, which induces a significant increase in the nanoparticle's size and their uncontrolled shape. Further investigations are required to address this behaviour towards the control of the hydrogel nanoparticles. The stability of the hydrodynamic flow focusing results altered when Gd-DTPA is added to the solutions (Figure II-2 a and b) and, consequently, the morphology of the nanoparticles is compromised (Figure II-2 c and d).

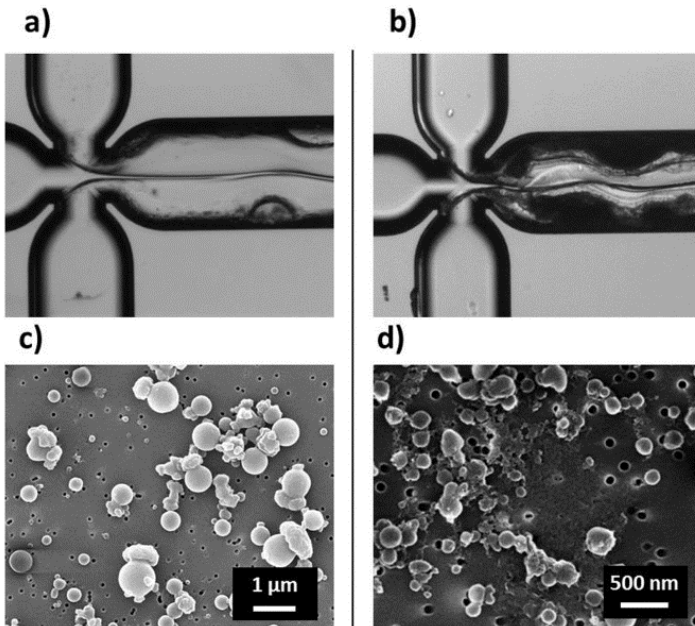


Figure II-2. Influence of Gd-DTPA on the nanoprecipitation. Instability of the Hydrodynamic Flow-Focusing when Gd-DTPA is added to the solvent phase. a) at the beginning and b) at the end of the experiment. FE-SEM images of larger and aggregated morphologies obtained at the concentration of Gd-DTPA of c) 0.1% wt/v, d) 0.05% wt/v.

Therefore, the formulation of rational strategies is needed to control the nanoprecipitation in the presence of Gd-DTPA. In details, the addition of the Gd-DTPA results in larger and high polydisperse nanoparticles. To control this interference and to restore optimized process parameters, we explore two different strategies: the tuning of pH conditions and the addition of hydro or lipophilic surfactants. In the first case, pH conditions are accurately tuned in the HA solution by varying NaOH concentration and keeping constant NaCl to avoid massive precipitation. Typically, a change in NaCl results in an increase of the crosslinking degree of the hydrogel nanoparticles. However, Figure II-3a shows how a further increase of NaCl concentration results in a massive and uncontrolled precipitation. The optimal value of NaCl concentration to obtain nanoparticle morphologies is 0.05 M; indeed, at higher concentrations, it is only possible to observe fiber-like morphologies mixed to nanoparticles (Figure II-3b).

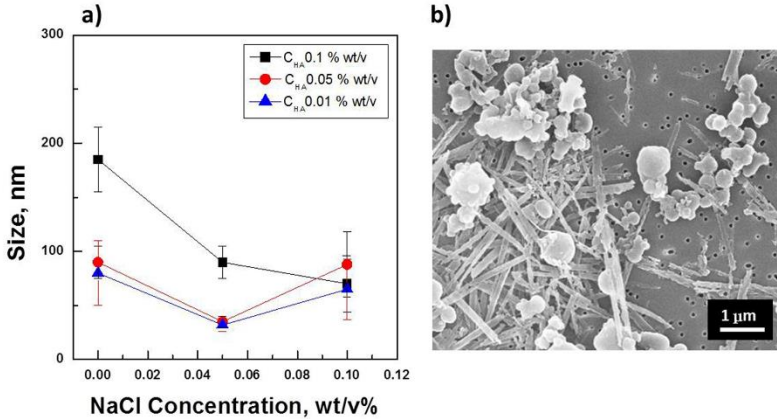


Figure II-3. Influence of NaCl on nanoparticles morphologies. a) Nanoparticles size versus NaCl concentration by varying C_{HA} (0.01 % wt/v (- \blacktriangle -); 0.05 % wt/v (- \bullet -); 0.1 % wt/v (- \blacksquare -); b) FE-SEM image of morphologies at 0.1M NaCl concentration showing fiber-like morphologies.

To restore the previous morphology, a narrow range of pH values, from 11.5 to 12.5, is found to be appropriate to control the interference between Gd-DTPA and HA matrix. Indeed, the variation of pH in the middle channel, when Gd-DTPA is also added, strongly influences the flow-focusing pattern by reducing the flow perturbations within the microfluidic device. Nanoparticles of around 40 nm in diameter are obtained for this range of pH. Furthermore, the significant success of this strategy can not only be found in the reduced size of the nanoparticles but also into the considerable increase of the Gd-DTPA concentration in the HA solution from 0.005 to 0.1% wt/v.

Figure II-4a clearly shows the effect of pH on the nanoparticle size due to the improved stability of the flow-focusing. This first strategy confirms that the addition of alkali changes the conformation of the

molecule through the breaking of hydrogen bonds, therefore influencing the interference with the Gd-DTPA, and the polymer molecules begin to untangle from each other, aligning in the direction of flow and resulting in a drastic reduction in viscosity. This optimal pH range reduces the viscosity of the medium and anomalous precipitations and promotes the degree of crosslinking of the NPs, as reported in the next paragraphs. The second proposed strategy is exploited by adding surfactants to the side channels to support the streams during the focusing action and to modulate the nanoprecipitation. The optimization of the flow-focusing pattern is found to be strongly dependent on the hydrophobicity and hydrophilicity of the surfactants. Indeed, the good hydrophilicity of the Tween 21 (HLB =13.3) highly interferes with the extraction of the water solvent by increasing instability of the focusing and, consequently, inducing agglomeration or polydispersity of the observed sample. Contrarily, when the less hydrophilic Tween85 (HLB=11) is added to the non-solvent, the flow-focusing appears very stable, compared to the previous one, because the lower compatibility of the Tween85 with the water solvent reduces the formation of heterogeneities at the interface. However, for both surfactants, a slight increase of the nanoparticle size is observed (Figure II-4b). Following the previous results, a more hydrophobic surfactant is tested. Span80 (HLB=4.3) is highly insoluble in water but presents good solvation in alcohol. Indeed, when Span80 is added to the non-solvent, the stability

of the focusing strongly increases in comparison to the other surfactants. This significant result shows that it is possible to reduce the interferences at the solvent-non-solvent interface using an appropriate surfactant that can simply modulate the affinity between solvent and non-solvents, regaining the control of the flow focusing pattern and, consequently, the morphology of the nanoparticles (Figure II-4c and d).

For completeness of results, a few tests are also performed by adding the water-soluble surfactants to the middle channel, but the formation of nanostructured morphologies is not observed.

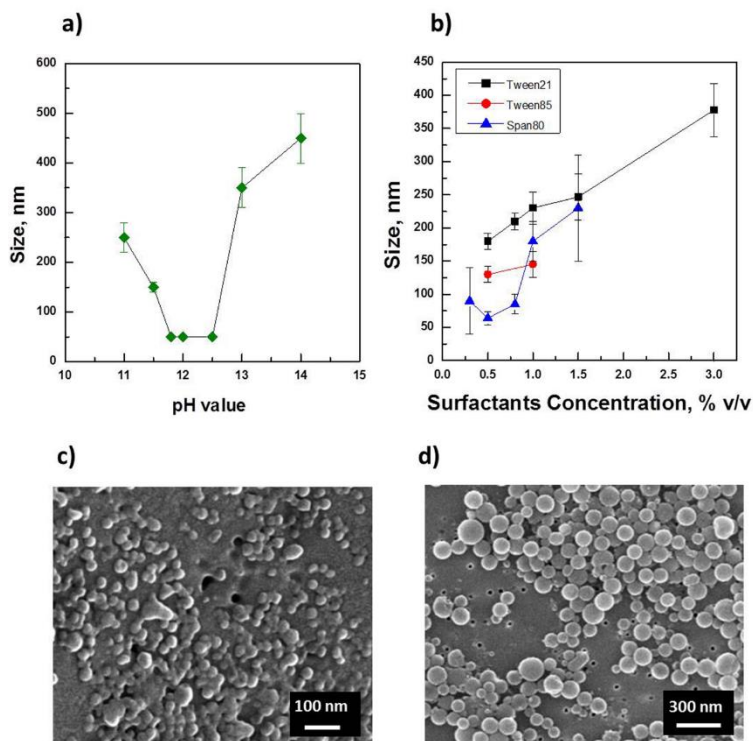


Figure II-4. Strategies to control the interference of Gd-DTPA on Flow-Focusing. Size of nanoparticles at C_{HA} 0.05% wt/v and at Gd-DTPA 0.1% wt/v reported for several a) pH values, b) concentration of surfactants; FE-SEM images of nanoparticles obtained at *standard conditions*: c) tilted image at 15° after the optimization of the pH value, d) not tilted image in presence of the hydrophilic surfactant Tween21 at 0.5% v/v. Data are collected without performing the crosslinking reaction and nanoparticles size is observed in Ethanol.

These strategies are also conducted at different pH values, confirming the preferred range of pH even in the presence of surfactants.

SURFACTANTS	pH	
0.5 % v/v < Tween21 < 3 % v/v 0.5 % v/v < Tween85 < 1.5 % v/v 0.5 % v/v < Span80 < 1.5 % v/v	11 < pH < 14	DVS side channels 0.4 % v/v < DVS < 5% v/v
0.5 % v/v < Span80 < 1.5 % v/v	11 < pH < 14	DVS middle channel 0.4 % v/v < DVS < 6% v/v Inlet channel $T \cong 5^{\circ}\text{C}$ Mixing channel $T \cong 35^{\circ}\text{C}$

Table II-1. Optimization of loading capability and crosslinking reaction. Process conditions of the investigated strategies to control the interference of Gd-DTPA in the nanoprecipitation mechanism: concentration of surfactants and tuning of pH condition together with the concentration of DVS added to the middle channel and to the side channel

II.2.2.3 Crosslinking and Swelling behaviour of cHANPs

Therefore, crosslinking strategies are needed to control the nanoprecipitation and stability of crosslinked HANPs (cHANPs) in the presence of Gd-DTPA. In this perspective, Divinyl Sulfone (DVS) has been selected among different highly reactive crosslinking agents for HA. Indeed, even if our DVS is highly reactive and toxic, the biocompatibility of the HA-DVS, i.e. sulfonyl bis-ethyl linkages between the hydroxyl groups of the polymer chains Figure II-5, has extensively been confirmed by histological analysis¹⁸, making our cHANPs appropriate for the potential clinical application.

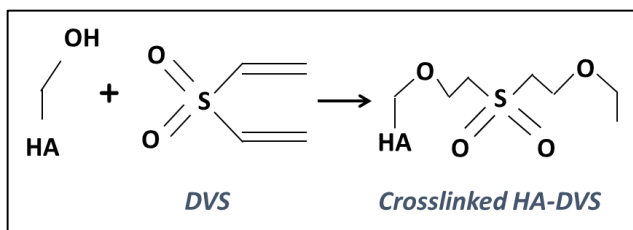


Figure II-5. Crosslinking reaction of HA hydroxyl groups with divinyl sulfone (DVS).

Furthermore, to confirm the success of the crosslinking reaction also IR analysis are performed. Figure II-6a and b show IR spectra of dried HA and of a dried solution composed by HA and DVS at pH 12. The chemical modifications of HA are identified in IR spectra of the cHANPs (Figure II-6c) by the characteristic peaks for DVS appearing between 1384 and 1280 cm^{-1} , which were attributed to the sulfone group ($\nu\text{SO}_2=1350, 1310\text{ cm}^{-1}$).

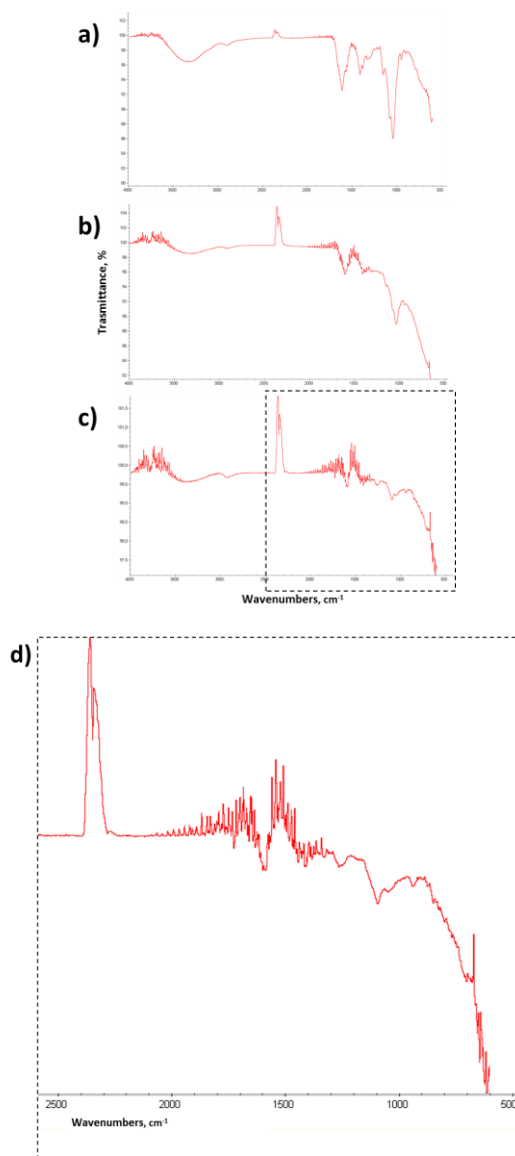


Figure II-6. IR spectrum, plotted as transmission, of a) dried HA powder b) dried solution composed by HA and DVS and c) and d) cHANPs

In the presence of Gd-DTPA, while nanoprecipitation occurs, two different crosslinking strategies are exploited to perform a simultaneous reaction: the injection of DVS into the middle channel or the side channels (Figure II-7a and b). These rational strategies are discussed in term of concentration and role played by pH and HLB of selected surfactants (i.e. Span 80, Tween 21 and 85), respectively used to avoid swelling and support the streams during the focusing action and modulating the nanoprecipitation.

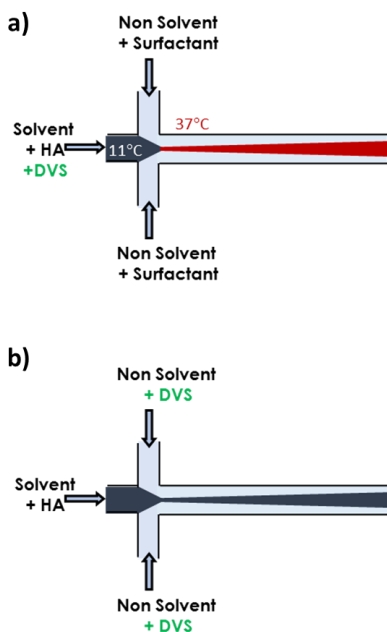


Figure II-7. Schematic illustration of the crosslinking strategies. Qualitative illustration within our microfluidic device of the two different crosslinking strategies: a) when DVS is added into the middle channel; b) when DVS is added into the side channels.

For the first strategy, a strict control of the temperature is necessary to avoid the onset of the crosslinking reaction in the HA aqueous solution before precipitation happens (Figure II-7a). During the injection, the polymer solution within the syringe is kept constant at 5°C while the microfluidic device is heated at 35°C, through a heat chamber, to promote the reaction at the nozzle section, where the mixing takes place. In this approach, nanoparticles of about 70 nm are produced at DVS concentrations of 0.6-0.8% v/v at standard conditions and C_{Span80} 0.5% v/v (Figure II-8a time point at zero seconds). Smaller nanoparticles are obtained of about 40 nm (Figure II-8b time point at zero seconds), at the standard conditions and pH equal to 12.3, by adding DVS to the side channels (Figure II-7b) even if an excess amount of agent, up to 4 % v/v, is necessary to avoid their swelling in water (Figure II-8b). Several experiments are also performed by adding DVS and surfactants to the side channels, but in this last case, both the morphologies and the crosslinking reaction result compromised. Both our chosen crosslinking approaches have the advantage to be highly tunable through process parameters and temperature. In our system, the occurrence of the solvent extraction produces the dilution of water into the mainstream, slightly increasing the reaction time. For these reasons, to promote the crosslinking reaction, purification and dialysis in water of the collected nanoparticles are performed after 4 hr of continuous stirring. However, the competition between crosslinking reaction and water

extraction affects mainly the second formulation, where an additional barrier to the reaction is represented by DVS diffusion from the side flow to the main one.

Additionally, the effect of the crosslinking degree is evaluated by the swelling behaviour under physiological conditions for both strategies: when DVS is injected through middle or side channels. In the first approach, a lower amount of crosslinker is used to reduce the swelling behaviour even after several hours. Indeed, stable nanoparticles are obtained for C_{DVS} ranging from 0.8 to 1.2% v/v. The increase of C_{DVS} at more than 1.2% v/v, however, promotes an instability of the flow or compromises the crosslinking reaction and, consequently, the swelling (Figure II-8a and c). Compared to the first approach, for the other one, a higher amount of agent is added to avoid a rapid swelling behaviour of nanoparticles in water. In particular, for C_{DVS} ranging from 4 to 4.5% v/v, the swelling behaviour of the cHANPs is not observed even after several days. Higher or lower concentrations of DVS lead to the formation of swelling particles or flow instability (Figure II-8b and d). Once again, the comparison between the two proposed strategies highlights considerable differences in the nanoparticle behaviour. Indeed, the smaller size and the absence of swelling behaviour obtained in the first strategy can be related to a faster and efficient crosslinking reaction due to more favourable reaction conditions in the aqueous environment, an ideal pH and temperature able to promote a faster crosslinking among the polymer chains. Additional data at

higher concentration of DVS, resulting in agglomeration and undefined morphologies or absence of nanoparticle formation, are not reported.

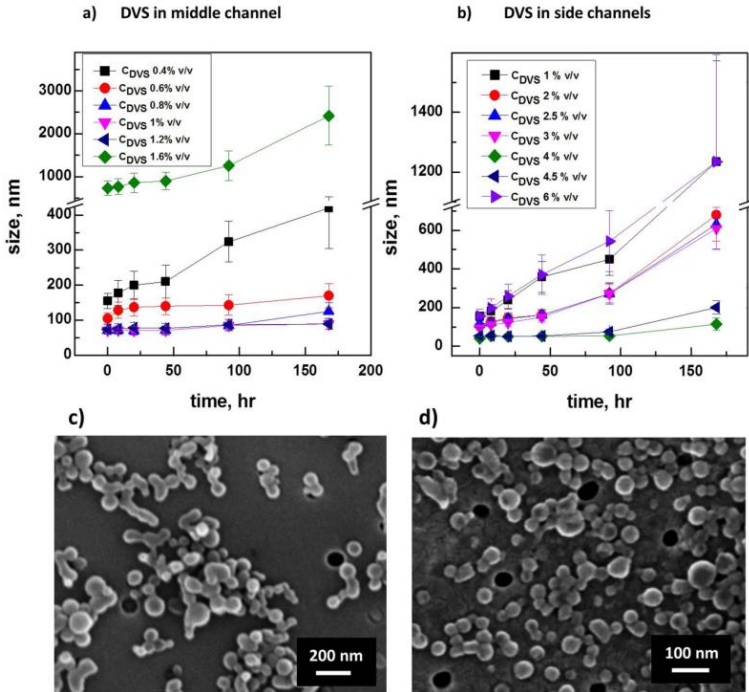


Figure II-8. Study of the Swelling behavior. Swelling behavior regarding nanoparticles size observed at several time points for different C_{DVS} when a) DVS is added in the middle channel, at standard process conditions, C_{Span80} of 0.5% v/v and 35°C; and b) DVS is added in the side channels, at pH equal to 12.3. FE-SEM images of cHANPs in water at the time zero when c) 0.8% v/v of DVS is added in the middle channel; d) 4% v/v of DVS is added in the side channels.

II.2.2.4 Loading Capability, Encapsulation Efficiency and Surface properties of Gd-loaded cHANPs

The proposed strategies also have the capability to increase or control the encapsulation efficiency (EE) in the cHANPs, to prevent the waste of expensive compounds and sustain their dosage over an extended treatment period. Results show that a DVS concentration added to the middle or the side phase has a significant impact on the entrapment efficiency of cHANPs. In details, for DVS in the middle channel, it is observed that an increase in DVS concentration (from 0.6 to 1% v/v) results in a rise of cHANPs encapsulation efficiency from 27 to 89% and a loading capability from 22 to 59%. On the contrary, a worse control is observed by increasing the concentration of DVS in the non-solvent phase, where a slight increase in cHANPs encapsulation efficiency and loading capability is obtained from 39 to 53% and from 26 to 35%, respectively, for selected DVS values of 4 and 4.5% v/v. Loading capability is only reported for stable nanoparticles in water and, it is also compared with loading capability resulting by the encapsulation of a highly toxic and non-chelate Gadolinium, $GdCl_3$ at equal conditions, proving that values reached are of about 90% (see the specific paragraph in the Experimental Section). The importance of a high encapsulation efficiency has been already emphasized since a large nanoparticles recovery is required for reducing manufacturing costs while size and morphology are important for quality control and biodistribution of injectable products. Furthermore, surface properties analysis of the empty cHANPs or cHANPs containing Gd-DTPA is

conducted to assess the promising delivery functions of the cHANPs. Gd-free cHANPs have a negative surface charge of $-50 \text{ mV} (\pm 4.5 \text{ mV})$ which can be attributed to the presence of carboxylic end groups of the polymer on the nanoparticle surface, proposing their availability to future decorations of the nanoparticles. Zeta Potential measurements show a significant increase to $-36.4 \text{ mV} (\pm 3.01)$ linked to the encapsulation of Gd-DTPA²⁷.

II.2.2.5 General observation about the interference of Gd-based CAs on Nucleation and Growth in Microfluidics

A comparison between the traditional²⁸ and microfluidic nanoprecipitation has been already presented in Chapter 1, now we have shown how this comparison has been carried out to take advantage from the Gd-DTPA interference and to design some rational strategies that could systematically ensure the entrapment of Gd-DTPA and the control of its loading. A qualitative evaluation regarding nucleation and growth by diffusion is reported in Figure II-9a. In the flow-focused nanoprecipitation, when a stable and thin hydrodynamic flow focusing is achieved along the main channel, the mixing time can be extremely reduced, and a fast extraction occurs at the nozzle section by providing a high level of mixing for all species Figure II-9a. However, the stability and the width of the hydrodynamic flow focusing are altered when even small concentrations of Gd-DTPA are added to the solutions (Figure II-9b), compromising morphology, size and loading capability of the nanoparticles. Indeed,

the Gadolinium complex acts probably as a salt compound, increasing the hydrogel strength significantly. A possible explanation can be that the electrostatic repulsion resulting from the charged groups on polymer chains is suppressed by the accumulation of counterions due to the metal complex²⁹. Furthermore, starting from the considerations reported by Gouin et al.³⁰ about the interaction between DTPA and HA, we hypothesize that Gd-chelate modifies the affinity of the polymer solution shifting the supersaturation to a low degree and leads to a slow heterogeneous nucleation followed by the growth of produced nuclei into large or aggregated particles. These specific interactions induce flow perturbation, causing an uncontrolled size variation and formation of aggregated morphologies (Figure II-9b). As showed, several rational strategies, based on pH of the solution and HLB of the surfactants, have been proposed to exploit the effects on the relaxivity of the presence of Gd-DTPA during the nanoprecipitation. A further outcome of the formulated strategies is the increase in the loading capability of Gadolinium based contrast agent that can be attributed to the repulsion between surfactant and water phase. Indeed, the retaining of the Gd-CAs is supported by the hydrophobic nature of the Span80 that increases the interface viscosity and prevents Gd-DTPA diffusion towards the external antisolvent phases. This behaviour is also explained by the higher molecular weight of the CAs, whose extraction, in these conditions, is less favoured compared to the small water molecules. This finding is of

crucial importance because the use of a surfactant is very easy to enforce compared to other alternatives, such as the utilization of a co-solvent, reduced concentration or addition of reacting components that could interfere with the reaction yield and contaminate samples. Later, the macrocyclic molecules have been firmly entrapped within the hydrogel matrix, using a crosslinking reaction simultaneously occurring with the nanoprecipitation. Investigations related to the addition of the DVS in the middle channels or into the side channels have furnished to the hydrogel nanoparticles some peculiar properties responsible for the modulation of the release behaviour and swelling properties.

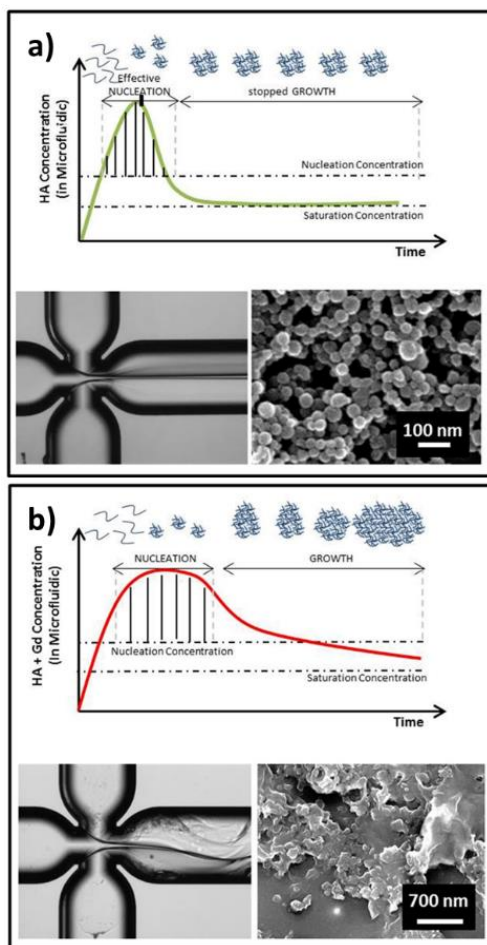


Figure II-9. Interference of the CA on the Nanoprecipitation mechanism. The schemes report the interpretation of the nucleation and growth phenomena in a microfluidic device. Panel a) represents the interpretation of the thermodynamics when nanoprecipitation occurs and a stable focused stream produces monodisperse nanoparticle by an *effective nucleation*. Panel b) represents changes of the nanoprecipitation phases, when Gd-DTPA is added to the solvent, and instability of the flow-focusing produces aggregated and polydisperse nanoparticles from a slow heterogeneous nucleation.

ICP-MS results demonstrated that using our flexible platform it is possible to take advantages from the strong interference detected by the presence of Gd-DTPA producing Gd-entrapped nanoparticles with enhanced loading.

The proposed approaches aim to overcome some drawbacks of the traditional procedures for the production of nanoparticles such as high polydispersity, expensive and time-consuming purification/recovery steps³¹. Furthermore, results present the effective strategy to dose all species and to control properly the entrapment of CAs within the hydrogel nanostructures that potentially influences MRI performances in terms of signal intensity and tissue specificity.

II.2.2.6 Simultaneous encapsulation of other agents

After the optimization of the Gd-DTPA entrapment within cHANPs, to confirm the versatility of our designed microfluidic platform, we have performed a successful simultaneous encapsulation of fluorophores, such as ATTO 633, ATTO 488, with Gd-DTPA for multimodal imaging.

The addition of a fluorophore to the middle channel, at “standard process conditions”, in quantities of at least 1 nmol /100 mL, does not influence the nanoprecipitation and crosslinking reaction, and, consequently, the flow focusing behaviour.

Field Emission Scanning Electron Microscopy (FE-SEM) characterization confirm the stability of the Nanoparticle' size, while as showed in Figure II-10. STED image of cHANPs with ATTO633

and Gd-DTPA entrapped. STED image proves the encapsulation of the fluorophore.

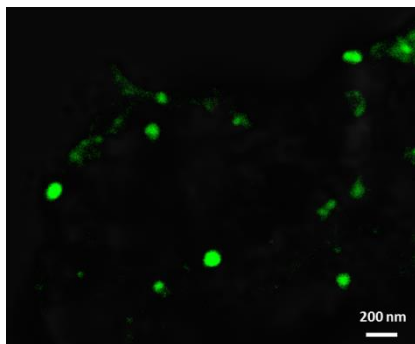


Figure II-10. STED image of cHANPs with ATTO633 and Gd-DTPA entrapped.

II.2.2.7 PEGylation of cHANPs

Owing to its high binding affinity for CD44, which is abundant in the tumor tissue, HA has been extensively investigated for the development of tumor-targeted imaging agents and drug delivery systems³². However, it is worthy of note that the targetability of HA is compromised by its binding to other receptors in normal organs, such as the LYVE-1 receptor on cells located in the lymphatics and the HARE receptor on liver sinusoidal endothelial cells³³. Therefore, it can be expected that modulation of the binding affinity of HA to the receptors may affect *in vivo* biodistribution and, eventually, targetability by a combination of active and passive targeting mechanisms. In this study, we aim to control delivery properties of cHANPs by PEGylation. Therefore, cHANPS of about 40 nm diameter are bioconjugated with PEG-FITC (1KDa). Previously zeta

potential results demonstrated that they are negatively charged surfaces (-40 mV), attributed to the presence of deprotonated carboxyl groups of HA. As expected, the zeta potential of the nanoparticles was slightly decreased by PEGylation (-15 mV), causing consumption of carboxylic acids at the backbone of HA. PEGylation is also useful to assess the surface stability of the nanoparticles during the chemical decoration and the ability to retain the loaded Gd compound. SEM, TEM and STED images of cHANPs after PEGylation reaction are reported in Figure II-11a, b, and c.

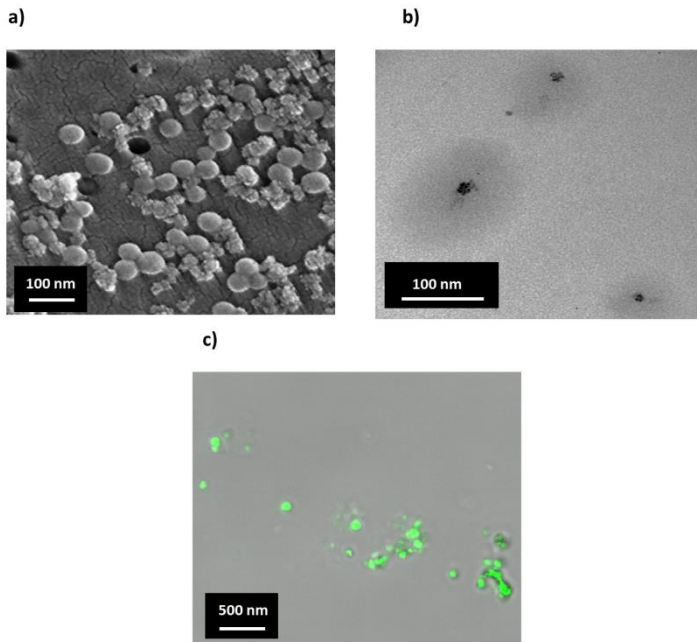


Figure II-11. PEGylation of cHANPs. FE-SEM a) TEM b) and STED images c) of cHANPs after conjugation reaction with PEG₁₀₀₀-FITC.

II.3 Another case study: preliminary results

II.3.1 Synthesis of PEGylated crosslinked nanoparticles by nanoprecipitation in microfluidics in a one-step manner

While in the above reported paragraph the PEGylation has been performed and optimized after the synthesis and the purification of Gd-loaded nanoparticles. In this session, we intend to demonstrate the versatility of our designed microfluidic platform by synthesizing PEGylated cHANPs (PEG-cHANPs) in microfluidics through a co-nanoprecipitation process of HA -SH and PEG-VS at the same condition just used to produce cHANPs but avoiding the batch pegylation reaction of our nanoparticles.

For the feasibility study, an aqueous solution containing thiolated HA (HA-SH) concentrations ranging from 0.01 to 0.1 % wt/v was tested. The initial solution was kept under continuous stirring for at least 4 hr and then mixed with PEG-vinylsulfone (PEG-VS) (ranging from 0.9 to 2.25 % v/v) at neutral pH and at 4°C to avoid the crosslinking reaction before nanoprecipitation occurs within the microfluidic device. Then, HA-SH and PEG-VS solution was injected through the middle channel. The flow rate of the middle channel was kept constant at 30 $\mu\text{L}/\text{min}$. Acetone, used as non-solvent and injected through the side channels, was laterally injected to induce nanoprecipitation by a flow focusing approach. The flow rates of the side channels were unchanged at 110 $\mu\text{L}/\text{min}$. Precipitated nanoparticles were collected in a Petri glass containing about 25 mL of non-solvent and kept under

continuous stirring. In the literature studies, hydrogels between HA-SH and PEG-VS were obtained through a Michael addition in PBS at 37 °C. The molar ratio of thiol groups to vinylsulfone groups was kept at 1.2^{34,35}. In our microfluidic platform, a study on the reagents was conducted to create, at the nozzle section, the nucleophilic addition of a carbanion (HA-SH) to unsaturated carbonyl compound (PEG-VS). Several experiments were carried out to promote the reaction and to reduce suddenly growth's step after the nucleation phase. Each successful experiment was repeated at least 10 times.

In this perspective, we have obtained HA-PEG hydrogels nanoparticles (of about 70 nm) using as aqueous solution 0.05 % wt/v thiolated HA (HA-SH) and 1.35 % v/v PEG-vinylsulfone (PEG-VS) to explore the effects of the nanoprecipitation on the flow focusing behaviour exclusively due to the presence of another polymer with not negligible molecular weight (PEG-VS = 2 KDa). Lower concentrations of PEG-VS lead to the formation of swelling particles while higher concentrations provoke uncontrolled precipitation of PEG-VS and flow instability.

In our microfluidic device, at the nozzle section, the nucleophilic addition of a carbanion (HA-SH) to unsaturated carbonyl compound (PEG-VS) is performed (Figure II-12a).

Transmission Electron Microscopy (TEM) and Field Emission Scanning Electron Microscopy (FE-SEM) images of the collected morphologies are showed in Figure II-12b and c, respectively. We can

observe that collected nanoparticles maintain their shape even after 48 hours in water due to a strong crosslinking reaction performed together with nanoprecipitation, encapsulation of Gd-DTPA and PEGylation of cHANPs. TEM image (Figure II-12b) shows a different electron density between the core and the shell, that can give a previous indication of the presence of an outer covering coating different from the cHANPs before the PEGylation. Results show that our microfluidic approach is able to maintain unchanged process parameters and further the concentration ratios between the various components in order to obtain monodisperse PEGylated crosslinked HA-PEG-VS nanoparticles in a one step manner.

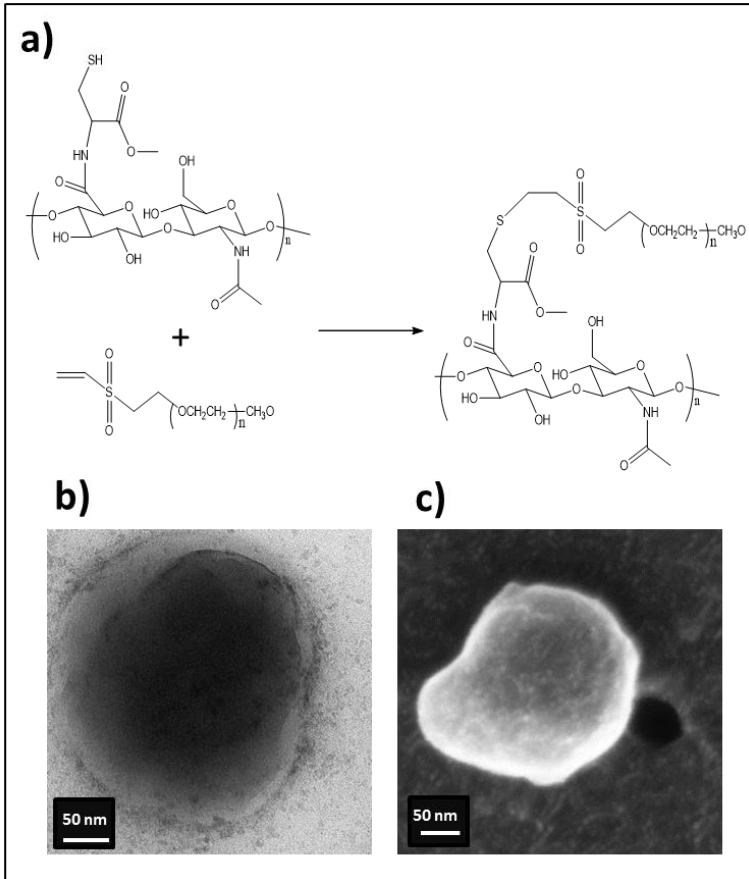


Figure II-12. Morphology of HA-PEG-VS Nanoparticles. a) Schematic illustration of the Michael Addition reaction mechanism of thiolated HA with PEG-VS. b) TEM and c) FE-SEM images of the PEGylated cHANPs in water after 48 hours.

II.3.2 Fourier Transform Infrared (FT-IR)

FT-IR analysis is performed to confirm the effectiveness of the reaction. Comparative FTIR spectra of HA-SH, PEG-VS and PEGylated cHANPs are showed in Figure II-13. The analysis shows that the PEGylated cHANPs do not exhibit the double bond C=C,

observed for PEG-VS at 750 cm^{-1} , due to the Michael Addition reaction between the double bond of the PEG-VS and thiol group of HA. Furthermore, the success of the reaction is also guaranteed by the presence of the peak at 600 cm^{-1} that indicates the C-S bond stretching. Nevertheless, results on PEGylated cHANPs also present the peak at 1245 cm^{-1} associated with C-SH vibration related to the residual not reacted thiols of the precursor HA-SH.

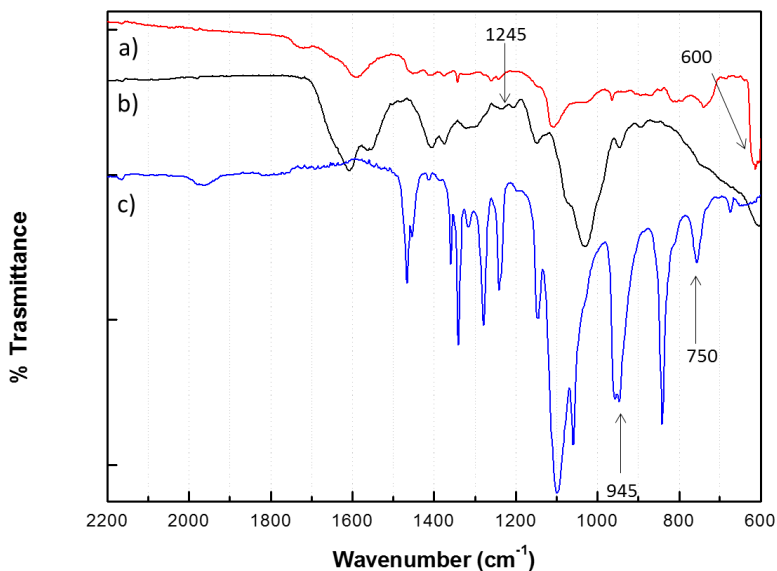


Figure II-13. FT-IR Analysis Comparison of FT-IR spectra of a) PEGylated cHANPs; b) HA-SH and c) PEG-VS precursors.

FT-IR analysis finally reports that microfluidic platform to produce PEGylated cHANPs can accurately control the tuning of the crosslinking reaction to improve relaxometric properties and stability of the system.

II.4 Conclusions

Crosslinked Hyaluronic Acid Nanoparticles (cHANPs) to be applied in MRI field have been developed and loaded with a clinically relevant Gd-CA, Gd-DTPA. For the first time, an interference of the Gd-DTPA in nanoprecipitation mechanism is reported which has added some significant advances in the basic knowledge of the interactions between Gd chelates and hydrogel matrix. We have demonstrated that, through our microfluidic strategies, it is possible to take advantages from the observed interference between HA and Gd-DTPA promoting a high entrapment of the Gd-DTPA within the cHANPs without chemically modifying the approved Gd-metal chelate. The designed strategies have allowed a fine control of the nanoparticle properties, such as the monodisperse average size of 40 nm, surface charge and the loading capability of 59%. A controlled degradation and release behaviour up to 96 hr under physiological conditions, high encapsulation efficiency of the hydrophilic metal chelate up to 89% are also reported. Furthermore, the surface charge analysis reports the presence of carboxylic groups that can be readily functionalized with targeting moieties, increasing potentially chemical functionalities to impact on tissue specificity and integrating additional imaging and therapeutic capabilities.

Our straightforward and scalable strategies are proposed as a microfluidic platform to develop hydrogel nanoparticles entrapping clinically approved agents for potential application in diagnostics and therapy.

II.5 References

- 1 Jahn, A. *et al.* Preparation of nanoparticles by continuous-flow microfluidics. *Journal of Nanoparticle Research* **10**, 925-934, doi:10.1007/s11051-007-9340-5 (2008).
- 2 Chronopoulou, L., Sparago, C. & Palocci, C. A modular microfluidic platform for the synthesis of biopolymeric nanoparticles entrapping organic actives. *Journal of Nanoparticle Research* **16**, doi:10.1007/s11051-014-2703-9 (2014).
- 3 Karnik, R. *et al.* Microfluidic platform for controlled synthesis of polymeric nanoparticles. *Nano Letters* **8**, 2906-2912, doi:10.1021/nl801736q (2008).
- 4 Ali, H. S. M., York, P. & Blagden, N. Preparation of hydrocortisone nanosuspension through a bottom-up nanoprecipitation technique using microfluidic reactors. *International Journal of Pharmaceutics* **375**, 107-113, doi:10.1016/j.ijpharm.2009.03.029 (2009).
- 5 Rondeau, E. & Cooper-White, J. J. Biopolymer microparticle and nanoparticle formation within a microfluidic device. *Langmuir* **24**, 6937-6945, doi:10.1021/la703339u (2008).
- 6 Valencia, P. M. *et al.* Single-Step Assembly of Homogenous Lipid - Polymeric and Lipid - Quantum Dot Nanoparticles Enabled by Microfluidic Rapid Mixing. *Acs Nano* **4**, 1671-1679, doi:10.1021/nn901433u (2010).
- 7 Kolishetti, N. *et al.* Engineering of self-assembled nanoparticle platform for precisely controlled combination drug therapy. *Proceedings of the National Academy of Sciences of the United States of America* **107**, 17939-17944, doi:10.1073/pnas.1011368107 (2010).
- 8 Mieszawska, A. J. *et al.* Synthesis of Polymer-Lipid Nanoparticles for Image-Guided Delivery of Dual Modality Therapy. *Bioconjugate Chemistry* **24**, 1429-1434, doi:10.1021/bc400166j (2013).
- 9 Capretto, L. *et al.* Mechanism of co-nanoprecipitation of organic actives and block copolymers in a microfluidic environment. *Nanotechnology* **23**, 16, doi:10.1088/0957-4484/23/37/375602 (2012).
- 10 Dashtimoghadam, E., Mirzadeh, H., Taromi, F. A. & Nystrom, B. Microfluidic self-assembly of polymeric nanoparticles with tunable compactness for controlled drug delivery. *Polymer* **54**, 4972-4979, doi:10.1016/j.polymer.2013.07.022 (2013).
- 11 Majedi, F. S. *et al.* Microfluidic assisted self-assembly of chitosan based nanoparticles as drug delivery agents. *Lab on a Chip* **13**, 204-207, doi:10.1039/c2lc41045a (2013).
- 12 Strijkers, G. J., Mulder, W. J. M., van Tilborg, G. A. F. & Nicolay, K. MRI contrast agents: Current status and future perspectives. *Anti-Cancer Agents in Medicinal Chemistry* **7**, 291-305, doi:10.2174/187152007780618135 (2007).
- 13 Collins, M. N. & Birkinshaw, C. Comparison of the effectiveness of four different crosslinking agents with hyaluronic acid hydrogel films for tissue-

- culture applications. *Journal of Applied Polymer Science* **104**, 3183-3191, doi:10.1002/app.25993 (2007).
- 14 Collins, M. N. & Birkinshaw, C. Investigation of the swelling behavior of crosslinked hyaluronic acid films and hydrogels produced using homogeneous reactions. *Journal of Applied Polymer Science* **109**, 923-931, doi:10.1002/app.27631 (2008).
- 15 Ibrahim, S., Kang, Q. K. & Ramamurthi, A. The impact of hyaluronic acid oligomer content on physical, mechanical, and biologic properties of divinyl sulfone-crosslinked hyaluronic acid hydrogels. *Journal of Biomedical Materials Research Part A* **94A**, 355-370, doi:10.1002/jbm.a.32704 (2010).
- 16 Martins Shimojo, A. A., Barbosa Pires, A. M., Lichy, R., Rodrigues, A. A. & Andrade Santana, M. H. The crosslinking degree controls the mechanical, rheological, and swelling properties of hyaluronic acid microparticles. *Journal of Biomedical Materials Research Part A* **103**, 730-737, doi:10.1002/jbm.a.35225 (2015).
- 17 Souza Bicudo, R. C. & Andrade Santana, M. H. Production of hyaluronic acid (HA) nanoparticles by a continuous process inside microchannels: Effects of non-solvents, organic phase flow rate, and HA concentration. *Chemical Engineering Science* **84**, 134-141, doi:10.1016/j.ces.2012.08.010 (2012).
- 18 Oh, E. J. *et al.* Control of the molecular degradation of hyaluronic acid hydrogels for tissue augmentation. *Journal of Biomedical Materials Research Part A* **86A**, 685-693, doi:10.1002/ibm.a.31681 (2008).
- 19 Russo, M., Bevilacqua, P., Netti, P. A. & Torino, E. A Microfluidic Platform to design crosslinked Hyaluronic Acid Nanoparticles (cHANPs) for enhanced MRI. *Scientific Reports* **6**, 37906, doi:10.1038/srep37906 <http://www.nature.com/articles/srep37906#supplementary-information> (2016).
- 20 Shimojo, A. A. M., Pires, A. M. B., Lichy, R. & Santana, M. H. A. The Performance of Crosslinking with Divinyl Sulfone as Controlled by the Interplay Between the Chemical Modification and Conformation of Hyaluronic Acid. *Journal of the Brazilian Chemical Society* **26**, 506-512, doi:10.5935/0103-5053.20150003 (2015).
- 21 Schante, C. E., Zuber, G., Herlin, C. & Vandamme, T. F. Chemical modifications of hyaluronic acid for the synthesis of derivatives for a broad range of biomedical applications. *Carbohydrate Polymers* **85**, 469-489, doi:10.1016/j.carbpol.2011.03.019 (2011).
- 22 Abdelwahed, W., Degobert, G., Stainmesse, S. & Fessi, H. Freeze-drying of nanoparticles: Formulation, process and storage considerations. *Advanced Drug Delivery Reviews* **58**, 1688-1713, doi:10.1016/j.addr.2006.09.017 (2006).
- 23 Ankrum, J. A. *et al.* Engineering cells with intracellular agent-loaded microparticles to control cell phenotype. *Nature Protocols* **9**, 233-245, doi:10.1038/nprot.2014.002 (2014).

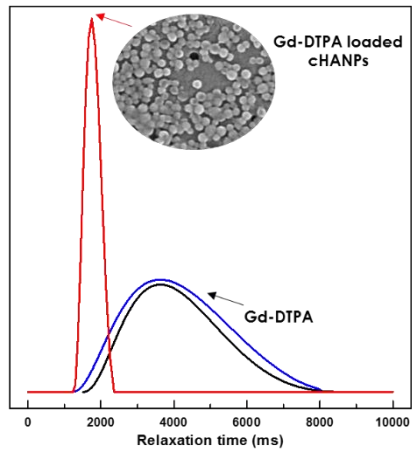
- 24 Yap, W. T. *et al.* Quantification of particle-conjugated or particle-encapsulated peptides on interfering reagent backgrounds. *Biotechniques* **57**, 39-44, doi:10.2144/000114190 (2014).
- 25 Capretto, L., Carugo, D., Mazzitelli, S., Nastruzzi, C. & Zhang, X. Microfluidic and lab-on-a-chip preparation routes for organic nanoparticles and vesicular systems for nanomedicine applications. *Advanced Drug Delivery Reviews* **65**, 1496-1532, doi:10.1016/j.addr.2013.08.002 (2013).
- 26 Hood, R. R. & DeVoe, D. L. High-Throughput Continuous Flow Production of Nanoscale Liposomes by Microfluidic Vertical Flow Focusing. *Small* **11**, 5790-5799, doi:10.1002/sml.201501345 (2015).
- 27 Mitragotri, S. & Lahann, J. Physical approaches to biomaterial design. *Nature Materials* **8**, 15-23, doi:10.1038/nmat2344 (2009).
- 28 Chen, K. J. *et al.* A small MRI contrast agent library of gadolinium(III)-encapsulated supramolecular nanoparticles for improved relaxivity and sensitivity. *Biomaterials* **32**, 2160-2165, doi:10.1016/j.biomaterials.2010.11.043 (2011).
- 29 Weissmann, B. & Meyer, K. The structure of hyalobiuronic acid and of hyaluronic acid from umbilical Cord1, 2. *Journal of the american chemical society* **76**, 1753-1757 (1954).
- 30 Gouin, S. & Winnik, F. M. Quantitative assays of the amount of diethylenetriaminepentaacetic acid conjugated to water-soluble polymers using isothermal titration calorimetry and colorimetry. *Bioconjugate Chemistry* **12**, 372-377, doi:10.1021/bc000109w (2001).
- 31 Joye, I. J. & McClements, D. J. Biopolymer-Based Delivery Systems: Challenges and Opportunities. *Current Topics in Medicinal Chemistry* **16**, 1026-1039, doi:10.2174/1568026615666150825143130 (2016).
- 32 Saravanakumar, G. *et al.* Hydrotropic hyaluronic acid conjugates: Synthesis, characterization, and implications as a carrier of paclitaxel. *International Journal of Pharmaceutics* **394**, 154-161, doi:10.1016/j.ijpharm.2010.04.041 (2010).
- 33 Choi, K. Y. *et al.* PEGylation of hyaluronic acid nanoparticles improves tumor targetability in vivo. *Biomaterials* **32**, 1880-1889, doi:10.1016/j.biomaterials.2010.11.010 (2011).
- 34 Jeong, C. G. *et al.* Screening of hyaluronic acid-poly(ethylene glycol) composite hydrogels to support intervertebral disc cell biosynthesis using artificial neural network analysis. *Acta Biomaterialia* **10**, 3421-3430, doi:10.1016/j.actbio.2014.05.012 (2014).
- 35 Jin, R. *et al.* Synthesis and characterization of hyaluronic acid-poly(ethylene glycol) hydrogels via Michael addition: An injectable biomaterial for cartilage repair. *Acta Biomaterialia* **6**, 1968-1977, doi:10.1016/j.actbio.2009.12.024 (2010).

III. CHAPTER III - Gd-DTPA loaded cHANPs for enhanced in vitro and in vivo MRI analysis

Abstract

Strategies to enhance relaxometric properties of clinically approved Magnetic Resonance Imaging (MRI) Gadolinium-based Contrast Agents (Gd-based CAs) without the chemical modification of the chelates have proved to be the most effective to impact suddenly on the diagnostic field. Here, a microfluidic platform is used to synthesize crosslinked Hyaluronic Acid NanoParticles (cHANPs) in which a clinically relevant MRI-CAs, Gd-DTPA is entrapped. The proposed crosslinked formulations

allow the control of the relaxometric properties of CAs, thus providing a boosting of the relaxation rate T_1 , since a T_1 of 1562 is achieved with a 10 μM of Gd-loaded cHANPs while a similar value is reached with 100 μM of the clinical relevant Gd-DTPA in solution. Results led us to identify this approach as an adjustable scenario to design intravascularly-injectable hydrogel nanoparticles entrapping Gd-DTPA thus overcoming general drawbacks of clinically approved CAs suffering from poor relaxivity and nephrotoxicity effects. The significant enhancement of signal intensity is observed in vitro and confirmed in vivo after PEGylation and peptide reactions.



Graphical Abstract III-1. Boosting of the relaxation time of the Gd-DTPA loaded cHANPs compared to Gd-DTPA “free” in water.

III.1 Background

III.1.1 Introduction

The Magnetic Resonance Imaging (MRI) represents the first-line diagnostic imaging modality for numerous indications. It provides high-resolution anatomic images of all body organs, including soft tissues and can be used for visualizing functions of cardiac, brain, and central nervous system, as well as detecting tumor. It is a clinically well-established, non-invasive technique that leverages the magnetic properties of water protons present in the body to produce three-dimensional whole body anatomical and functional images^{1,2}.

High magnetic fields (1.5 T and above) are clinically favoured because of their higher signal-to-noise ratio, capability for MR spectroscopy³ and other forms of functional MRI, such as high-speed imaging and high-resolution imaging. MRI signal intensity is related to the relaxation rate of in vivo water protons and can be enhanced by the administration of a contrast agent (CA) prior to scanning.

These CAs utilize paramagnetic metal ions to enhance the contrast in an MR image by positively influencing the relaxation rates of water protons in the immediate surroundings of the tissue in which they localize. The ability of CAs to effectively enhance image contrast depends on their relaxivity (longitudinal r_1 ; transversal r_2 ;) and the level of accumulation at the target site⁴.

Among different CAs, Gadolinium-based ones, used in up to 30% of clinical MRI scans⁵, consist of poly(amino carboxylate) complexes of

Gd ions, where Gd ions cytotoxicity is sequestered via chelation with ligands such as diethylenetriaminepentaacetic acid (DTPA) and tetraazacyclododecane-1,4,7,10-tetraacetic acid (DOTA)⁶⁻⁸. However, despite its certain role, Gadolinium-based CAs, like most of other clinically relevant CAs, suffer from poor sensitivity⁶ and rapid renal clearance, requiring long scan times, thus severely limiting the time window for MRI. In addition, they present low tissue specificity, leading to concerns in linking the use of these CAs with nephrogenic systemic fibrosis (NSF)⁹ and progressive accumulation in various central nervous system (CNS) structures following repeated gadolinium administration¹⁰.

To date, several efforts have increased tissue specificity, thus reducing nephrotoxicity, by designing architectures that entrap or conjugate CAs¹¹⁻²⁰. Recently, approaches using batch conventional synthesis were shown to successfully boost relaxivity by entrapping Gd-based CAs into biocompatible matrices, without chemically modifying the clinically approved Gd-chelates²¹⁻²³. Decuzzi et al.⁴ optimized the performance of MRI nanoconstructs by confining Gd-DTPA within porous structures of silicon microparticles (about 1-2 μm) produced by microfabrication. They examined the consequences of geometrical confinement of CAs within the nanopores, achieving a 2-3 times enhancement in r_1 without chemical modification of the chelate; however, a considerable increase of the relaxometric properties was observed only when nanotubes or fullerenes were also incorporated

into the silicon structure. Courant et al. enhanced relaxivity by encapsulating Gd-chelates (Gd-DOTA) into hydrophilic and biocompatible polymer nanoparticles (about 250 nm) obtained by the ionotropic gelation between Chitosan (CH) and Hyaluronic Acid (HA)²⁴.

Therefore, it is essential to highlight the need to build up a biocompatible system with higher relaxivity able to protect the chelate around Gd ions from transmetallation phenomena and control the accumulation and the clearance of the Gd-based CAs in a specific organ. Recently, in this perspective, we have exploited the impact of crosslinked and un-crosslinked biopolymer matrices on relaxometric properties of CAs where the contribution to the enhancement of CAs is highlighted and attributed to the reduced mobility of water within the hydrogel²⁵. However, systems with nanometric and monodisperse size under 100 nm are likely to improve delivery functions²⁶ to the tissues, stability of the metal chelates, and also provide enhanced relaxometric properties of the Gadolinium-based CAs.

Over the past decade, microfluidics has enabled the production of a variety of enhanced nanoparticles for applications in therapy and diagnostics^{27-37 38,39}. However, although great efforts have been made to apply microfluidic technologies to the production of nanoparticles, the exploitation of microfluidic approaches to support the design of nanostructures to improve relaxometric properties of clinically approved CAs for MRI has not been developed.

It is well known that the size, shape and size distribution of core nanoparticles affect the contrast resolution of MRI. Therefore, in the application of nanoparticle based MRI contrast agents, it is highly desirable to have uniform size of core material, which is one of the most important parameters. To address these demands, a microfluidic platform has been already presented as an ideal method to tightly control the final particle properties, i.e. size, polydispersity, entrapping of CAs etc., due to the process's ability to accurately control process parameters and thus enables efficient, continuous and tunable mixing⁴⁰⁻⁴⁶.

III.1.2 Aim of Chapter 3

In this Chapter, *in vitro* and *in vivo* MRI analysis of the Gd-loaded cHANPs obtained through the already discussed microfluidic platform are performed. We have presented that it is possible to achieve a fine-tuning of the mixing among all species and the control of their nanoprecipitation behaviour and crosslinking reaction. Now we demonstrate how the mixing also control the relaxometric properties of the contrast agents entrapping within the cHANPs. For both production strategies proposed to design Gd-loaded cHANPs, a considerable improvement in relaxation rate is found for DVS concentration at 4% v/v in the side channels and at 0.8% v/v in the middle channel. In particular, a T_1 of 1562 ms is achieved with 10 μM of Gd-loaded cHANPs suspension, while 100 μM of Gd-DTPA free in solution is required to achieve a comparable T_1 (about 1724 ms).

Indeed, the relaxation time reported for cHANPs is achieved with a concentration about 10 times lower than that of the free Gd-DTPA. This observation is crucial to lead potentially to a significant reduction of administration dosage on clinical usage of T₁ contrast agents and to gain advantages in the imaging modalities based on nanotechnologies. Also preliminary in vivo results clearly show the improvement of the MRI and confirm the stability of cHANPs. Gd-loaded cHANPs could potentially provide tissue specificity and reduce nephrotoxicity and, at the same time, they have the capability to retain Gd-based contrast agents to boost the MR signal without the chemical modification of the chelates. Later, we have performed and optimized a reaction of PEGylation and a decoration with peptide to aim a specific target.

III.2 Case Study

III.2.1 Experimental Section

III.2.1.1 Materials

Materials used for Gd-loaded cHANPs preparation were the same presented in *Chapter I* and *II*.

Materials used for the conjugation reaction: EDC (N-(3-Dimethylaminopropyl)-N'-ethylcarbodiimide, MW=191.70), NHS (N-Hydroxysuccinimide, MW=115.09) and Streptavidin (1mg/ml) were purchased from Sigma Aldrich Co. Cy7- PEG1KDa-NH₂, and Fitc- PEG1KDa-NH₂ were purchased from Nanocs Inc. Peptide pA20-36 (MW=1922, 1 mg/ml) was purchased from CASLO ApS.

The protein quantification assay, QuantiPro™ BCA assay kit and the WST-1 assay were purchased from Sigma Aldrich Co. Plasma from human P953 was purchased from Sigma Aldrich Co.

III.2.1.2 In vitro cytotoxicity

A adenocarcinomic human alveolar basal epithelial cells (A549) was used. The cells were cultured in Dulbecco's modified Eagle's medium (DMEM) containing 10% fetal calf serum and L-glutamine (2.9 mg/ml) at 37 °C in water-saturated air supplemented with 5% CO₂. For the cytotoxicity measurements, the cells were plated in 96-well plates for 24 hr before the addition of the nanoparticles. Fresh medium containing an increasing concentration of nanoparticles was added to each well and the cells were incubated for 24 h. At the end of the incubation time, the cytotoxicity of the nanoparticles was tested using an WST-1 assay (SIGMA-ALDRICH, MI). Briefly, phosphate-buffered saline (PBS) containing WST-1 was added to each well and the cells were incubated for 30 min, 1 hr, 2 hr, 4 hr, 12 hr and 24 hr. Spectral absorption of the samples were measured at 450 nm with ELISA Reader (Biotek, Winooski, VT). The number of live cells is proportional to the amount of formazan produced.

III.2.1.3 In vitro MRI

Unloaded and Gd-loaded cHANPs at different concentrations were tested by in vitro MRI and results were compared with Magnevist, Gd-DTPA in water as a control. After vigorously stirring, changes in relaxation time (T₁ and T₂) were evaluated at two different magnetic

fields, 1.5 T and 3 T in a Clinical Magnetic Resonance (Philips Achieva 1.5T and 3T) using Sense Head 8 coil and by Minispec Bench Top Relaxometer at 1.5 T (Bruker corporation) by adding 300 μL of the sample to a specific tube³⁵. For T_1 measurement by the clinical instruments, the inversion recovery sequence was used with the following parameters: repetition time $\text{TR}= 2500$ ms; echo time $\text{TE}=12$ ms; inversion time $\text{TI}=50, 100, 200, 400, 800, 1100, 1800$ ms; $\text{FOV}= 180 \times 146$ mm; slice thickness= 4 mm, acquisition matrix= 360×292 . Only modulus images were recorded and were loaded on MR map. T_1 maps can be generated from sets of inversion recovery images (multiple series, each containing one image) with varying inversion time (TI), After sorting the images by their corresponding TI, a 3-parameter curve fitting using a Levenberg-Marquardt algorithm is performed for each pixel position where signal intensity of any of the corresponding source pixels is above the user-defined noise level. Therefore, MR_map performs several cycles of additional curve fittings on the whole data set, where each time the signs of the signal in an increasing number of leading images are switched to negative, starting with the image with the lowest TI and finishing with the last image where $\text{TI} < 0.67 \times \text{limit } T_1$ (ms). Finally, the combination of signs yielding the best (= lowest) Chi value during the curve fitting process was selected and its curve fitting results were used to reconstruct the map. Finally, relaxivity r_1 was calculated using weighted linear regression ($R_1=1/T_1 \text{ s}^{-1}$ relaxation rate plotted against

Gd concentration, mM, and r_1 , $\text{mM}^{-1} \text{s}^{-1}$, is the slope of the fitted curve). Estimation of measurement uncertainty was evaluated using weighted linear regression. Furthermore, the relaxation time distribution was obtained by CONTIN Algorithm. The relaxation spectrum was normalized with respect to the CONTIN processing parameters. The integral of a peak corresponds therefore to the contribution of the species exhibiting this peculiar relaxation to the relaxation time spectrum⁴⁷.

III.2.1.4 Sorption of Gd-DTPA

Later, Gd-DTPA was also adsorbed to empty cHANPs by placing cHANPs in Gd-DTPA solution. Briefly, a solution of Gd-DTPA 180 μM was dissolved in the same volume of cHANPs solution and the suspension was placed on wheel for 48 hr in order to get maximum sorption of Gd-DTPA on NPs mainly through diffusion. Since the concentration of Gd-DTPA was higher outside the NPs than inside the NPs, Gd-DTPA diffuses from external solution to the cHANPs polymer matrix. Then, the sample was dialyzed against water in dialysis membrane bag of 50000 MCWO for 12 hr. The concentration of Gd-DTPA from the external medium of dialysis bag, treated by evaporator, was calculated by T_1 value measured at 37°C on Bruker Minispec mq60 instrument using standard inversion-recovery pulse sequence. Later the content of gadolinium adsorbed on NPs was calculated by subtracting the amount of gadolinium in the external

medium from the total amount of Gd-DTPA which had been added in the system.

III.2.1.5 In vitro stability in plasma

The in vitro stability of the test compounds was studied in human plasma. The plasma was reconstructed following the protocol reported from Sigma Aldrich Co. After, the plasma was activated at 37 °C in a shaking water bath for 20 min. 100 µL of cHANPs was mixed with 100 µL of PBS. The assays were performed in a shaking water bath at 37°C and conducted in triplicate. Samples (50 µL) were taken at 0, 15, 30, 45, 60, 90 min. The samples were subjected to vortex mixing for 1 min and then centrifugation at 4°C for 15 min at 14,000 rpm. The clear supernatants were analyzed by HPLC. The in vitro plasma half-life ($t_{1/2}$) was calculated using the expression $t_{1/2}=0.693/b$, where b is the slope found in the linear fit of the natural logarithm of the fraction remaining of the parent compound vs. incubation time.

III.2.1.6 Quantification of carboxyl groups on the surface of cHANPs

Back titration method was performed to directly quantify carboxylic groups on the surface of cHANPs. In brief, 10 mL of cHANPs (0.1 mg/mL) was dispersed in 20 mL of 0.01 M NaOH solution, stirred for 30 min and then pH annotated. A standard solution of 0.01 mM HCl, was used as the titrant. After each addition of titrant the solution was stirred magnetically for 1 min and the pH was recorded. From the difference of NaOH and HCl concentration at equivalent point, the

molar concentration of carboxylic sites was calculated. The titration was repeated on a second NP sample to check for reproducibility.

III.2.1.7 Direct conjugation with PEG-NH₂-Dye

The formation of an amide bond between the COOH groups on the nanoparticle surface and the -NH₂ end groups of the PEG labeled with fluorophore was adopted as a strategy of attack to carry out the reaction of direct PEGylation. Especially for each reaction, PEG1KDa amino and labeled with different fluorophores (Cy7-PEG1KDa-NH₂, FITC-PEG1KDa-NH₂) were used. The activation of the carboxylated surface of the cHANPs was occurred after contact for 10 minutes with 500 μ L of the starting sample to a solution of EDC (230 μ L at 70 mM) and NHS (230 μ L at 21 mM). Thereafter, 2mM of NH₂-PEG1KDa-Dye was added, allowing to react in the dark for 4 hours and in a slight rotation. The excess reagents were removed by ultracentrifugation (30.000 rpm, 15°C, 10 min) or spin-x corning system (4000 rpm, 20°C, 10 min) and the pellet was suspended in a phosphate buffer (pH 6.8). The amount of reagents was stabilized basing on the quantification, carried out by titration of the carboxyl groups available on the surface of the cHANPs.

III.2.1.8 Indirect conjugation streptavidin-biotin-peptide

The streptavidin-biotin bond was adopted as a strategy of attack to make the conjugation of the peptide to the nanoparticle surface. For this purpose, the peptide pA20-36 (EYVNCNLDLVGNCVIRG, MW 1922 Da), due to the presence of a C-ter of biotin molecule position,

has been previously conjugated to streptavidinate nanoparticles. Therefore, the surface of the nanoparticle, first, has been activated with EDC (0.0155 $\mu\text{mol/mL}$) and NHS (0.13 $\mu\text{mol/mL}$) for 10 minutes, then the streptavidin (0.006 $\mu\text{mol/mL}$) was added and allowed to react overnight in a slight stirring. After removal of the excess reagents by different methods of purification, the peptide (0.02 $\mu\text{mol/mL}$) to be conjugated was added to the resulting pellet suspended in PBS. The reaction was left for 4 hours under stirring, and finally a further purification was carried out to remove the excess peptide. The collected material was resuspended in PBS.

III.2.1.9 Direct conjugation with peptide

500 μL of cHANPs were reacted with EDC and NHS. Since the EDC/NHS excesses were in equilibrium with the aqueous environment and provide no interference with the next step reaction, they have not been removed. After 15 minutes, the peptide (0.020 $\mu\text{mol/mL}$), previously deactivated with TEA, was added directly to the reaction. Reactions were kept in agitation by a rotating shaker. After 4 hours, the excess peptide was removed by various purification methods.

III.2.1.10 Quantification of PEG concentration

The amount of PEG conjugated to cHANPs was determined by spectrofluorimetric (ENSPiRE Multimode Plate Reader PerkinElmer). All measurements were performed in triplicate. The

calibration line was set in the range of 0-80 nmol/mL (Ex/Em 480-550).

III.2.1.11 BCA assay

BCA assay, which results to be extremely precise and sensitive being able to detect the amount of protein of 0.5 g/mL, was used to measure the concentration of the peptide on the surface of the cHANPs. It is based on the principle that under alkaline conditions the copper Cu^{2+} ions form a complex with peptide bonds of proteins and are reduced to Cu^+ . The bicinchoninic acid, under alkaline conditions, is a highly sensitive reagent, stable and specific for the Cu^+ , and form with it a compound of purple colour and its intensity is proportional to the amount of protein present. The intensity variation is determined by absorbance measurements in a spectrophotometer at 562 nm. As expected, 150 μL of the cHANPs suspension were reacted with equal amount of working reagent solution and the mixture was incubated at 37°C for 2 h. The results were compared with a BSA calibration curve and the concentration value was then extrapolated by a straight line of calibration built using bovine serum albumin samples of known concentration (0 - 40 mg/mL). All measurements were performed in triplicate.

III.2.1.12 In vivo MRI

Unloaded cHANPs have been preliminary tested in vivo to evaluate the acute and chronic toxicity on C57-bulb mice model. In details, the chronic toxicity tests have been assessed by injecting 200 μL of

unloaded and loaded cHANPs intravenously at 1 hr, 24 hr, 48 hr and after 40 days. Experiments have been repeated in triplicate.

Later, for T₁ measurement, the in vivo experiments for loaded cHANPs were conducted by PET/MRI 3T Siemens instrumentation with a dose of 150 µL applying an Inversion Recovery (IR) sequence (*VOF= 100x75 mm; slice thickness=1.2 mm without GAP, contiguous slice, acquisition matrix=192x144; Averages: 6; Turbo spin-echo; Sequence duration: 10 minutes -36 seconds; Signal to Noise Ratio: 1; Spatial Resolution: 0.5 x 0.5; TR: 550; TE: 11*). A basal acquisition has been conducted for all subjects before the injection protocol.

The biodistribution analysis have been made at different time points: 45 minutes, 3 hr, 6hr, 8 hr, and for 24hr. Experiments have been repeated in triplicate. After the MRI scans, the blood and tissue samples were collected at predetermined sampling points. Quantitative analysis has been made by digesting and homogenizing the organ with nitric acid at 100°C for at least 3 hr. Later, the samples are diluted and the liquid analyzed by ICP-MS with the same protocol described in the paragraph *II.2.1.2*.

All studies were performed with mice under general anesthesia, obtained with an intraperitoneal injection of tribromoethanol solution at a final concentration of 12.5 mg/mL and administered at a dose of about 250 mg/kg. Once anesthetized, mice were prepared for venous cannulation by bathing the whole tail in tap water warmed at 39 °C to obtain proper vasodilation. A lab-made catheter, consisting of a 30 G

needle mounted on a polyethylene tube, was delicately advanced in one of the lateral caudal veins, until blood could be seen in the tube. Hence, two-three drops of surgical glue were spilled on the needle /tail interface area and let dry. The tube was flushed with 20 μL of a heparinized solution and the tip of the tube was closed to avoid further bleeding. The mice were then positioned on magnetic compatible bedding within a head coil and the baseline acquisition was performed. Hereafter, 150 μL of the contrast agent solution was slowly injected, following any eventual reaction of the mouse or any change in the respiratory pattern. Acquisition were performed every 10 minutes till one hour post injection, and then after 3, 6, 8 and 24 hr. Two solutions were studied: Gd-loaded cHANPs and Gd-DTPA. In each solution, the final Gd concentration was the same.

The DICOM files of each acquisition were stored on an external unit. The files were imported in dedicated software for imaging analysis (OsiriX© Lite, Pixmeo SARL, Bernex, Switzerland). A circular region of interest (ROI) of about 2 mm^2 was drawn and then saved, to be used in the analysis of all images. The anatomic areas studied were: renal cortices and medullas, the urinary bladder, the salivary glands. The mean intensity obtained for each organ (IO) was normalized to the mean muscle intensity (IM) applying the formula: $\text{IO}_{\text{norm}} = \text{IO}/\text{IM}$, and the result was used to calculate the percentage of contrast enhancement (% CE) according to Corbin et al.⁴⁸ $\% \text{ CE} = (\text{I}_{\text{post}} - \text{I}_{\text{pre}}) / \text{I}_{\text{pre}} * 100$.

III.2.2 Results and Discussion

III.2.2.1 In vitro cytotoxicity

Typically, structural alterations of nanoparticles in aqueous solutions, in cell-culture medium, might also affect and change the final results of the in vitro toxicological studies. Therefore, cytotoxicity tests are essential to assess preliminarily the biocompatibility of the cHANPs. Likewise, the surface charge of NPs plays an especially important role in cell–NP interactions because cell membranes themselves are charged. Understanding the behavior of NPs at the time of toxicological assay may play a crucial role in the interpretation of its results. Nasti et al. suggest that the cytotoxicity of chitosan/TPP nanoparticles is a function of their surface composition/charge because the HA-coating reduces the cytotoxicity while the positively charged nanoparticles are more rapidly internalized than those of opposite charge. The mechanical stability and the enzymatic degradation of the nanoparticles is determined by the degree of crosslinking of HA structures. As highlighted by studies of Lai, HA sheets incorporated different concentrations of DVS in a range between 0 and 50 mM had a good cytocompatibility². For this study, the toxicity of loaded cHANPs is tested using a WST-1 assay, which is based on the conversion of a water-soluble tetrazolium salt (yellowish in color) to water insoluble formazan (purple color) by living cells. Scalar concentrations of cHANPs are tested in a range

between 10 $\mu\text{g/mL}$ and 100 $\mu\text{g/mL}$. It is evident that the cHANPs showed no detectable cytotoxicity in vitro (Figure III-1).

The varied NP–cellular localization and interaction might lead to various modes of toxicity. Even NPs of the same material can show completely different intracellular behavior due to, for example, slight differences in surface coating, charge and size. It has been reported that especially the NP size determines the efficiency of cellular uptake and subsequent intracellular processing.

The disruption of the NPs inside the cell greatly influences the resulting toxic effects. The cytotoxicity could be attributed to the chemical composition of the nanostructure, but it should be considered that the NPs destabilization results in the release of their content into intracellular compartments, which can present synergic cytotoxic effects. This cytotoxicity can be desired, in antitumor treatments, or undesired during NPs application for diagnostics purposes. Furthermore, an excellent cell uptake of the NPs guarantees the efficient cell MRI and intracellular drug delivery.

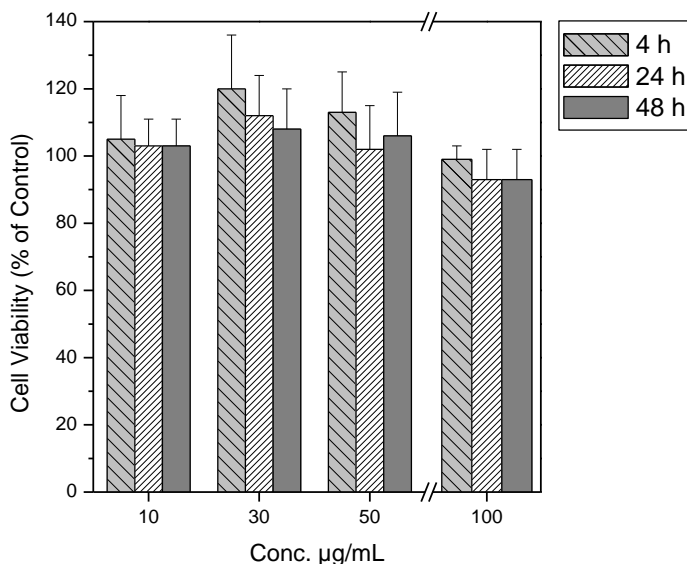


Figure III-1. *In vitro* cytotoxicity. A549 cell viability expressed as a percentage of the value obtained with a concentration of cHANPs in a range between 10 µg/mL and 100 µg/mL for three different time intervals. The error bars represent the standard deviations calculated from three independent experiments.

III.2.2.2 *In vitro* MRI

Given the versatility of our cHANPs, it is of particular interest to investigate how the selection of the different crosslinking reaction's strategies, presented into the Chapter II, could result in advanced and tailorable CAs-loading functionalities.

In vitro relaxivity is studied for loaded and unloaded cHANPs and the results are presented for Gd-DTPA in water at different concentrations. For all MR instruments, T_1 values measured on

Gd-loaded cHANPs show a higher relaxation rate compared to the relative “free” contrast agent, confirming that active compounds are not only dispersed or encapsulated but even wrapped within the hydrogel polymer matrix of cHANPs. It is also observed that reaction strategies can not only affect the stability and degradation behavior but even the MR functionality. The relaxation time values of Gd-DTPA and cHANPs are first calculated at 37 °C and 1.5 T (Minispec mq60). A notable change in relaxation rate is found for Gd-loaded cHANPs obtained by adding DVS in the side channels (C_{DVS} at 4% v/v) and in the middle channel (C_{DVS} 0.8% v/v). Comparison between the relaxation time distributions of loaded cHANPs, at the same concentration of Gd-DTPA in HA solution, is reported in Figure III-2 and Table III-1. Results clearly show that the relaxation time for Gd-DTPA entrapped within cHANPs is shorter than that of the “free” contrast agent. By tuning the process parameters and adjusting the crosslinking reaction, a T_1 of 1562 ms is achieved with 10 μ M of Gd-loaded cHANPs suspension, while 100 μ M of Gd-DTPA free in solution is required to achieve a comparable T_1 . Indeed, the relaxation time reported for cHANPs is achieved with a concentration about 10 times lower than that of the free Gd-DTPA. The value related to the unloaded cHANPs is also reported, proving that the nanoparticles do not contribute themselves to the relaxivity.

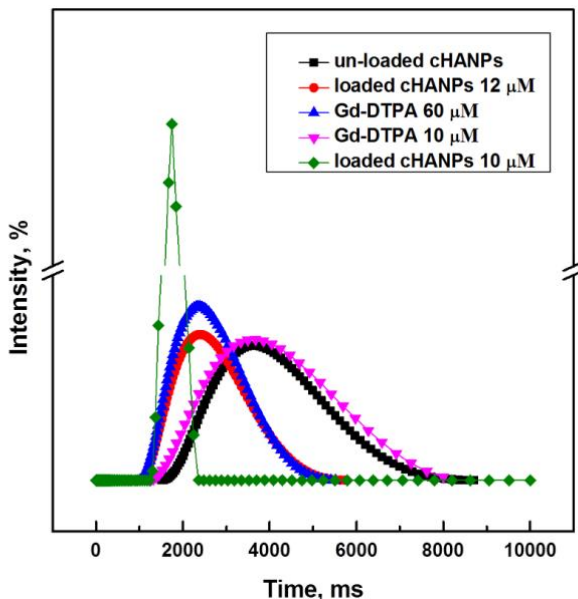


Figure III-2. In vitro relaxation time distribution. Relaxation time distribution reported for: Gd-DTPA in water solution at (-▼-) 10 μM , (-▲-) 60 μM and (-◀-) 100 μM ; un-loaded cHANPs (-■-); loaded cHANPs at *standard conditions* obtained using (-●-) 4% v/v DVS in the side channels, at pH 12.3, reported at 12 μM of Gd-DTPA, (-◆-) 0.8 % v/v DVS and C_{span80} 0,5v/v in the middle channel, reported at Gd-DTPA of 10 μM .

	C_{CAs} [μM]	T_1 [ms]	$1/T_1$ [ms^{-1}]
Milli-Q water	0	3800	0.26
un-loaded cHANPs	0	3600	0.27
Gd-DTPA	10	3380	0.29
Gd-DTPA	60	2111	0.47
Gd-DTPA	100	1724	0.58
loaded cHANPs 4% v/v DVS side channels	12	2170	0.46
loaded cHANPs 0.8% v/v DVS middle channel	10	1562	0.64

Table III-1. Relaxation time analysis. Data obtained performing relaxation time measurements are reported showing an increase of $1/T_1$ values compared to the free Gd-DTPA in water. cHANPs obtained by adding DVS (4% v/v) in the side channels and DVS (0.8 % v/v) in the middle channel, at *standard conditions* and pH of 12.3. Each relaxation time measurement is repeated at least 10 times and shows a standard deviation lower than 10 %.

Results are also confirmed using a clinical MRI instrumentation 1.5 T and 3 T. Indeed, loaded-cHANPs, obtained by adding DVS in the middle channel (0.8% v/v) and in the side channels (4% v/v), show a maximum r_1 relaxivity of about $48.97 \text{ mM}^{-1}\text{s}^{-1}$ and

14.09 $\text{mM}^{-1}\text{s}^{-1}$, respectively. Both values are considerably higher than the value of $3.9 \text{ mM}^{-1} \text{ s}^{-1}$ reported for commercial Magnevist (Figure III-3).

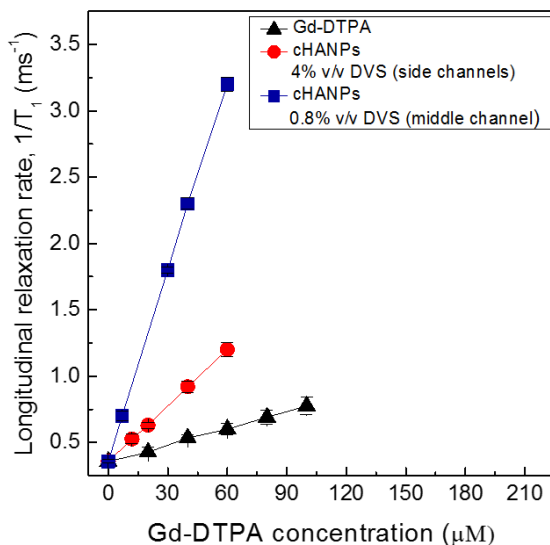


Figure III-3. In vitro MRI. Longitudinal relaxation rate ($1/T_1$) versus Gd-DTPA concentration for (-▲-) free Gd-DTPA in water and for Gd-DTPA loaded cHANPs obtained by injecting DVS (-●-) in the side channels and (-■-) in the middle channel, showing a relaxivity of $3.9 \text{ mM}^{-1}\text{s}^{-1}$, $14.09 \text{ mM}^{-1}\text{s}^{-1}$ and $48.97 \text{ mM}^{-1}\text{s}^{-1}$ respectively.

As well-known⁴⁹, the relaxivity is defined as the rate of change in relaxation times of the water protons per mM concentration of metal ions. Larger is the relaxivity of a given CA and larger is the induced spin-lattice relaxation time T_1 and spin-spin relaxation time T_2 shortening. In the presence of CAs, T_1 and T_2 may be shortened considerably. However, an increase in contrast

agent concentration provides an increase in signal intensity due to the effect on T_1 until a certain optimal concentration is reached while further increase in concentration reduces the signal because of a broad effect on T_2 , producing as net result a non-linear relation. This peculiar behaviour dictates their use in clinical practice, preferring contrast agents that have a relatively greater effect on T_1 than on T_2 and reveals the enormous advantage of manipulating clinical relevant contrast agents with enhanced MRI sensitivity. The relaxation times of the selected cHANPs samples remain unchanged at standard physiological conditions for at least 5 days after sample preparation, ensuring no leakage of Gd-DTPA from the cHANPs during MRI acquisitions.

Additionally, a significant difference can also be found in the relaxation time distributions reported for both strategies in Figure III-4. We notice that it is possible to modulate the T_1 by changing the DVS concentration within the same strategy. This is particularly evident when DVS is added to the middle channel, because any variation in DVS concentrations corresponds a change in the relaxation rates distribution of the produced nanoparticles.

However, at a value of DVS concentration of 0.8% v/v a narrow relaxation time distribution is obtained demonstrating optimal equilibrium conditions to boost the MRI signal.

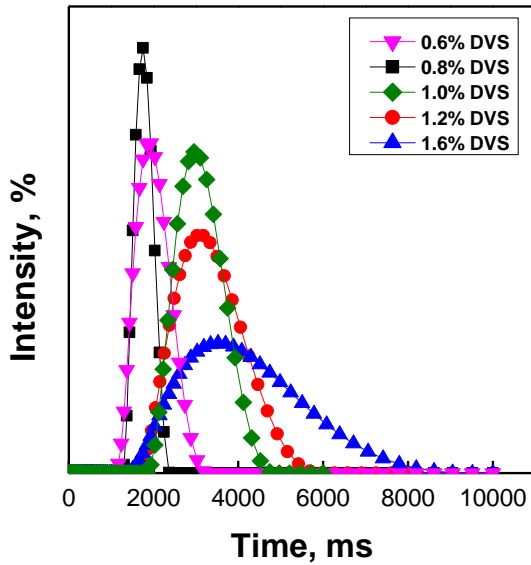


Figure III-4. Relaxation time distribution reported for Gd-DTPA loaded cHANPs obtained by adding DVS in the middle channel, at Span 80 0.5 % v/v, at Gd-DTPA 0.1 %wt/v at standard flow conditions.

For completeness, we have also evaluated the relaxivity of unloaded cHANPs compared with free Gd-DTPA in water showing that they do not contribute to the enhancement of MRI signal (Figure III-5).

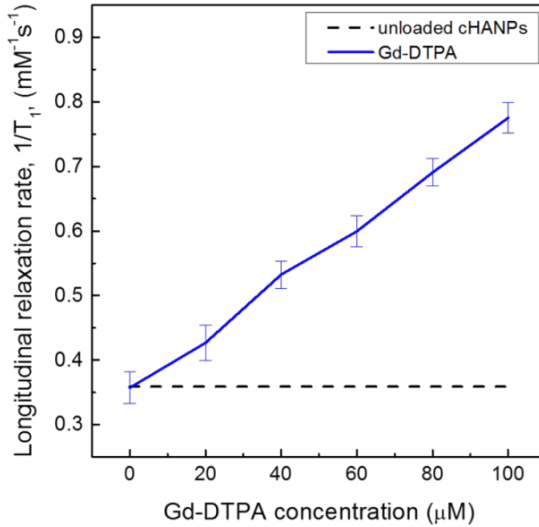


Figure III-5. Relaxometric properties of unloaded cHANPs. The relaxation time measurements versus Gd-DTPA concentration show that the unloaded cHANPs do not contribute to the enhancement of MRI signal.

III.2.2.3 Sorption of Gd-DTPA

In this sorption analysis, detailed into the experimental section, the release of Gd-DTPA is very fast and there is no enhancement in MRI signal at the same concentration of Gd-DTPA in water. Furthermore, the adding of Gd-DTPA alters the morphology of formed cHANPs (Figure III-6). However, after the sorption, no enhanced relaxivity is observed compared to the free Gd-DTPA, but partial release of the Gd^{3+} ions is observed even after 12 h.

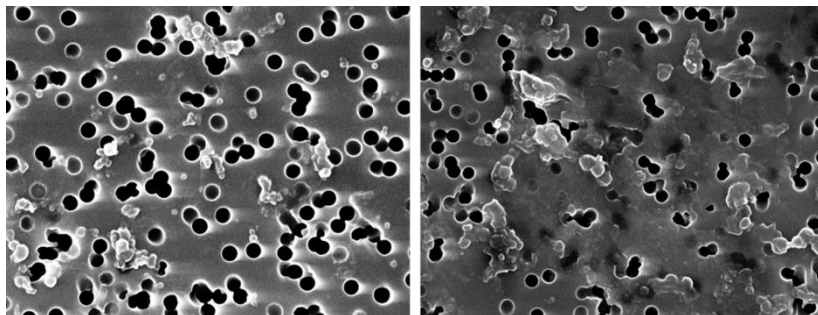


Figure III-6. FE-SEM images of cHANPs obtained by nanoprecipitation in hydrodynamic flow focusing and treated by sorption of Gd-DTPA.

III.2.2.4 Direct conjugation with PEG-NH₂ -dye

For in vivo applications, to potentially reduce adhesive interactions of colloids with intracellular components, the surface of cHANPs has been coated with polyethylene glycol (PEG). PEG is a coiled polymer of repeating ethylene ether units with dynamic conformations. This polymer is non-toxic, non-immunogenic, non-antigenic, highly soluble in water and FDA approved. In both drug-delivery and imaging applications, the addition of PEG to NPs reduces RES uptake and increases circulation time versus uncoated counterparts. Indeed, the PEGylation has several advantages: a prolonged residence in body, a decreased degradation by metabolic enzymes and a reduction or elimination of protein immunogenicity.

Using back titration, the concentration of carboxylic groups is determined by making them to react with an excess volume of base solution at a known concentration and then titrating the resulting mixture with the standardized acid solution. To optimize PEGylation

reaction, we first perform quantitative characterization of carboxyl functionalities of cHANPs. Using back titration, we can quantify the number of surface functionalities, providing important information about the surface physicochemical properties and the effects on the quality and reproducibility of the functional nanomaterial. We estimate about 15 nmol of carboxylic group/mg of NP.

As expected, PEGylation produces a chemical decoration of the particles inducing a larger nanoparticle size distribution due to the PEG-corona. Indeed, the measured size of the cHANPs decorated with PEG-FITC (1KDa) is of about 60 nm diameter. Previously zeta potential results demonstrated that cHANPs have a negatively charged surfaces (-40 mV), attributed to the presence of deprotonated carboxyl groups of HA. In details, PEGylation reduces the carboxylic groups from 15 ± 2.5 nmol/mL to 7 ± 1.5 nmol/mL, proving that some COOH- groups are still not conjugated. It could be since using titration we have also quantified carboxylic groups not exposed on the nanoparticle surface, that were not available for the PEGylation reaction due to the high molecular weight of the PEG. However, as expected, the zeta potential of the nanoparticles was slightly decreased by PEGylation (-15 mV), caused by the consumption of carboxylic acids at the backbone of HA. PEGylation is also useful to assess the surface stability of the nanoparticles during the chemical decoration and the ability to retain the loaded Gd compound during the bioconjugation. cHANPs subjected to direct PEGylation have

maintained their structural integrity despite the presence of a higher surface roughness and a slight increment in size. TEM and STED images (Figure III-7 and Figure III-8) show the presence of an outer covering coating.

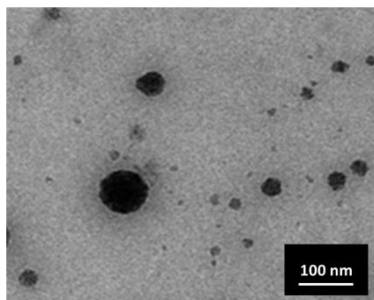


Figure III-7. TEM image of cHANPs after direct PEGylation reaction.

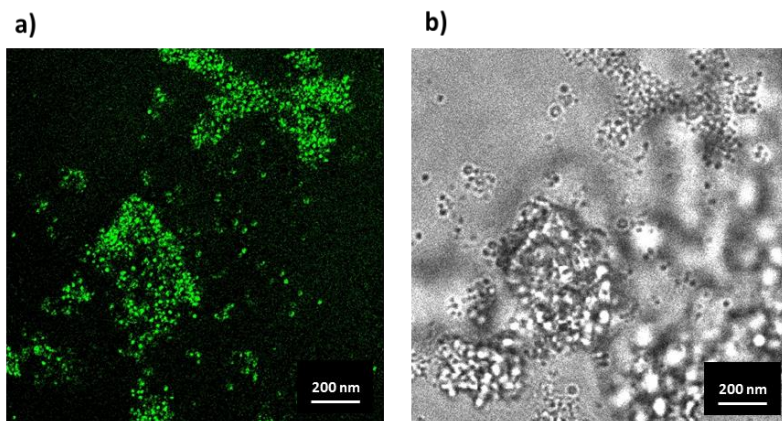


Figure III-8. Images of cHANPs after functionalization with NH₂-PEG1KDa-FITC. The same image is reported in a) fluorescence and in b) transmittance light.

We have also measured the pH variation of the cHANPs during the reaction, as follow detailed:

- pH pre-reaction 5.85
- pH post EDC 5.80
- pH post PEG (time 0) 5.43
- pH-post PEG (time Over night) 7.04

III.2.2.5 Direct conjugation with peptide pA20-36

cHANPs subjected to direct conjugation with peptide pA20-36 have maintained their stable morphology. Also in this case, it is possible to appreciate the presence of confirmed outer coating by TEM analysis (Figure III-9).

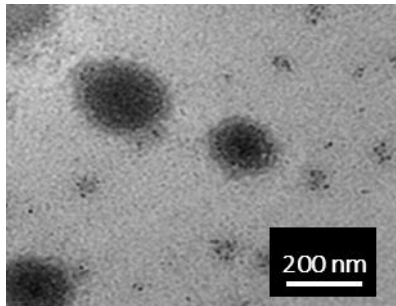


Figure III-9. TEM image of cHANPs after direct conjugation with peptide pA20-36.

III.2.2.6 Indirect conjugation with peptide pA20-36

To increase the amount of conjugated peptide, cHANPs are subjected also to indirect conjugation. In this condition, they have not suffered from alterations in the morphology, but it is possible to appreciate an increase in the size evidenced by the presence of a double coating layer consisting of the streptavidin-biotin-peptide complex observable by TEM analysis (Figure III-10).

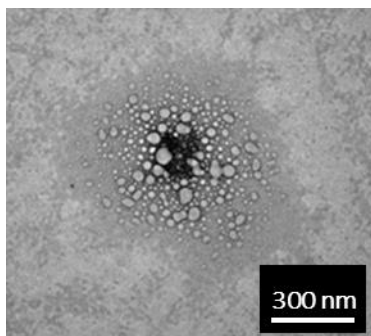


Figure III-10. TEM image of cHANPs after indirect conjugation with peptide pA20-36.

III.2.2.7 Toxicity study in vivo

Results of acute and chronic toxicity tests in the short and long period, conducted for loaded and unloaded cHANPs, have proven the biocompatibility of the proposed nanostructures even after several administrations. The animals are breathing regularly and eating normally.

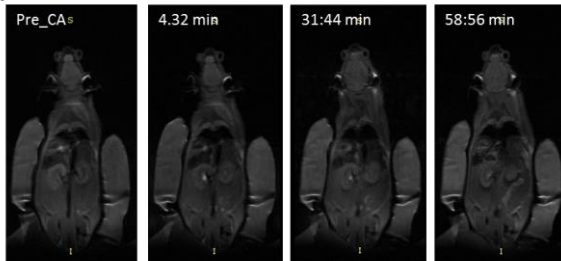
III.2.2.8 In vivo MRI

For in vivo MRI analysis, a basal acquisition (Standard MRI protocol) has been conducted on pre-clinical 9.4 T MRI instrumentation for all subjects before the injection protocol as reported in the experimental section.

Figure III-11 and Figure III-12 show the coronal view MRI images of a mouse C57bulb injected with Gd-DTPA and Gd-loaded cHANPs. Figure III-11a, Figure III-12a represent mice injected with only Gd-DTPA at 800 μM , while Figure III-11b and Figure III-12b report Gd-loaded cHANPs at 10 μM at different time intervals. Figures report an

acquired slice of kidney and bladder respectively. Image Analysis related to the injection of Gd-DTPA at 150 μM are not reported because the signal is not appreciable.

a) Gd-DTPA, 800 μM



b) cHANPs, 10 μM

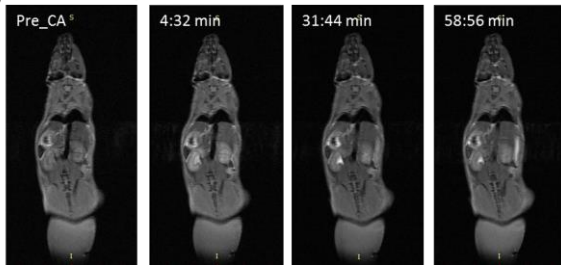
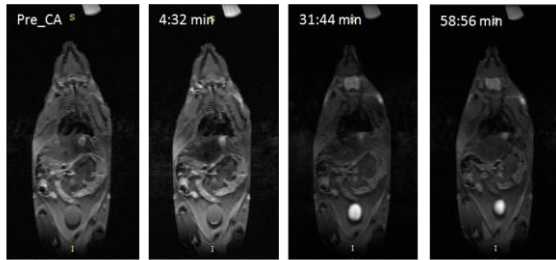


Figure III-11. In vivo MRI. Qualitative Image Analysis for kidney at different time intervals after injection of a) Gd-DTPA at 800 μM ; and of b) Gd-DTPA loaded cHANPs at 10 μM

a) Gd-DTPA, 800 μ M



b) cHANPs, 10 μ M

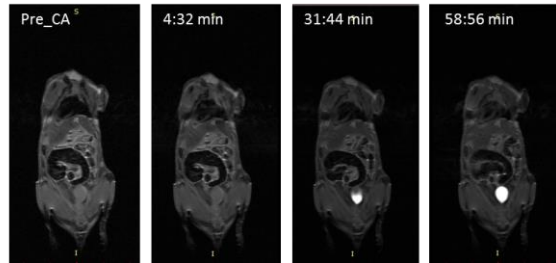


Figure III-12. In vivo MRI. Qualitative Image Analysis for bladder at different time intervals after injection of a) Gd-DTPA at 800 μ M; and of b) Gd-DTPA loaded cHANPs at 10 μ M

While the experiments are performed, no side effects of the used CAs are observed. As showed in Figure III-13, because of the elimination of the Gd-DTPA is by renal clearance, the kidney shows a lighter image compared to other tissues. After about 4 min from Gd-DTPA injection, the kidney appears brightened and the signal intensity reaches the maximum of intensity of 62 %, followed by rapid decay. After injection for 1 h, the signal intensity of the whole mice body tends to the normality. Because of the duration time of acquisition used the signal intensity in the heart or liver is not visible. The urinary bladder becomes lighter after 6 min from injection, the maximum

value of signal intensity (343 %) is recorder after 45 min from Gd-DTPA administration and remains high to 1 hr, while the whole mice body returns to appear normal.

Also after injection of Gd-loaded cHANPs the signal intensity in the kidney immediately increases. The enhanced signal intensity is detectable after 3 min, it reaches to the highest (82%) at 48 min and remains visible to 1 h after i.v.

In conclusion, preliminary in vivo results clearly demonstrate the improvement of the MRI signal and confirm the stability of cHANPs ensuring no release of Gd-DTPA during the time course of the relaxation measurements (Figure III-13, Figure III-14).

It is also important to highlight the higher persistence of the MRI signal in the case of Gd-loaded cHANPs compared to the free Gd-DTPA in water Figure III-13 and Figure III-14.

Gd-DTPA loaded cHANPs for enhanced in vitro and in vivo MRI analysis

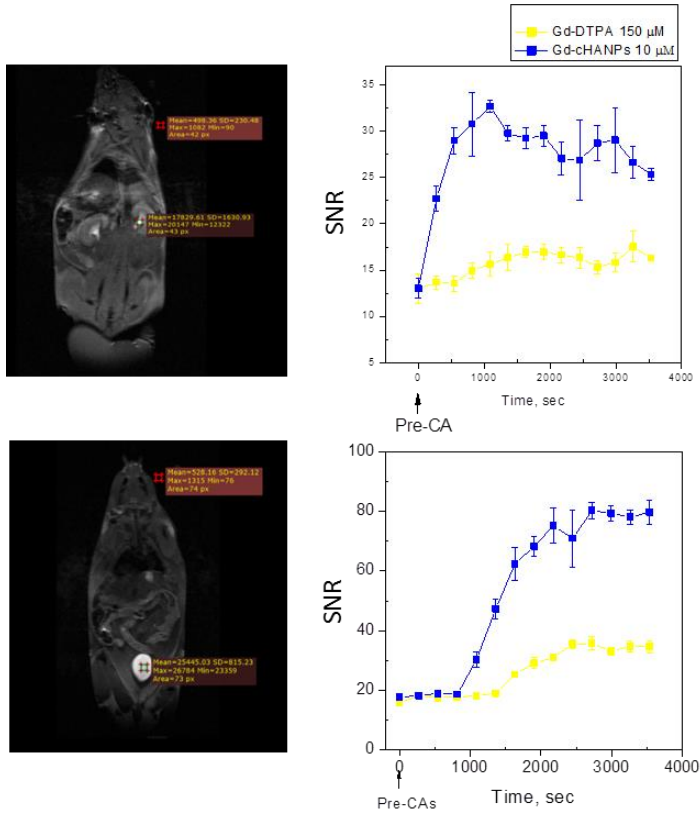


Figure III-13. In vivo MRI. Quantitative Image Analysis at different time intervals after injection of Gd-DTPA at 150 μ M and of Gd-DTPA loaded cHANPs at 10 μ M for a) kidney and b) bladder.

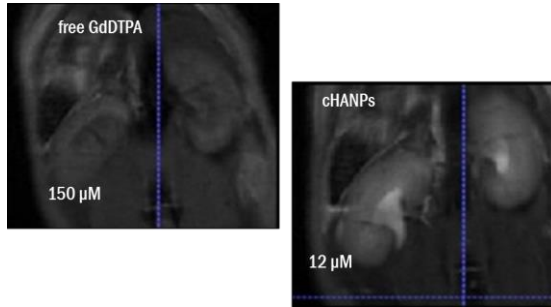


Figure III-14. In vivo MRI. Qualitative Image Analysis

Same analysis is conducted on a PET/MRI 3 T scanner to evaluate the % contrast enhancement (CE) of the images for a scanner used in a clinical practice. In details, a multivariate analysis of variance for repeated measures (RM-MANOVA) is used to study the selected parameters of the treatment group with Gd-loaded cHANPs and Gd-DTPA. No significant effect of the treatment group could be detected for renal medulla (0.96) and salivary glands ($P=0.65$). The urine % CE resulted significantly affected by the interaction of time over group ($P=0.0008$), with the cHANPs having the highest % CE than Gd-DTPA treated mice. A significant difference between groups was detected for the renal cortex ($P=0.03$) and a significant effect of the interaction of time over group ($P=0.0007$) is recorded, as well, with cHANPs showing a higher and increasing % CE from 10 minute to 1 hour.

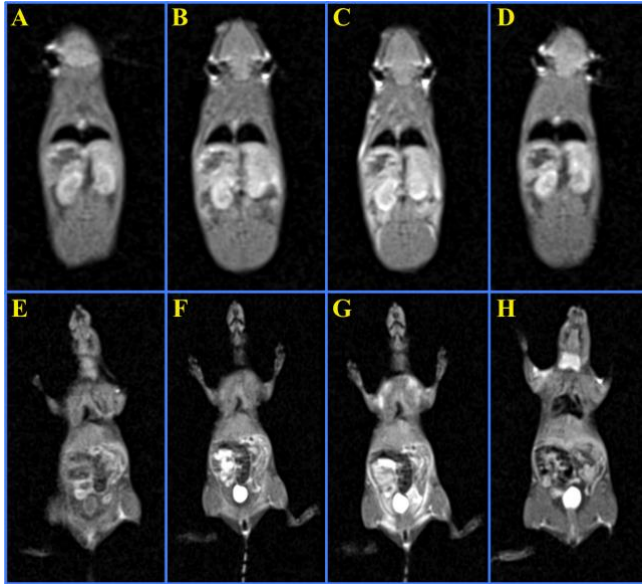


Figure III-15. Dynamic MRI study in coronal view of a mouse treated with HA NPs. The slices selected include the kidneys (upper row) and the urinary bladder (lower row). Baseline acquisition (A, E) is followed by intravenous injection of the HA NPs suspension, and the mice are scanned at 30 minutes (B, F), one hour (C, G) and 3 hours (D, H) post injection. The same window level (WL=320) and window width (WW=610) were used in all images.

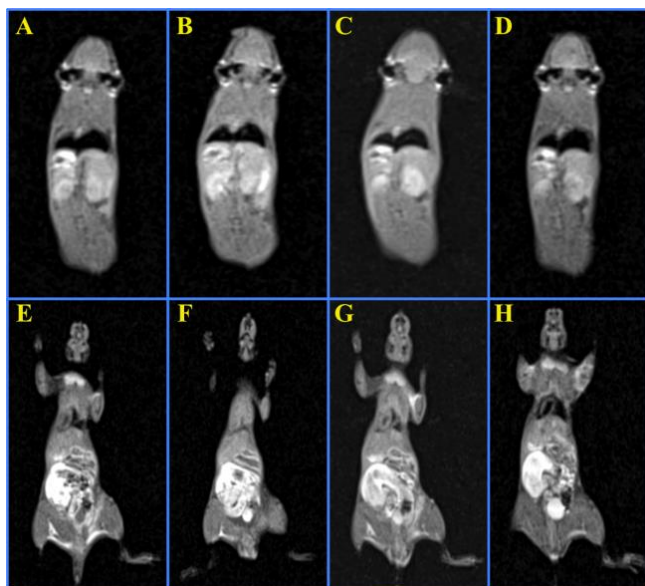


Figure III-16. Dynamic MRI study in coronal view of a mouse treated with Gd-DTPA. The slices selected include the kidneys (upper row) and the urinary bladder (lower row). Baseline acquisition (A, E) is followed by intravenous injection of the Gd-DTPA solution, and the mice are scanned at 30 minutes (B, F), one hour (C, G) and 3 hours (D, H) post injection. The same window level (WL=320) and window width (WW=610) were used in all images.

III.2.2.9 In vivo biodistribution study

We have also performed some preliminary study of biodistribution, stated as percentage of injected dose per gram of organ (% ID/g), in mice at 1 h after intravenous injection of cHANPs. These results are still work in progress even if no residuals are detected in the organs after 24 hr.

Mice are sacrificed 8 hours after the injection and the accumulation of the metal within the organs is measured by ICP–MS after homogenization and digestion as reported in the *Experimental Section*.

Evaluation of the biodistribution and clearance is currently under investigation but the weight of the organs is anyway reported as available data for further analysis. Preliminary results show no residuals of the metal in the organs (for further details see the *Appendix V.I.*). Tables below show the weights of the organs after 8 hours.

Subject	Organ	Weight (mg)
Mouse 1 (T1)	Liver	909.30
	Kidney	219.25
	Lung	141.41
	Spleen	75.75
	Heart	80.40
	Blood	≈1ml
	Brain	382.20

Subject	Organ	Weight (mg)
Mouse 2 (T2)	Liver	674.32
	Kidney	256.38
	Lung	151.14
	Spleen	100.23
	Heart	100.03
	Blood	≈1ml
	Brain	412.00

Subject	Organ	Weight (mg)
Mouse 3 (T3)	Liver	683.61
	Kidney	191.78
	Lung	133.11
	Spleen	47.65
	Heart	67.15
	Blood	≈1ml
	Brain	395.00

III.3 Another case study

III.3.1 In vitro MRI of Gd-loaded PEGylated cHANPs

Given the versatility of our platform, it is of interest to investigate how the selection of the different crosslinking reaction's strategies, or the encapsulation of different agents could result in advanced and tailorable CAs-loaded nanoparticles.

In vitro relaxivity is studied for loaded and unloaded cHANPs and the results are compared also with nanoparticles after PEGylation.

The relaxation time values of Gd-DTPA and cHANPs are first calculated at 37 °C and 1.5 T (Minispec mq60). For all MR instruments, results clearly show that the relaxation time for Gd-DTPA entrapped within cHANPs is shorter than that of the “free” contrast agent.

Also in these conditions, after PEGylation for both strategies, we have achieved a T_1 of 1590 ms which corresponds to 20 μM of Gd-loaded cHANPs suspension (measured through ICP-MS), while 100 μM of Gd-DTPA free in solution is required to achieve a comparable T_1 (Figure III-17). Indeed, the relaxation time reported for cHANPs is achieved with a concentration about 5 times lower than that of the free Gd-DTPA.

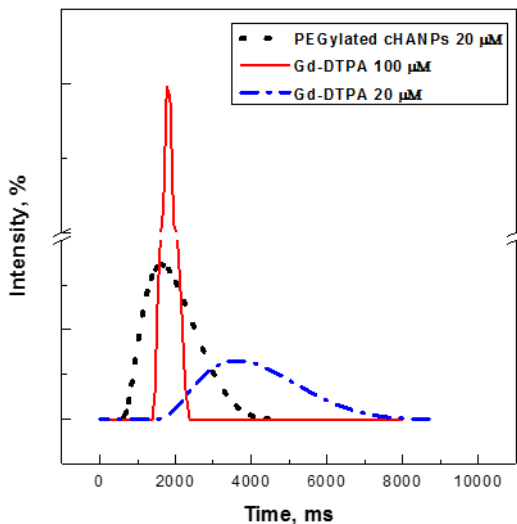


Figure III-17. In vitro relaxation time distribution. Relaxation time distribution reported for: Gd-DTPA in water solution at 20 μM and 100 μM ; PEGylated loaded cHANPs at *standard conditions* obtained using 4% v/v DVS in the side channels, at pH 12.3, reported at 20 μM of Gd-DTPA.

III.4 Conclusions

cHANPs performances have been assessed in terms of longitudinal relaxation rates as a function of the crosslinking degree and loading conditions. Additionally, a relaxation rate T_1 of 1562 ms is achieved with 10 μM of Gd-loaded cHANPs while 100 μM of Gd-DTPA solution is required to reach similar T_1 (about 1724 ms).

Results support the concept that the entrapment of the Gd-based CAs within the hydrogel structure can enhance relaxivity, thus enable potentially low dosage administration. Therefore, the positive contrast

effect is preserved, ensuring an improvement of the time window for clinical imaging acquisitions due to the reduction of long scan time and rapid renal clearance. Proposed cHANPs could improve the stability and reduce toxicity related to the Gd-chelate. Furthermore, the surface charge analysis reports the presence of carboxylic groups that are readily functionalized with targeting moieties, increasing potentially chemical functionalities to impact on tissue specificity and integrating additional imaging and therapeutic capabilities. Preliminary studies about toxicity, in vivo biodistribution and MRI acquisition highlight the powerful effect of the produced nanostructures for application in clinical imaging

III.5 References

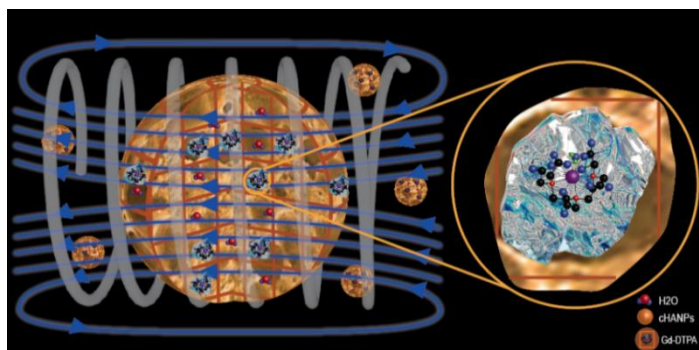
- 1 Mansfield, P. Snapshot magnetic resonance imaging (nobel lecture). *Angewandte Chemie-International Edition* **43**, 5456-5464, doi:10.1002/anie.200460078 (2004).
- 2 Caravan, P., Ellison, J. J., McMurry, T. J. & Lauffer, R. B. Gadolinium(III) chelates as MRI contrast agents: Structure, dynamics, and applications. *Chemical Reviews* **99**, 2293-2352, doi:10.1021/cr980440x (1999).
- 3 Rutt, B. K. & Lee, D. H. The impact of field strength on image quality in MRI. *Jmri-Journal of Magnetic Resonance Imaging* **6**, 57-62, doi:10.1002/jmri.1880060111 (1996).
- 4 Sethi, R. *et al.* Enhanced MRI relaxivity of Gd³⁺-based contrast agents geometrically confined within porous nanoconstructs. *Contrast Media & Molecular Imaging* **7**, 501-508, doi:10.1002/cmml.1480 (2012).
- 5 Xue, S. H., Qiao, J. J., Pu, F., Cameron, M. & Yang, J. J. Design of a novel class of protein-based magnetic resonance imaging contrast agents for the molecular imaging of cancer biomarkers. *Wiley Interdisciplinary Reviews-Nanomedicine and Nanobiotechnology* **5**, 163-179, doi:10.1002/wnan.1205 (2013).
- 6 Caravan, P. Strategies for increasing the sensitivity of gadolinium based MRI contrast agents. *Chemical Society Reviews* **35**, 512-523, doi:10.1039/b510982p (2006).
- 7 Laurent, S., Elst, L. V. & Muller, R. N. Comparative study of the physicochemical properties of six clinical low molecular weight gadolinium contrast agents. *Contrast Media & Molecular Imaging* **1**, 128-137, doi:10.1002/cmml.100 (2006).
- 8 Toth, T., Helm, L. & Merbach, A. E. Relaxivity of gadolinium(III) complexes: Theory and mechanism. *Chemistry of Contrast Agents in Medical Magnetic Resonance Imaging*, 45-119 (2001).
- 9 Penfield, J. G. & Reilly, R. F., Jr. What nephrologists need to know about gadolinium. *Nature Clinical Practice Nephrology* **3**, 654-668, doi:10.1038/ncpneph0660 (2007).
- 10 McDonald, R. J. *et al.* Intracranial Gadolinium Deposition after Contrast-enhanced MR Imaging. *Radiology* **275**, 772-782, doi:10.1148/radiol.15150025 (2015).
- 11 Cao, C.-Y., Shen, Y.-Y., Wang, J.-D., Li, L. & Liang, G.-L. Controlled intracellular self-assembly of gadolinium nanoparticles as smart molecular MR contrast agents. *Scientific Reports* **3**, doi:10.1038/srep01024 (2013).
- 12 Ahmad, M. W. *et al.* Potential dual imaging nanoparticle: Gd₂O₃ nanoparticle. *Scientific Reports* **5**, doi:10.1038/srep08549 (2015).
- 13 Moriggi, L. *et al.* Gold Nanoparticles Functionalized with Gadolinium Chelates as High-Relaxivity MRI Contrast Agents. *Journal of the American Chemical Society* **131**, 10828-+, doi:10.1021/ja904094t (2009).

- 14 Cheng, Z. L., Thorek, D. L. J. & Tsourkas, A. Gadolinium-Conjugated Dendrimer Nanoclusters as a Tumor-Targeted T-1 Magnetic Resonance Imaging Contrast Agent. *Angewandte Chemie-International Edition* **49**, 346-350, doi:10.1002/anie.200905133 (2010).
- 15 Huang, C. H., Nwe, K., Al Zaki, A., Brechbiel, M. W. & Tsourkas, A. Biodegradable Polydisulfide Dendrimer Nanoclusters as MRI Contrast Agents. *ACS Nano* **6**, 9416-9424, doi:10.1021/nn304160p (2012).
- 16 Chen, K. J. *et al.* A small MRI contrast agent library of gadolinium(III)-encapsulated supramolecular nanoparticles for improved relaxivity and sensitivity. *Biomaterials* **32**, 2160-2165, doi:10.1016/j.biomaterials.2010.11.043 (2011).
- 17 Felton, C. *et al.* Magnetic nanoparticles as contrast agents in biomedical imaging: recent advances in iron- and manganese-based magnetic nanoparticles. *Drug Metabolism Reviews* **46**, 142-154 (2014).
- 18 Kim, T. *et al.* Mesoporous Silica-Coated Hollow Manganese Oxide Nanoparticles as Positive T-1 Contrast Agents for Labeling and MRI Tracking of Adipose-Derived Mesenchymal Stem Cells. *Journal of the American Chemical Society* **133**, 2955-2961, doi:10.1021/ja1084095 (2011).
- 19 Wen, S. H. *et al.* Multifunctional dendrimer-entrapped gold nanoparticles for dual mode CT/MR imaging applications. *Biomaterials* **34**, 1570-1580, doi:10.1016/j.biomaterials.2012.11.010 (2013).
- 20 Na, H. B., Song, I. C. & Hyeon, T. Inorganic Nanoparticles for MRI Contrast Agents. *Advanced Materials* **21**, 2133-2148, doi:10.1002/adma.200802366 (2009).
- 21 Ananta, J. S. *et al.* Geometrical confinement of gadolinium-based contrast agents in nanoporous particles enhances T-1 contrast. *Nature Nanotechnology* **5**, 815-821, doi:10.1038/nnano.2010.203 (2010).
- 22 Sethi, R. *et al.* Enhanced MRI relaxivity of Gd³⁺-based contrast agents geometrically confined within porous nanoconstructs. *Contrast Media & Molecular Imaging* **7**, 501-508, doi:10.1002/cmml.1480 (2012).
- 23 Gizzatov, A. *et al.* Geometrical confinement of Gd(DOTA) molecules within mesoporous silicon nanoconstructs for MR imaging of cancer. *Cancer Letters* **352**, 97-101, doi:10.1016/j.canlet.2014.06.001 (2014).
- 24 Courant, T. *et al.* Hydrogels Incorporating GdDOTA: Towards Highly Efficient Dual T1/T2 MRI Contrast Agents. *Angewandte Chemie-International Edition* **51**, 9119-9122, doi:10.1002/anie.201203190 (2012).
- 25 Ponsiglione, A., Russo, M., Netti, P. & Torino, E. Impact of biopolymer matrices on relaxometric properties of contrast agents. *Interface Focus* **20160061**, doi:http://dx.doi.org/10.1098/rsfs.2016.0061 (2016).
- 26 Mitragotri, S. & Lahann, J. Physical approaches to biomaterial design. *Nature Materials* **8**, 15-23, doi:10.1038/nmat2344 (2009).

- 27 Zhu, Z. Q., Si, T. & Xu, R. X. Microencapsulation of indocyanine green for potential applications in image-guided drug delivery. *Lab on a Chip* **15**, 646-649, doi:10.1039/c4lc01032a (2015).
- 28 Sah, E. & Sah, H. Recent Trends in Preparation of Poly(lactide-co-glycolide) Nanoparticles by Mixing Polymeric Organic Solution with Antisolvent. *Journal of Nanomaterials*, **22**, doi:10.1155/2015/794601 (2015).
- 29 Jahn, A. *et al.* Microfluidic Mixing and the Formation of Nanoscale Lipid Vesicles. *Acs Nano* **4**, 2077-2087, doi:10.1021/nn901676x (2010).
- 30 Hood, R. R. & DeVoe, D. L. High-Throughput Continuous Flow Production of Nanoscale Liposomes by Microfluidic Vertical Flow Focusing. *Small* **11**, 5790-5799, doi:10.1002/sml.201501345 (2015).
- 31 Lu, M. *et al.* Shape-Controlled Synthesis of Hybrid Nanomaterials via Three-Dimensional Hydrodynamic Focusing. *Acs Nano* **8**, 10026-10034, doi:10.1021/nn502549v (2014).
- 32 Kang, X. *et al.* Mass production of highly monodisperse polymeric nanoparticles by parallel flow focusing system. *Microfluidics and Nanofluidics* **15**, 337-345, doi:10.1007/s10404-013-1152-6 (2013).
- 33 Rhee, M. *et al.* Synthesis of Size-Tunable Polymeric Nanoparticles Enabled by 3D Hydrodynamic Flow Focusing in Single-Layer Microchannels. *Advanced Materials* **23**, H79-H83, doi:10.1002/adma.201004333 (2011).
- 34 Xu, Q. *et al.* Preparation of Monodisperse Biodegradable Polymer Microparticles Using a Microfluidic Flow-Focusing Device for Controlled Drug Delivery. *Small* **5**, 1575-1581, doi:10.1002/sml.200801855 (2009).
- 35 DeMello, J. & DeMello, A. Microscale reactors: nanoscale products. *Lab on a Chip* **4**, 11N-15N, doi:10.1039/b403638g (2004).
- 36 Min, K. I., Im, D. J., Lee, H. J. & Kim, D. P. Three-dimensional flash flow microreactor for scale-up production of monodisperse PEG-PLGA nanoparticles. *Lab on a Chip* **14**, 3987-3992, doi:10.1039/c4lc00700j (2014).
- 37 Carugo, D., Bottaro, E., Owen, J., Stride, E. & Nastruzzi, C. Liposome production by microfluidics: potential and limiting factors. *Scientific Reports* **6**, doi:10.1038/srep25876 (2016).
- 38 Schubert, S., Delaney, J. T., Jr. & Schubert, U. S. Nanoprecipitation and nanoformulation of polymers: from history to powerful possibilities beyond poly(lactic acid). *Soft Matter* **7**, 1581-1588, doi:10.1039/c0sm00862a (2011).
- 39 Mora-Huertas, C. E., Fessi, H. & Elaissari, A. Polymer-based nanocapsules for drug delivery. *International Journal of Pharmaceutics* **385**, 113-142, doi:10.1016/j.ijpharm.2009.10.018 (2010).
- 40 Knopp, E. A. & Cowper, S. E. Nephrogenic systemic fibrosis: Early recognition and treatment. *Seminars in Dialysis* **21**, 123-128, doi:10.1111/j.1525-139X.2007.00399.x (2008).
- 41 Lim, J. M. *et al.* Parallel microfluidic synthesis of size-tunable polymeric nanoparticles using 3D flow focusing towards in vivo study. *Nanomedicine-*

- Nanotechnology Biology and Medicine* **10**, 401-409, doi:10.1016/j.nano.2013.08.003 (2014).
- 42 Lim, J.-M. *et al.* Ultra-High Throughput Synthesis of Nanoparticles with Homogeneous Size Distribution Using a Coaxial Turbulent Jet Mixer. *ACS Nano* **8**, 6056-6065, doi:10.1021/nn501371n (2014).
- 43 Lazarus, L. L., Yang, A. S. J., Chu, S., Brutchey, R. L. & Malmstadt, N. Flow-focused synthesis of monodisperse gold nanoparticles using ionic liquids on a microfluidic platform. *Lab on a Chip* **10**, 3377-3379, doi:10.1039/c0lc00297f (2010).
- 44 Conde, A. J. *et al.* Continuous flow generation of magnetoliposomes in a low-cost portable microfluidic platform. *Lab on a Chip* **14**, 4506-4512, doi:10.1039/c4lc00839a (2014).
- 45 Herranz-Blanco, B. *et al.* Microfluidic assembly of multistage porous silicon-lipid vesicles for controlled drug release. *Lab on a Chip* **14**, 1083-1086, doi:10.1039/c3lc51260f (2014).
- 46 Karnik, R. *et al.* Microfluidic platform for controlled synthesis of polymeric nanoparticles. *Nano Letters* **8**, 2906-2912, doi:10.1021/nl801736q (2008).
- 47 Provencher, S. W. CONTIN: a general purpose constrained regularization program for inverting noisy linear algebraic and integral equations. *Computer Physics Communications* **27**, 229-242 (1982).
- 48 Corbin, I. R. *et al.* Low-density lipoprotein nanoparticles as magnetic resonance imaging contrast agents. *Neoplasia* **8**, 488-498, doi:10.1593/neo.05835 (2006).
- 49 Kozłowski, H., Brown, D. R. & Valensin, G. Metallochemistry of Neurodegeneration: Biological, Chemical and Genetic Aspects. *Metallochemistry of Neurodegeneration: Biological, Chemical and Genetic Aspects*, 1-281, doi:10.1039/9781847555311 (2006).

IV. CHAPTER IV - Impact of biopolymer matrices on relaxometric properties of Contrast Agents: the definition of Hydrodenticity



Abstract

Properties of water molecules at the interface between MRI CAs and macromolecules could have a valuable impact on the CAs' relaxivity by modifying the correlation times of the metal chelate. However, an understanding of the physicochemical properties of polymer/CA systems is necessary to improve the efficiency of clinically used CAs. In this context, we investigate the impact of Hyaluronic Acid (HA) hydrogels on the relaxometric properties of Gd-DTPA and we observe that the presence of Gd-DTPA could alter the polymer conformation and the behaviour of water molecules at the HA/Gd-DTPA interface, thus modulating the relaxivity of the system. The tunability of hydrogel structures could be exploited to improve magnetic properties of metal chelates. Thus, hydrogel structural parameters of cHANPs are investigated to control the status of hydrated Gd-DTPA subjected to the osmotic pressure deriving from elastodynamics of swollen gels, establishing an equilibrium able to boost relaxometric properties of the Gd-DTPA without the chemical modification of the chelate. This capability has been here called *Hydrodenticity* and defined in terms of crosslink density and mesh size, tunable through our microfluidic approach.

IV.1 Background

IV.1.1 Introduction

Investigation of water molecules at the interface between relevant clinical Contrast Agents (CAs) for Magnetic Resonance Imaging (MRI) and macromolecules can be of great interest to increase the performances of metal chelates. Indeed, most of the clinically-used CAs are characterized by poor effectiveness in the high magnetic fields region, which is clinically favored because of its higher signal-to-noise ratio and high-resolution imaging. MRI CAs also lack of tissue specificity and can cause heavy allergic effects, serious nephrotoxicity¹⁻³ and intracranial deposition of metal ion after repeated intravenous administration⁴. Despite their wide use, currently available CAs exhibit low relaxivity⁵, which is far below its theoretical maximum required to obtain an accurate diagnosis at safe administration dosage⁶. In these perspectives, the possibility to have a CA that could work at low concentration but without giving over its signal intensity and, therefore, positive contrast effect is of great interest, as already said in Chapter 3. The extensive research on nano-engineered systems and polymer-based nanocomposites⁷⁻¹⁷ has led to significant advances also in the field of MRI^{13,18-22}. In particular, some recent studies have shown that nanoconstructs can improve CAs' relaxivity and many efforts have been devoted to the development of polymer-based carriers for MRI CAs with particular reference to Gadolinium (Gd) chelates, which are the most commonly clinically

used agents^{18,23-28}. In this framework, Port et al.²⁹ have reported that the rigidification of MRI CAs, obtained through covalent or non-covalent binding to macromolecules, could be favourable to an increase in relaxivity of the metal-chelate. Later, Decuzzi et al.^{5,30} have proved that it is possible to modify through the geometrical confinement the magnetic properties of MRI CAs by controlling their characteristic correlation times without the chemical modification of the chelate structure. Furthermore, Courant et al.²⁵ have highlighted the capability of combined hydrogels to boost the relaxivity of Gd-based CAs. In details, hydrogels³¹⁻³⁴ show these three-dimensional networks, made of hydrophilic polymer chains held together by chemical or physical crosslinking, they are glassy in the dry state but have the ability to swell in water, forming elastic gels that retain a large quantity of fluid in their mesh-like structures³⁵. The presence of hydrophilic polymer interfaces and the control of water behaviour in hydrogels play a fundamental role in the relaxation enhancement of the Gd-based CAs by influencing the characteristic correlation times defined by the theory of Solomon and Bloembergen³⁶. As stated by this theory,^{37,38} indeed, high relaxivity can be achieved by a fine and accurate control of the characteristic parameters that regulate the dipolar interaction between water protons and Gd-based CAs.³⁹ the number of water molecules (q) in the Inner Sphere (IS), i.e. those present in the coordination sites of the Gd ion, and their residence lifetime (τ_M); the rotational correlation time of the metal complex (τ_R);

the diffusion correlation time (τ_D) of the water molecules in the Outer Sphere (OS), i.e. those diffusing nearby the metal complex. According to these parameters and by exploiting the versatile properties of nano- and bio-materials, several nanostructured CAs with enhanced relaxivity have been investigated.⁴⁰⁻⁴⁵

Despite several experimental studies addressed in this field, a comprehensive knowledge of the mechanisms involved in the relaxation enhancement due to the entrapment of CAs in polymer-based architectures is still missing. In particular, the role played by the water at the interface between polymer chains and MRI CAs has not been fully investigated and could lead to the availability of tailored models that accurately describe these novel complex systems. In this perspective, we believe that a more in-depth knowledge about the interference between macromolecules and MRI CAs and an understanding of their physicochemical properties is necessary to impact in the design strategies of the nanostructures and, consequently, to overcome the limitations of clinically used MRI CAs, particularly linked to the low relaxivity. To this aim, it is crucial to study the main phenomena involved in the formation of polymer matrices and how their properties can influence the relaxivity of MRI CAs is performed.

IV.1.2 Aim of Chapter 4

In the Chapter 4, we aim to investigate the impact of hydrogel-CA systems on the relaxometric properties of metal chelates to understand

better the clear role of the water, which mediates interactions and could be responsible for their behaviour in solution. On one hand, the magnetic properties of the water protons surrounding the CA are fundamental to enhance the CAs' relaxivity. On the other, the presence of water molecules can induce changes in the polymer structure through polar interactions, hydrogen bonding and osmotic pressure. Among different biopolymer, Hyaluronic Acid (HA)⁴⁶ is chosen as model polymer due to its hydrophilic nature and established biocompatibility and biodegradability. Commercially available Gd-DTPA is selected as the CA due to its widespread use in clinical practice⁴⁷.

First experiments are focused on determining the water self-diffusion coefficients in polymer and CA solutions through Time-Domain NMR relaxometry to observe changes in water mobility in the presence of both HA and Gd-DTPA. Self-diffusion measurements have already proved especially successful for probing interfacial water structure and dynamics near various biological and polymer surfaces⁴⁸. Intramolecular interactions, as well as entropy costs, can alter the mobility of solvent molecules within polymer matrices or in confined environments, with a slowing effect on the diffusion⁴⁹⁻⁵¹. Moreover, since the relaxation efficiency is mediated by translational and rotational diffusion⁴⁸, a variation of the water diffusion behaviour at the interface between polymer chains and MRI CAs could impact on the τ_D of the complex, thereby influencing the relaxometric properties

of the metal chelate. Isothermal Titration Calorimetry (ITC) is employed after that to investigate thermodynamic interactions involved in the mixing of HA with Gd-DTPA⁵²⁻⁵⁴. Finally, relaxometric properties of HA/Gd-DTPA solutions are investigated by means of time-domain NMR relaxometry⁵⁵. The knowledge of these complex systems could be scaled to nanoscale dimensions, inspiring the development of a new class of nanostructured MRI CAs with highly tunable relaxometric properties. Starting from these observations, we have also proved that, by changing structural parameters of a hydrogel matrix containing a CA, through our already presented Microfluidic Flow Focusing approach, it is possible to affect the dipolar coupling between the electronic magnetic moment of the metal ion and the nuclear magnetic moment of the water nuclei (relaxation rate). This effect results from the complex equilibrium established by the elastic stretches of polymer chains, water osmotic pressure and hydration degree of Gd-based CAs, that we have called *Hydrodenticity*.

Hydrodenticity, hence, refers to the status of the hydrated Gd-DTPA with the coordination water subjected to osmotic pressure^{56,57} deriving from elastodynamics equilibrium of swollen gels.⁵⁸⁻⁶¹ We hypothesize that the attainment of this equilibrium is reached when the normal energetic stability of the meshes is compromised by the presence of the Gd-DTPA and evolves to a new spontaneous equilibrium involving the formation of nanocompartments, called “Gado-

Meshes”, in which water is in an abnormal aggregate state that influences the relaxivity. The capability to control the organization of these nanocompartments within the nanoparticles can be applied to define a new class of medical devices useful to improve the properties of CAs for MRI. Within the cHANPs, the properties of *Hydrodentivity* can be modulated to obtain desired crosslink density, mesh size, hydrophilicity and loading capability, playing on the biodegradable behavior and relaxometric properties of the Gd-loaded cHANPs.

IV.2 Case Study

IV.2.1 Experimental Section

IV.2.1.1 Materials

HA (Bohus Biotech, Sweden) with an average molecular weight of 42000 Da is used for the polymer matrix because of its biocompatibility, biodegradability and swelling properties. Commercially available Gd-DTPA (Sigma-Aldrich) with a molecular weight of 547.57 Da is used since it is a well-known, low-risk CA. Divinyl Sulfone (DVS) (Sigma Aldrich) with a molecular weight of 118.15 Da is used as crosslinking agent. Milli-Q water is systematically used for sample preparation and analysis.

IV.2.1.2 Sample preparation

Non-crosslinked hydrogel-CA solutions were prepared by dispersing both the HA and the Gd-DTPA powders in distilled deionized water and then mixing using magnetic stirrer. Different HA concentrations,

ranging from 0.1 to 5 % w/v, was utilized for the experimentation. For each fixed concentration of HA, Gd-DTPA concentration was varied between 0 and 0.2 mM.

Crosslinked hydrogel-CA solutions were prepared by adding DVS to the above-described solutions to crosslink the polymer network chemically. Hydrogels were prepared at different HA: DVS ratios (from 1:1 to 1:16).

IV.2.1.3 Water self-diffusion coefficient

Diffusion measurements of water molecules were carried out on a Bruker Minispec (mq 20) bench-top relaxometer operating at 20 MHz for protons (magnetic field strength: 0.47 T). A pulsed field gradient spin echo (PFG-SE) sequence⁶², with two magnetic field gradient pulses of length δ and strength g , and with a delay Δ between the leading edges of them, was used to measure water self-diffusion coefficients. The self-diffusion coefficient, D , was derived by linear regression of signal attenuation ratio curve, a semi-logarithmic plot of the echo attenuation as a function of the tunable parameter of the sequence, $k = (\gamma g \delta)^2 * (\Delta - \delta/3)$.

IV.2.1.4 Isothermal Titration Calorimetry

Isothermal Titration Calorimetry (ITC) measurements were conducted by filling the sample cell (0.7 mL in volume) with an aqueous solution of HA at different concentrations (from 0.1 to 0.7 % w/v) and the 50 μ L syringe with an aqueous solution of Gd-DTPA at 1.5 mM. Measurements were performed at 25 °C and fixed stirring rate of 200

rpm. Fifty injections, each of 1 μL of Gd-DTPA, were delivered in intervals of 500 s. Data analysis and processing to provide ITC and enthalpy change, ΔH , profiles were carried out using the NanoAnalyze (TA instruments) and the Origin Pro 9.1 SRO software (OriginLab Corporation, USA).

IV.2.1.5 Relaxometric measurement

Relaxation times were measured on a Bruker Minispec (mq 60) bench-top relaxometer operating at 60 MHz for protons (magnetic field strength: 1.41 T). The acquisitions were performed at 37°C, and before each measurement, the sample was placed into the NMR probe for about 15 min for thermal equilibration. Longitudinal relaxation times, T_1 , were determined by both saturation (SR) and inversion recovery (IR) pulse sequences, by using the same protocol presented into the paragraph III.2.1.4. Data were treated by a least-squares method using Origin Pro 9.1 SRO software (OriginLab Corporation, USA).

IV.2.1.6 Swelling Ratio and Hydrogel parameters

Swelling Ratio (SR) is calculated as follows:

$$SR = d_{H_2O}/d_{eth}$$

where d_{eth} (in nm) d_{H_2O} (in nm) are the nanoparticle's diameters in Ethanol and in water respectively, measured by Dynamic Light Scattering. A simplified version of the the Flory-Rehner equations are used in order to compute the hydrogel structure parameters ($\overline{M_c}$: molecular weight between crosslinks (g/mol); ν_e : effective crosslink

density (mol/cm³); ξ : mesh size (nm). See the *Appendix V.II* for the detailed calculations.

IV.2.2 Results and Discussion

IV.2.2.1 Diffusion Coefficient

In our systems, we have observed that water mobility slightly changes with increasing network density induced by crosslinking reaction (Figure IV-1). Besides, a more significant decrease in the water diffusion is observed in the presence of increasing polymer concentration rather than increasing CA concentration (Table IV-1). However, the study of the diffusion coefficient as a function of the crosslinking degree requires further investigation to understand its influence on the relaxometric properties.

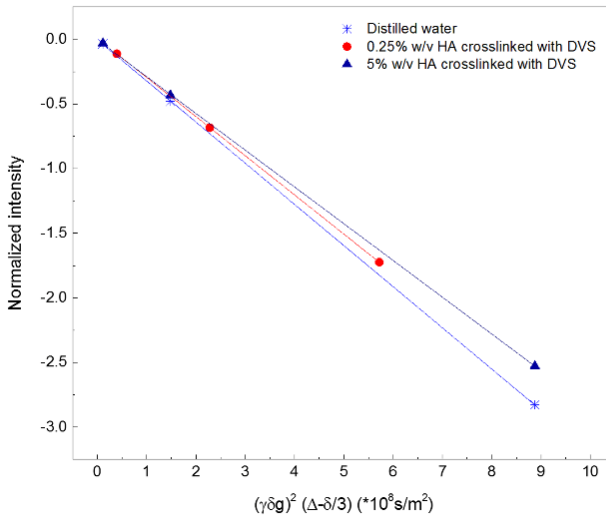


Figure IV-1. Stejskal Tanner Plot is used for calculating water self-diffusion coefficient of: (1) distilled water; (2) 0.25 % w/v HA solution with 5 μL DVS 8 hours after the crosslinking reaction; (3) 5 % w/v HA solution with 40 μL DVS 8 hours after the crosslinking reaction.

Table IV-1. Range of water self-diffusion coefficients, D , measured for: (1) distilled water; (2) Gd-DTPA solutions at different Gd-DTPA concentrations; (3) 0.25 and 5 % w/v HA hydrogel solutions at varying crosslinking degrees, i.e. different DVS concentrations.

HA (% w/v)	DVS (μL)	Gd-DTPA (mM)	D^a ($*10^{-9} \text{ m}^2\text{s}^{-1}$)
0	0	0	3.19
0	0	0.05 \div 1	3.18 \div 3.09
0.25	0 \div 25	0	3.05 \div 2.90
5	5 \div 40	0	2.88 \div 2.83

^a Values of the standard deviation for the measured diffusion coefficients are all below $0.4*10^{-12} \text{ m}^2\text{s}^{-1}$.

Further details on diffusion data are reported in Table IV-2 and Table IV-3.

Table IV-2. Water self-diffusion coefficient measured at different Pulse Gradient Amplitudes for 0.25 and 5 % w/v HA hydrogel solution at varying crosslinking degrees (different DVS concentrations). Diffusion coefficients have been measured 8 and 24 hours after crosslinking reaction.

HA (% w/v)	DVS (μL)	D after 8h (*10 ⁻⁹ m ² s ⁻¹)	D after 24h (*10 ⁻⁹ m ² s ⁻¹)
0	0	3.19 ± 0.01	3.19 ± 0.01
0.25	0	3.05 ± 0.01	3.06 ± 0.02
0.25	5	3.01 ± 0.02	3.02 ± 0.01
0.25	10	2.97 ± 0.03	2.98 ± 0.02
0.25	15	2.95 ± 0.03	2.96 ± 0.02
0.25	20	2.92 ± 0.02	2.94 ± 0.02
0.25	25	2.90 ± 0.02	2.92 ± 0.03
5	10	2.88 ± 0.02	2.87 ± 0.01
5	20	2.85 ± 0.01	2.85 ± 0.02
5	30	2.83 ± 0.02	2.85 ± 0.01
5	40	2.84 ± 0.01	2.84 ± 0.02

Table IV-3. Range of water self-diffusion coefficient measured for Gd-DTPA solutions at different Gd-DTPA concentrations.

Gd-DTPA (μM)	D (* $10^{-9} \text{ m}^2\text{s}^{-1}$)
0	3.19 ± 0.01
50	3.12 ± 0.02
100	3.14 ± 0.02
150	3.09 ± 0.02
200	3.18 ± 0.01
500	3.11 ± 0.02
1000	3.13 ± 0.03

Furthermore, results show that water mobility starts decreasing even at very low polymer concentration (0.25 % w/v HA). This dynamic can be attributed to the high molecular weight and hydrophilicity of the HA, which allows the formation of several hydrogen bonds at the surface of the polymer, thereby stabilizing the polymer structure and reducing water self-diffusion. At first, because of the diffusion measurements, we can observe that thanks to the high hydrophilicity of the HA promoting the hydrogen bonds formation at the surface of the polymer, water mobility starts decreasing even at very low polymer concentrations.

IV.2.2.2 Isothermal Titration Calorimetry

Here, ITC is proposed to calculate the energetic contribution and thermodynamic interactions deriving from the mixing of Gd-chelates with the polymer solution.

In our experiment, a simple dilution of Gd-DTPA in water or water in HA exhibits only small constant exothermic peaks (Figure IV-2 and Figure IV-3).

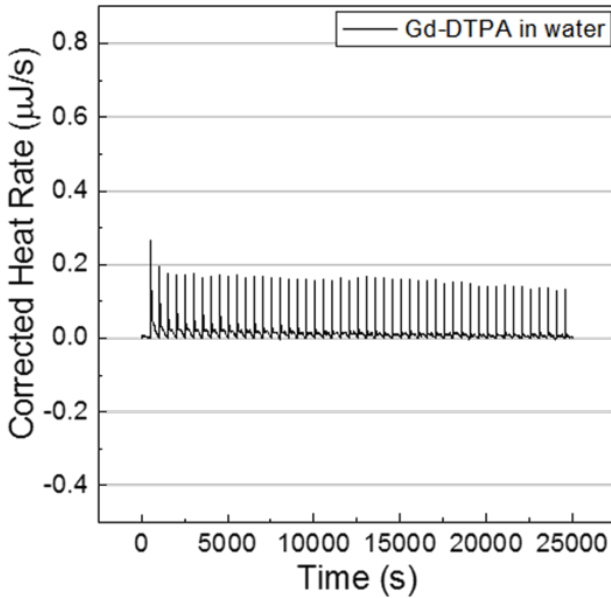


Figure IV-2. Titration curves of Gd-DTPA in water at 25 °C and 200 rpm.

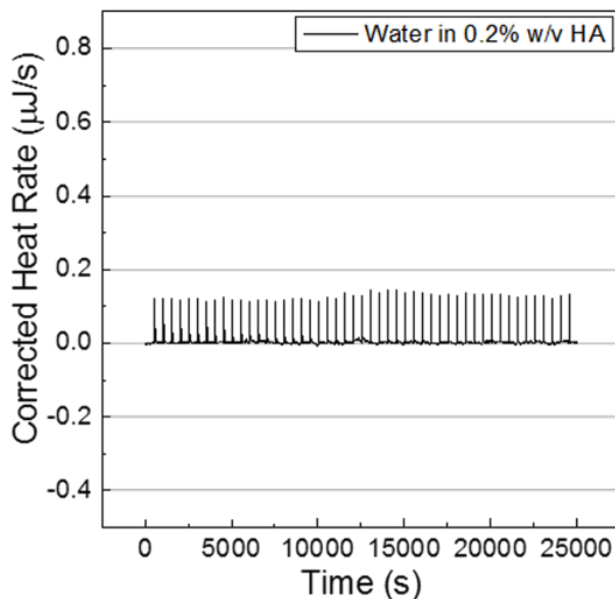


Figure IV-3. Titration curves of water into 0.2% w/v HA solutions at 25 °C and 200 rpm.

On the contrary, when Gd-DTPA is injected as titrant into the cell containing HA solution a change from exothermic to endothermic behaviour is clearly observed. This change occurs at an HA/Gd-DTPA molar ratio of 0.5 (Figure IV-4), i.e. when the molar concentration of Gd-DTPA in solution is twice the HA molar concentration. Starting from these observations, we hypothesize that at a certain HA/Gd-DTPA ratio, the enthalpy variations obtained in the binding experiment can be related to changes in the polymer structure, which in turn can be associated with the water-mediated interaction between the Gd-chelate and the polymer. The presence of Gd-DTPA, which

has a high affinity for water molecules, may interfere with the polymer solution and induce peculiar arrangements in polymer chains' conformation.

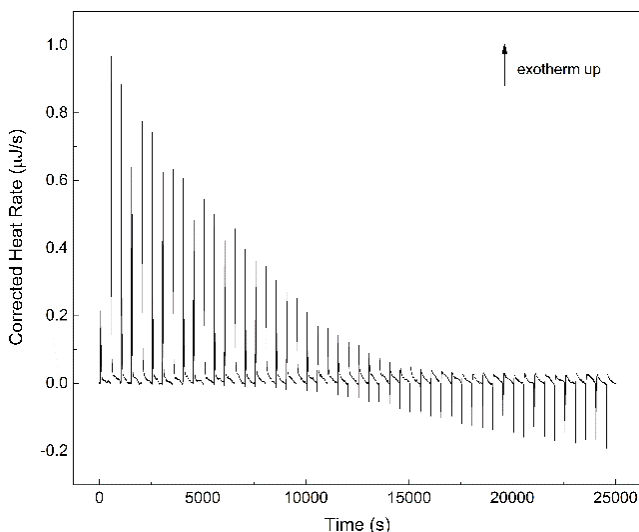
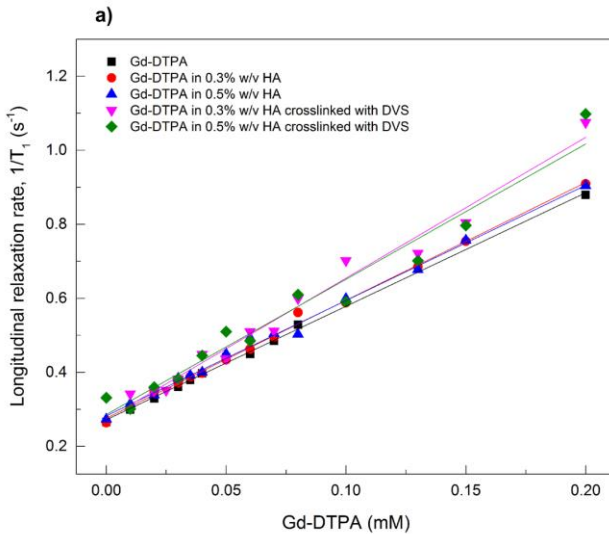


Figure IV-4. Thermograms (heat flow versus time) of Gd-DTPA into aqueous solution of HA at 0.6 % w/v. Temperature and stirring rate have been kept constant at 25 °C and 200 rpm, respectively, for each sample.

These experimental observations could be of crucial importance in the design of polymer-based MRI CAs. Therefore, we have subsequently investigated how the polymer conformation can influence the relaxometric properties of the MRI complex in the polymer solution. Secondly, ITC results suggest that the presence of Gd-DTPA induce considerable thermodynamic variations in the polymer/CA mixing process that can be related to changes in polymer conformation.

IV.2.2.3 Time-Domain Relaxometry

Through Time-Domain Relaxometry, relationships between system formulation, polymer matrices and relaxivity enhancement are provided. Results show how the relaxivity could be varied by changing the structural parameters of the hydrogel, namely polymer concentration and crosslinking degree (DVS concentration). Figure IV-5 a) and b) display the longitudinal relaxation rate, R_1 , and longitudinal relaxation time distribution for Gd-DTPA in distilled water and different crosslinked and non-crosslinked HA/Gd-DTPA solutions.



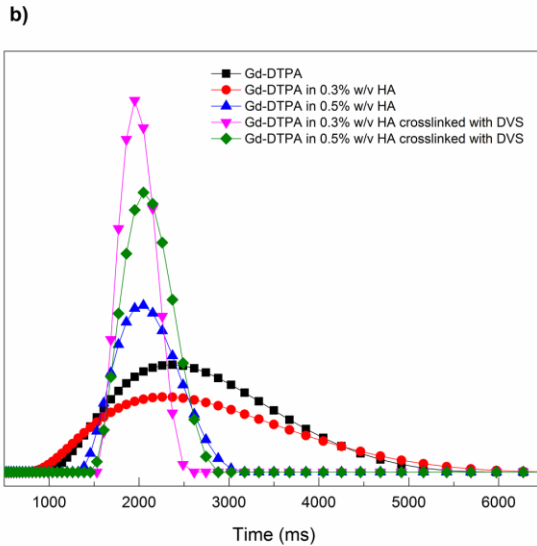


Figure IV-5. a) Longitudinal relaxation rate as a function of Gd-DTPA concentration and **b)** longitudinal relaxation time distribution for: (1) Gd-DTPA in distilled water; (2) Gd-DTPA in 0.3 % w/v HA solution; (3) Gd-DTPA in 0.5 % w/v HA solution; (4) Gd-DTPA in 0.3 % w/v HA crosslinked with DVS (HA: DVS = 1:8); (5) Gd-DTPA in 0.5 % w/v HA crosslinked with DVS (HA:DVS = 1:8). Linear regression is applied to each set of data reported in **a)**.

In detail, Figure IV-5 a) demonstrates the variation of relaxation rates against the concentration of Gd-DTPA. As expected, R_1 rises linearly as Gd-DTPA concentration increases and surprisingly, the relaxivity, r_1 , appears to be tuned mostly by the variation of hydrogel structure (polymer concentration and crosslinking degree). Therefore, we found out that could be possible to modulate the r_1 by changing the DVS concentration and to induce corresponding changes in the relaxation rates through the hydrogel matrix. Slopes of the regression lines in

Figure IV-5 a), indicating each obtained relaxivity r_1 value, are reported in Table IV-4. Figure IV-5 b) highlights through the relaxation time distribution the influence of hydrogel structure on the relaxation times as already discussed in Figure IV-5 a). In particular, it displays a narrower relaxation time distribution in the presence of crosslinking, thereby indicating an enhancement of the MRI signal. As shown in Table IV-4, a slight increase in the relaxivity (from 1% to 6%) on the reference solution (Gd-DTPA in water) is observed for the non-crosslinked samples. Besides, for crosslinked hydrogel-CA systems, in the presence of a crosslinked network, the relaxivity increases to an even greater extent, ranging from 11% up to 25%. About this last result, it seems that the crosslinking degree is interfering more on the relaxivity of CAs than on the diffusivity of water, acting, therefore, more on the rigidification of the CAs than on the water mobility.

Table IV-4. Relaxivity enhancement for the investigated polymer/CA systems.

HA (% w/v)	DVS (% w/v)	r_1 (mM ⁻¹ s ⁻¹)	r_1 increment (%)
0	0	3.07 ± 0.04	0
0.3	0	3.18 ± 0.05	3.6
0.3	2.4	3,81 ± 0.16	24,1
0.5	0	3,11 ± 0.06	1.3
0.5	4	3,65 ± 0.23	18,9
0.7	0	3,26 ± 0.06	6.2
0.7	5.6	3,41 ± 0.21	11.1

However, this aspect is of crucial important and will require further investigations and comparison. Percentages of increment in the relaxivity are calculated by dividing the difference between the relaxivity of the polymer/CA system and the reference (Gd-DTPA in water) by that of the reference solution, as follows:

$$r_1 \text{ increment} = \frac{\frac{1}{T_1} \Big|_{GdDTPA \text{ in HA}} - \frac{1}{T_1} \Big|_{GdDTPA}}{\frac{1}{T_1} \Big|_{GdDTPA}} * 100$$

Finally, taking into consideration the computed relaxivity values, we can hypothesize that the hydrogel structure, which is strictly dependent on the water content and its dynamics within the polymer matrix, can significantly impact on the relaxivity of the whole polymer/CA system. Table IV-5 shows further details on relaxometric data.

Table IV-5. Relaxation rates ($1/T_1$) and relaxivity values for: (Sample 1) Gd-DTPA in water; (Sample 2) Gd-DTPA in 0.3% w/v HA solution; (Sample 3) Gd-DTPA in 0.3% w/v HA solution crosslinked with 2.4% w/v DVS; (Sample 4) Gd-DTPA in 0.5% w/v HA solution; (Sample 5) Gd-DTPA in 0.5% w/v HA solution crosslinked with 4% w/v DVS; (Sample 6) Gd-DTPA in 0.7% w/v HA solution; (Sample 7) Gd-DTPA in 0.7% w/v HA solution crosslinked with 5.6% w/v DVS

Gd-DTPA (mM)	Sample 1 (s ⁻¹)	Sample 2 (s ⁻¹)	Sample 3 (s ⁻¹)	Sample 4 (s ⁻¹)	Sample 5 (s ⁻¹)	Sample 6 (s ⁻¹)	Sample 7 (s ⁻¹)
0.000	0.265 ± 0.003	0.264 ± 0.001	0.273 ± 0.000	0.273 ± 0.001	0.331 ± 0.001	0.265 ± 0.003	0.301 ± 0.001
0.010	0.299 ± 0.000	0.309 ± 0.000	0.342 ± 0.001	0.315 ± 0.001	0.301 ± 0.001	0.309 ± 0.001	0.313 ± 0.001
0.020	0.330 ± 0.001	0.347 ± 0.001	0.348 ± 0.001	0.339 ± 0.001	0.360 ± 0.001	0.345 ± 0.000	0.342 ± 0.001
0.025	-	-	0.351 ± 0.001	-	-	-	-
0.030	0.361 ± 0.000	0.372 ± 0.001	0.381 ± 0.001	0.384 ± 0.001	0.382 ± 0.001	0.373 ± 0.001	0.403 ± 0.007
0.035	0.379 ± 0.001	0.388 ± 0.001	-	0.392 ± 0.001	-	-	-
0.040	0.397 ± 0.002	0.398 ± 0.002	0.449 ± 0.001	0.400 ± 0.005	0.445 ± 0.001	0.398 ± 0.003	0.402 ± 0.006
0.050	0.441 ± 0.003	0.434 ± 0.025	0.436 ± 0.001	0.450 ± 0.001	0.510 ± 0.002	0.445 ± 0.001	0.468 ± 0.001
0.060	0.450 ± 0.001	0.463 ± 0.001	0.510 ± 0.001	0.493 ± 0.001	0.485 ± 0.001	0.452 ± 0.001	0.549 ± 0.003
0.070	0.485 ± 0.001	0.496 ± 0.001	0.512 ± 0.001	0.505 ± 0.001	-	-	-
0.080	0.528 ± 0.001	0.562 ± 0.003	0.599 ± 0.004	0.503 ± 0.001	0.610 ± 0.015	0.548 ± 0.002	0.547 ± 0.001
0.100	-	0.588 ± 0.069	0.702 ± 0.002	0.599 ± 0.004	0.590 ± 0.001	0.594 ± 0.002	0.595 ± 0.007
0.130	-	0.685 ± 0.000	0.722 ± 0.002	0.678 ± 0.001	0.701 ± 0.001	0.675 ± 0.002	0.699 ± 0.001
0.150	-	0.754 ± 0.001	0.805 ± 0.002	0.757 ± 0.002	0.797 ± 0.001	0.755 ± 0.001	0.786 ± 0.002
0.180	-	-	-	-	-	0.845 ± 0.002	1.043 ± 0.003
0.200	0.880 ± 0.002	0.909 ± 0.003	1.075 ± 0.002	0.904 ± 0.008	1.098 ± 0.004	0.971 ± 0.002	0.896 ± 0.004
0.250	-	-	-	-	-	1.071 ± 0.003	1.126 ± 0.004

Relaxivity (mM⁻¹s⁻¹)	3.067 ± 0.044	3.185 ± 0.050	3.805 ± 0.164	3.114 ± 0.061	3.655 ± 0.225	3.256 ± 0.064	3.410 ± 0.205
---	------------------	------------------	------------------	------------------	------------------	------------------	------------------

IV.2.2.4 Theoretical interpretation of the enhanced Relaxivity

Starting from the Solomon–Bloembergen–Morgan (SBM) theory³⁶, the physics of CAs is described by a set of physicochemical parameters characterizing the fluctuating magnetic dipole created by the paramagnetic ion. In detail, according to the SBM model, the metal complex can be viewed as having separate coordination spheres⁶³: the Inner Sphere (IS), which consists of water molecules directly coordinated to the metal ion, and the Outer Sphere (OS), which is a less organized structure consisting of bulk water molecules diffusing in the near environment of the metal complex. In some cases, a Second Sphere (SS) contribution is taken into account, which is related to water molecules hydrogen bonded to the metal complex⁶⁴. Each of the coordination mentioned above spheres has its characteristic parameters. IS parameters include the number of labile water molecules coordinated to the metal ion (q), the residence time of the coordinated water molecule (τ_M), which in turn determines the rate of the coordinated water molecule exchanging with the bulk, and the rotational correlation time (τ_R), which is how quickly the contrast agent is tumbling in solution. Conversely, OS parameters include the translational diffusional time (τ_D), which represent the diffusion of water molecules in the bulk near to the Gd complex.

It is already known that molecular motion, size, rigidity and possible binding between Gd-chelates and other macromolecules may induce changes in relaxivity². Furthermore, polymer architecture and properties can strongly affect the MRI enhancement^{20,26,29}.

As previously reported in the SBM theory, characteristic parameters of the metal chelate can be physically or chemically tuned and are of primary importance in the design of new CAs⁶⁵. In particular, the Gd-chelator determines the number of coordinated water molecules (q) and the water exchange rate (k_{ex}), which is the inverse of the residence time τ_M . Moreover, decreased τ_D and τ_R , which can be obtained, for instance, through the binding of the metal chelate with large macromolecules, generally yield increased relaxation rates at low magnetic fields (<1.5 T)³.

Our findings report that the presence of a polymer network can significantly affect the relaxation enhancement since it influences the hydration mechanism of the CA, i.e. the number of water molecules in either the IS, SS or OS, their diffusion behaviour and exchange rate with the water molecule coordinated to the metal ion.

As schematically represented in Figure IV-6, the obtained results suggest that changes in polymer conformation, induced by varying polymer/CA molar ratio, could be furtherly exploited to improve the relaxivity of the CA.

Indeed, the altered behaviour of the water molecules at the HA/Gd-DTPA interface, exhibiting reduced mobility and strong interactions

with the highly hydrophilic polymer surface, may have a considerable impact on the correlation times, especially τ_M and τ_D . In fact, the presence of polymer hydrophilic groups can change the access of bulk water molecules to the coordinated water molecule and, thus, alter the water exchange rate ($k_{ex} = 1/\tau_M$). Moreover, polymer chains can slightly reduce the mobility of the OS water molecules, with a consequent decreasing of τ_D . A simultaneous reduction of the CA's tumbling rate (τ_R) can also be hypothesized since the environment provided by the presence of the polymer chains as well as of the crosslinking degree may induce a slower rotation of the metal chelate.

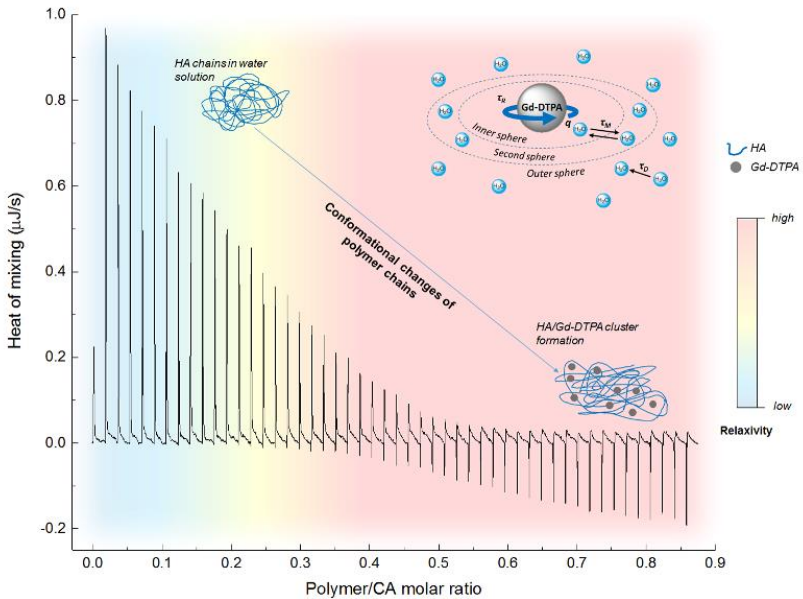


Figure IV-6. Relaxation enhancement induced by water-mediated HA/Gd-DTPA interactions.

Here, a study of the interactions involved in polymer- hydrogel-based CA solutions has been presented, aiming at understanding the key role of the water as a mediating agent that acts at the interface between the polymer and the metal chelate and determines both the polymer conformation and the relaxation enhancement. The systems have been investigated by mixing crosslinked or non-crosslinked HA with Gd-DTPA at specific polymer/CA molar ratios in aqueous solution without introducing chemical modifications of the CA. Water self-diffusion coefficients, as well as proton longitudinal relaxation curves for different HA/Gd-DTPA solutions, have been measured. A thermodynamic investigation of the mixing process between HA and Gd-DTPA in water has also been conducted. We have observed that, in the presence of a crosslinked matrix, it is possible to modulate the water content of the system and, therefore, the hydration of the CA, by adjusting the crosslinking degree of the hydrogel structure. In these conditions, a more stable polymer network can be obtained, promoting more efficient water-polymer and water-CA interactions that boost the relaxivity to higher values. The crosslinking degree is proposed as an advanced tool to modulate the hydrogel network and its properties, enabling the tuning of the relaxometric properties. These findings could be useful to deepen the knowledge of hydrogel-CA systems and to achieve an advanced comprehension of the fundamental mechanisms that rule the interaction between MRI CAs and hydrogel matrices, and are responsible for the relaxation enhancement. Further

characterization studies and computational simulations are necessary to insight the water behaviour within polymeric matrices in the presence of metal chelates and the potential impact that these structures can have on the relaxometric properties of clinically used CAs and, therefore, on the performance of MRI diagnosis.

The knowledge of these complex systems could be scaled to nanoscale dimensions, in particular to our case study, inspiring the development of a new class of nanostructured MRI CAs with highly tunable relaxometric properties.

IV.2.2.5 Study of hydrogel structural parameters enhancing relaxometric properties of Gd-based CAs within cHANPs

By the above-reported experiments, we have proved that a systematic tunability can be achieved by varying the crosslinking degree of the hydrogel nanoparticles in the presence of Gd-DTPA accurately (Chapter 2 and 3). A narrow or a broad distribution of relaxation rates on the DVS concentration is showed with regards to changes in the water dynamics, hydrogel conformation and slow motion of the CAs. High control of the parameters is mainly reached through microfluidic approach⁶⁶.

Starting from the observation of a peculiar swelling behavior (Figure IV-7) and in vitro relaxometric properties of the cHANPs (Figure III-4 in Chapter 3), we propose an explanation of how the hydrogel structural parameters can be used to improve the relaxometric properties of CAs.⁶⁷

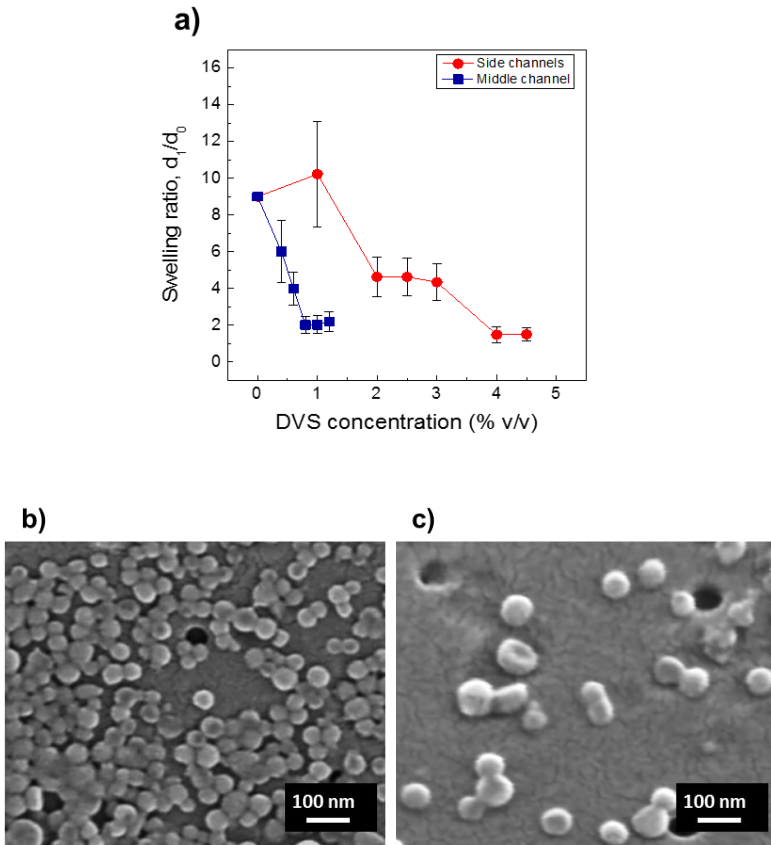


Figure IV-7. Swelling Behavior of cHANPs. (a) Swelling Ratio of crosslinked Hyaluronic Acid Nanoparticles (cHANPs) versus DVS concentration after 48 hours in water at “standard conditions” by injecting DVS (-■-) in the middle channel at Span80 0.5% v/v under strict control of temperature and (-●-) in the side channels at pH of 12.3. (b) FE-SEM images of cHANPs in water by adding DVS in the side channels. (c) 15° C tilted FE-SEM image of cHANPs in the same conditions of (b).

According to Flory-Rehner calculations,⁶⁸ we have determined the crosslink density (ν_c) and mesh size (ξ) of cHANPs in water after 48 hr (see *Appendix V.II* for details about calculations). It

has been already reported⁶⁷ that lower molecular weight films gave rise to decreased molecular weights between crosslinks as well as increased effective crosslink densities and decreased mesh size. Even in our results, a general increase of the crosslink density by increasing the DVS concentration is also evident for both strategies in Figure IV-8a but a different maximum value is achieved. Furthermore, as expected, by increasing the crosslink density, a reduction in mesh size is also obtained until to a certain extent (Figure IV-8b). However, at the most stable conditions (0.8 and 4% v/v DVS) i.e. in the absence of swelling for 48 h, we observe a difference in the crosslink density for the two strategies but not a significant variation in the achieved mesh size. Indeed, a mesh size of about 1.5 nm is reached for DVS 4% v/v (side channels) and of about 2 nm for DVS 0.8% v/v (middle channel).

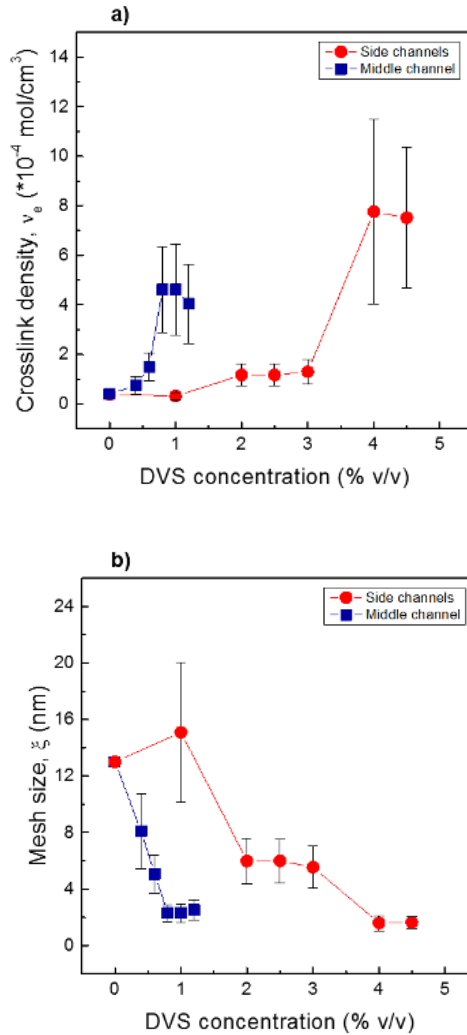


Figure IV-8. Hydrogel parameters. (a) Crosslink density and (b) Mesh size versus DVS concentration for Gd-DTPA loaded cHANPs obtained by injecting DVS (●) in the side channels and (■) in the middle channel.

The relationship between the measured structural parameters of the hydrogel and changes in CA's relaxivity is also examined Figure IV-9a and b. In our system, even if the mesh sizes calculated for both strategies are similar, the highest relaxivity is not observed at the maximum crosslink density, hypothesizing that an optimal equilibrium among the species should be achieved to boost the relaxometric properties.

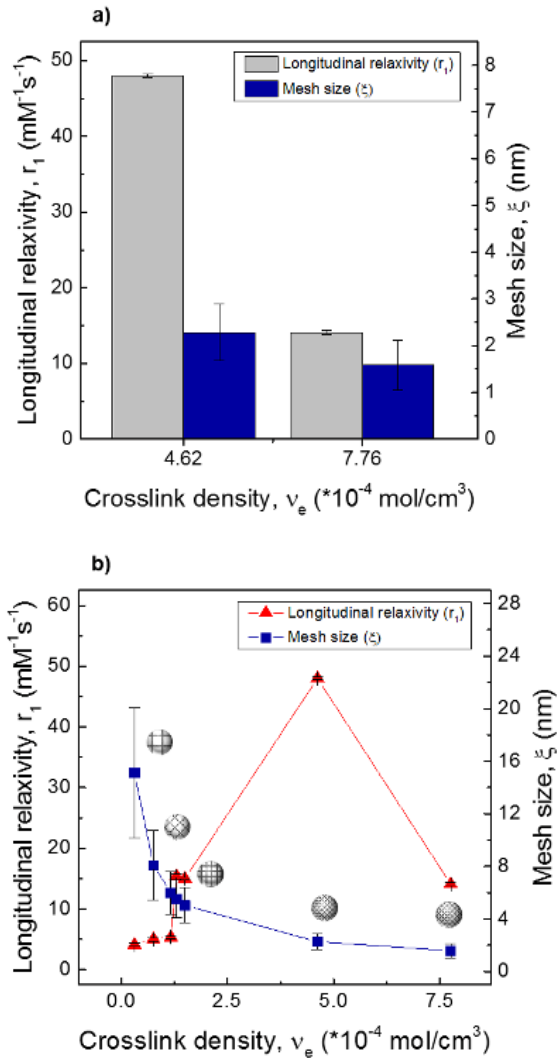


Figure IV-9. Effect of the Hydrodentivity. (a) Bar chart of longitudinal relaxivity (gray columns) and mesh size (blue columns) values computed at different crosslink densities. (b) Mesh size versus crosslink density (-■-) and corresponding relaxivity values (-▲-) along with a graphical representation of cHANPs' polymer network at different mesh size values.

IV.2.2.6 Definition of Hydrodentivity as a property referring to the Hydrogels/Gd-based CAs interaction

Results show so far that *Hydrodentivity* can be proposed as a new concept to summarize the complex equilibrium formed by elastic stretches of polymer chains, water osmotic pressure and hydration degree of Gd-based CAs able to boost the relaxivity.

Indeed, at the achieved minimum mesh size, crosslink density is responsible for the elastodynamic of the hydrogel and is representative of the water amount within the polymer meshes, which in turn is related to the osmotic pressure. Our results also show that the reduction in the elasticity of the matrix with the increase of the crosslink density does not correspond to a maximum enhancement of the relaxivity. It is probably due to the expelled water from the hydrogel network⁶⁹ that causes a reduction in the osmotic pressure within the water compartments of the meshes and a decrease of the hydrated status of Gd-DTPA, thus limiting the enhancement of the relaxometric properties in the nanostructures. These conditions promote the formation of water compartments containing Gd-DTPA called “Gado-Meshes”.

It is also well-known that the crosslink density also acts on the water diffusion, which decreases when the crosslink density increases and its slowdown in diffusion is more severe at the polymer-water interface^{70,71}. Even in the Gd-loaded cHANPs, the water diffusion at various crosslink densities is correlated with the water hydrogen bonding dynamics, and the variation of diffusion coefficient with

crosslink density is related to the variation of water content in different crosslink densities. Therefore, by changing further the properties of the “Gado-Meshes” through the crosslinking reaction, relaxivity increases to an even greater extent due to the *Hydrodentivity* because of the tuning of the crosslink density and, consequently, of the aggregated water state and slow moving of the CAs.

As the *Hydrodentivity* of CAs within the Gado-Mesh does not involve the chemical modification of the CAs, the observed enhancement in relaxivity is induced by the synergistic interaction of the aggregated water with the hydrogel matrix and Gd-DTPA. Indeed, according to the Solomon- Bloembergen-Morgan theory, this effect promotes both (§) a further reduction of the water mobility and diffusion, inducing an increase of the residence lifetime (τ_M) and characteristic diffusion time (τ_D) of the inner and outer sphere; and (§§) changes in hydrogel structures leading to the formation of nanocompartments enwrapping Gd-based CAs, causing a slow motion of the CAs and, therefore, an increase of the rotational correlation time (τ_R) intrinsic of the chelate. Furthermore, it is reasonable that the conditions, reached in the Gado-Mesh, control even the water exchange and, therefore, the relaxivity. Indeed, relaxivity can be limited if the water exchange is too slow because the relaxation effect is poorly transmitted to the bulk. However, relaxivity can also be reduced if the water exchange is too fast because the water is not coordinated to the GdCAs long enough to be relaxed.⁷² In the proposed system, at some degree of

Hydrodenticity, the hydrated status of Gd complexes, the elastodynamic response of HA and the osmotic pressure result probably in a much slower rotation. At this point, the importance of water exchange becomes significant, but the improved relaxivity of Gd-loaded cHANPs confirms that water diffusion is high enough, and the process for relaxing the water protons of aggregated water is in any case very efficient. We have already demonstrated cHANPs themselves do not contribute to the relaxivity of the system (Figure III-6). Thus, the increase in the relaxivity of the loaded cHANPs can be attributed solely to the formation of the Gado-Mesh and to the *Hydrodenticity* achieved in their organization that influences the relaxivity through the characteristic correlation times above mentioned.

Modulation of the *Hydrodenticity* through the: (i) elastic stretching of the polymer meshes (ii) osmotic pressure and (iii) hydrated state of Gd-DTPA contributes to the changes of the Inner and Outer-Sphere of the CAs. Therefore, through the hydrogel structural parameters, we can produce a library of functional nanostructures on the needs of a particular pathology, field and material properties.

Results could lead to the identification of a personalized diagnostic window (Figure IV-10) that can define the range of optimal properties between the hydrogel matrix and the CAs, being more efficient in treating a particular disease, avoiding

toxic effects and increasing the performance of the MRI acquisitions.

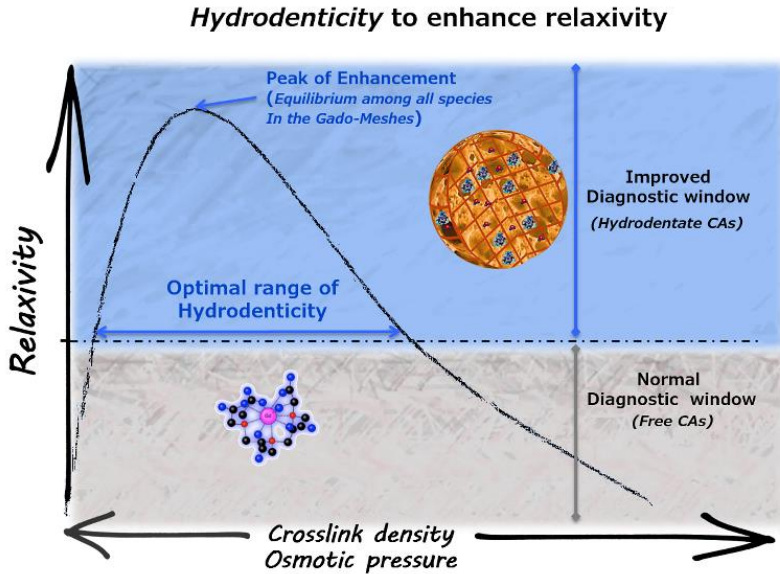


Figure IV-10. Hydrodentcity to enhance relaxivity. Schematic illustration of an improved diagnostic window in which it is possible to obtain a medical device for clinical use in the MRI field able to overcome the limitations related to the use of commercial CAs such as low relaxivity, limited acquisition time and reduced tissue specificity.

IV.3 Conclusions

Here, a study of the interactions involved in polymer-hydrogel-based CA solutions has been presented, aiming at understanding the key role of the water as a mediating agent that acts at the interface between the polymer and the metal chelate and determines both the polymer conformation and the relaxation enhancement. We are able to

individuate by a calorimetric study the energetic contribution in the bulk derived by the interference between the components HA/Water and CAs and how this contribution can modify the hydrogel structure. After, we have highlighted how the water dynamics in a hydrogel matrix can interfere with the relaxation properties of the Gd-based CAs. Based also on these findings on hydrogel matrices, the new concept of Hydrodentivity is here defined for the first time to intend the peculiar environment within the nanostructures composed by the ternary system, hydrogel/water/CAs able to improve the relaxometric properties of CAs. Parameters related to the hydrodentivity are individuated and explained, supported by the literature and a theoretical explanation is fully provided by the consolidated Flory-Rhener theory.

The microfluidic approach is only used as a tool to prove that *Hydrodentivity* can be modulated to obtain desired crosslink density, mesh size, hydrophilicity and loading capability, playing on the biodegradable behavior and relaxometric properties of the Gd-loaded nanostructures. Results are experimentally proving and modeling the relation between the structural parameters of the cHANPs and their improved relaxometric properties. This effect results from the complex equilibrium established by the elastic stretches of polymer chains, water osmotic pressure and hydration degree of GdCAs, that we have called *Hydrodentivity*.

Through the definition of this new concept, we aim to contribute to the advances in the solution of the both physical and biological limits regarding the clinical use of CAs, demonstrating that it is possible to increase their relaxivity by tuning the structural parameters of hydrogel nanoparticles, and, at the same time, improving potentially the tissue specificity, stability of the chelates, imaging diagnostic window and reducing the administration dosage. Indeed, starting from the observation of the swelling ratio, we show that by tuning the hydrogel matrix containing a CA it is possible to affect the dipolar coupling between the electronic magnetic moment of the metal ion and the nuclear magnetic moment of the water nuclei (relaxation rate).

IV.4 References

- 1 Zhou, Z. & Lu, Z. R. Gadolinium-based contrast agents for magnetic resonance cancer imaging. *Wiley Interdisciplinary Reviews: Nanomedicine and Nanobiotechnology* **5**, 1-18 (2013).
- 2 Caravan, P. Strategies for increasing the sensitivity of gadolinium based MRI contrast agents. *Chemical Society Reviews* **35**, 512-523, doi:10.1039/b510982p (2006).
- 3 Bruckman, M. A., Yu, X. & Steinmetz, N. F. Engineering Gd-loaded nanoparticles to enhance MRI sensitivity via T1 shortening. *Nanotechnology* **24**, 462001 (2013).
- 4 McDonald, R. J. *et al.* Intracranial Gadolinium Deposition after Contrast-enhanced MR Imaging. *Radiology* **275**, 772-782, doi:10.1148/radiol.15150025 (2015).
- 5 Sethi, R. *et al.* Enhanced MRI relaxivity of Gd³⁺-based contrast agents geometrically confined within porous nanoconstructs. *Contrast Media & Molecular Imaging* **7**, 501-508, doi:10.1002/cmml.1480 (2012).
- 6 Yang, J. J. *et al.* Rational design of protein-based MRI contrast agents. *Journal of the American Chemical Society* **130**, 9260-9267, doi:10.1021/ja800736h (2008).
- 7 Netti, P. A. Nano-engineered bioactive interfaces. *Interface Focus* **4**, doi:10.1098/rsfs.2013.0065 (2014).
- 8 Wang, X., He, J., Wang, Y. & Cui, F.-Z. Hyaluronic acid-based scaffold for central neural tissue engineering. *Interface Focus* **2**, 278-291, doi:10.1098/rsfs.2012.0016 (2012).
- 9 Wu, C. & Chang, J. Mesoporous bioactive glasses: structure characteristics, drug/growth factor delivery and bone regeneration application. *Interface Focus* **2**, 292-306, doi:10.1098/rsfs.2011.0121 (2012).
- 10 Ahearne, M. Introduction to cell-hydrogel mechanosensing. *Interface Focus* **4**, doi:10.1098/rsfs.2013.0038 (2014).
- 11 Fadeeva, E., Deiwick, A., Chichkov, B. & Schlie-Wolter, S. Impact of laser-structured biomaterial interfaces on guided cell responses. *Interface Focus* **4**, doi:10.1098/rsfs.2013.0048 (2014).
- 12 Bhowmik, D., Chiranjib, C. R., Tripathi, K. & Kumar, K. S. Nanomedicine-an overview. *International Journal of PharmTech Research* **2**, 2143-2151 (2010).
- 13 Lacroix, L.-M., Delpech, F., Nayral, C., Lachaize, S. & Chaudret, B. New generation of magnetic and luminescent nanoparticles for in vivo real-time imaging. *Interface Focus* **3**, doi:10.1098/rsfs.2012.0103 (2013).
- 14 Li, H., LaBean, T. H. & Leong, K. W. Nucleic acid-based nanoengineering: novel structures for biomedical applications. *Interface Focus* **1**, 702-724, doi:10.1098/rsfs.2011.0040 (2011).

- 15 Shen, Y. *et al.* Antisense peptide nucleic acid-functionalized cationic nanocomplex for in vivo mRNA detection. *Interface Focus* **3**, doi:10.1098/rsfs.2012.0059 (2013).
- 16 Sierra-Martin, B. & Fernandez-Barbero, A. Multifunctional hybrid nanogels for theranostic applications. *Soft Matter* **11**, 8205-8216, doi:10.1039/c5sm01789k (2015).
- 17 Raemdonck, K., Demeester, J. & De Smedt, S. Advanced nanogel engineering for drug delivery. *Soft Matter* **5**, 707-715, doi:10.1039/b811923f (2009).
- 18 Zhu, W. & Artemov, D. Biocompatible blood pool MRI contrast agents based on hyaluronan. *Contrast Media & Molecular Imaging* **6**, 61-68, doi:10.1002/cmimi.404 (2011).
- 19 Berezin, M. Y. *Nanotechnology for Biomedical Imaging and Diagnostics: From Nanoparticle Design to Clinical Applications*. (Wiley, 2015).
- 20 Davies, G.-L., Kramberger, I. & Davis, J. J. Environmentally responsive MRI contrast agents. *Chemical Communications* **49**, 9704-9721, doi:10.1039/c3cc44268c (2013).
- 21 Masotti, A. *et al.* Synthesis and characterization of polyethylenimine-based iron oxide composites as novel contrast agents for MRI. *Magnetic Resonance Materials in Physics Biology and Medicine* **22**, 77-87, doi:10.1007/s10334-008-0147-x (2009).
- 22 Corti, M. *et al.* Magnetic and relaxometric properties of polyethylenimine-coated superparamagnetic MRI contrast agents. *Journal of Magnetism and Magnetic Materials* **320**, E316-E319, doi:10.1016/j.jmmm.2008.02.115 (2008).
- 23 Xiao, Y., Xue, R., You, T., Li, X. & Pei, F. A new biodegradable and biocompatible gadolinium (III) -polymer for liver magnetic resonance imaging contrast agent. *Magnetic Resonance Imaging* **33**, 822-828, doi:10.1016/j.mri.2015.03.002 (2015).
- 24 Jeong, S. Y. *et al.* Biocompatible Polyhydroxyethylaspartamide-based Micelles with Gadolinium for MRI Contrast Agents. *Nanoscale Research Letters* **5**, 1970-1976, doi:10.1007/s11671-010-9734-7 (2010).
- 25 Courant, T. *et al.* Hydrogels Incorporating GdDOTA: Towards Highly Efficient Dual T1/T2 MRI Contrast Agents. *Angewandte Chemie-International Edition* **51**, 9119-9122, doi:10.1002/anie.201203190 (2012).
- 26 Li, Y. *et al.* Macromolecular Ligands for Gadolinium MRI Contrast Agents. *Macromolecules* **45**, 4196-4204, doi:10.1021/ma300521c (2012).
- 27 Courant, T. *et al.* Biocompatible nanoparticles and gadolinium complexes for MRI applications. *Comptes Rendus Chimie* **16**, 531-539, doi:10.1016/j.crci.2012.12.010 (2013).
- 28 Arosio, P. *et al.* Hybrid iron oxide-copolymer micelles and vesicles as contrast agents for MRI: impact of the nanostructure on the relaxometric properties. *Journal of Materials Chemistry B* **1**, 5317-5328, doi:10.1039/c3tb00429e (2013).

- 29 Port, M. *et al.* Impact of rigidification on relaxometric properties of a tricyclic tetraazatriacetic gadolinium chelate. *Contrast Media & Molecular Imaging* **1**, 121-127, doi:10.1002/cmmi.99 (2006).
- 30 Ananta, J. S. *et al.* Geometrical confinement of gadolinium-based contrast agents in nanoporous particles enhances T-1 contrast. *Nature Nanotechnology* **5**, 815-821, doi:10.1038/nnano.2010.203 (2010).
- 31 Pasqui, D., De Cagna, M. & Barbucci, R. Polysaccharide-Based Hydrogels: The Key Role of Water in Affecting Mechanical Properties. *Polymers* **4**, 1517-1534, doi:10.3390/polym4031517 (2012).
- 32 Oliveira, R. N. *et al.* Mechanical properties and in vitro characterization of polyvinyl alcohol-nano-silver hydrogel wound dressings. *Interface Focus* **4**, doi:10.1098/rsfs.2013.0049 (2014).
- 33 Manetti, C., Casciani, L. & Pescosolido, N. Diffusive contribution to permeation of hydrogel contact lenses: theoretical model and experimental evaluation by nuclear magnetic resonance techniques. *Polymer* **43**, 87-92, doi:10.1016/s0032-3861(01)00559-6 (2002).
- 34 Pal, K., Banthia, A. K. & Majumdar, D. K. Polymeric Hydrogels: Characterization and Biomedical Applications. *Designed Monomers and Polymers* **12**, 197-220, doi:10.1163/156855509x436030 (2009).
- 35 Omidian, H. & Park, K. Swelling agents and devices in oral drug delivery. *Journal of Drug Delivery Science and Technology* **18**, 83-93 (2008).
- 36 Wood, M. L. & Hardy, P. A. Proton relaxation enhancement. *J. Magn. Reson. Imaging* **3**, 149-156 (1993).
- 37 Solomon, I. Relaxation processes in a system of two spins. *Physical Review* **99**, 559 (1955).
- 38 Bloembergen, N. Proton relaxation times in paramagnetic solutions. *The Journal of Chemical Physics* **27**, 572-573 (1957).
- 39 Xue, S., Qiao, J., Pu, F., Cameron, M. & Yang, J. J. Design of a novel class of protein-based magnetic resonance imaging contrast agents for the molecular imaging of cancer biomarkers. *Wiley Interdisciplinary Reviews-Nanomedicine and Nanobiotechnology* **5**, 163-179, doi:10.1002/wnan.1205 (2013).
- 40 Huang, M., Huang, Z. L., Bilgen, M. & Berkland, C. Magnetic resonance imaging of contrast-enhanced polyelectrolyte complexes. *Nanomedicine-Nanotechnology Biology and Medicine* **4**, 30-40, doi:10.1016/j.nano.2007.10.085 (2008).
- 41 Rotz, M. W. *et al.* High Relaxivity Gd(III) - DNA Gold Nanostars: Investigation of Shape Effects on Proton Relaxation. *Acs Nano* **9**, 3385-3396, doi:10.1021/nn5070953 (2015).
- 42 Wang, Z. T. *et al.* Water-soluble amorphous iron oxide nanoparticles synthesized by a quickly pestling and nontoxic method at room temperature as MRI contrast agents. *Chemical Engineering Journal* **235**, 231-235, doi:10.1016/j.cej.2013.09.042 (2014).
- 43 Wang, G. S., Ma, Y. Y., Wei, Z. Y. & Qi, M. Development of multifunctional cobalt ferrite/graphene oxide nanocomposites for magnetic

- resonance imaging and controlled drug delivery. *Chemical Engineering Journal* **289**, 150-160, doi:10.1016/j.cej.2015.12.072 (2016).
- 44 Lakshmanan, S., Holmes, W. M., Sloan, W. T. & Phoenix, V. R. Nanoparticle transport in saturated porous medium using magnetic resonance imaging. *Chemical Engineering Journal* **266**, 156-162, doi:10.1016/j.cej.2014.12.076 (2015).
- 45 Ma, L. L. *et al.* Small Multifunctional Nanoclusters (Nanoroses) for Targeted Cellular Imaging and Therapy. *Acs Nano* **3**, 2686-2696, doi:10.1021/nn900440e (2009).
- 46 Necas, J., Bartosikova, L., Brauner, P. & Kolar, J. Hyaluronic acid (hyaluronan): a review. *Veterinarni Medicina* **53**, 397-411 (2008).
- 47 Lu, Z.-R., Mohs, A. M., Zong, Y. & Feng, Y. Polydisulfide Gd(III) chelates as biodegradable macromolecular magnetic resonance imaging contrast agents. *International Journal of Nanomedicine* **1**, 31-40, doi:10.2147/nano.2006.1.1.31 (2006).
- 48 Yoo, H., Paranjli, R. & Pollack, G. H. Impact of Hydrophilic Surfaces on Interfacial Water Dynamics Probed with NMR Spectroscopy. *J. Phys. Chem. Lett.* **2**, 532-536, doi:10.1021/jz200057g (2011).
- 49 Ori, G., Villemot, F., Viau, L., Vioux, A. & Coasne, B. Ionic liquid confined in silica nanopores: molecular dynamics in the isobaric-isothermal ensemble. *Mol. Phys.* **112**, 1350-1361, doi:10.1080/00268976.2014.902138 (2014).
- 50 Ori, G., Massobrio, C., Pradel, A., Ribes, M. & Coasne, B. Structure and Dynamics of Ionic Liquids Confined in Amorphous Porous Chalcogenides. *Langmuir* **31**, 6742-6751, doi:10.1021/acs.langmuir.5b00982 (2015).
- 51 Chiessi, E., Cavaliere, F. & Paradossi, G. Water and polymer dynamics in chemically cross-linked hydrogels of poly(vinyl alcohol): A molecular dynamics simulation study. *Journal of Physical Chemistry B* **111**, 2820-2827, doi:10.1021/jp0671143 (2007).
- 52 Martinez, J. C. *et al.* *Isothermal Titration Calorimetry: Thermodynamic Analysis of the Binding Thermograms of Molecular Recognition Events by Using Equilibrium Models.* (2013).
- 53 Gouin, S. & Winnik, F. M. Quantitative assays of the amount of diethylenetriaminepentaacetic acid conjugated to water-soluble polymers using isothermal titration calorimetry and colorimetry. *Bioconjugate Chemistry* **12**, 372-377, doi:10.1021/bc000109w (2001).
- 54 Kabiri, M. & Unsworth, L. D. Application of Isothermal Titration Calorimetry for Characterizing Thermodynamic Parameters of Biomolecular Interactions: Peptide Self-Assembly and Protein Adsorption Case Studies. *Biomacromolecules* **15**, 3463-3473, doi:10.1021/bm5004515 (2014).
- 55 Ponsiglione, A., Russo, M., Netti, P. & Torino, E. Impact of biopolymer matrices on relaxometric properties of contrast agents. *Interface Focus* **20160061**, doi:<http://dx.doi.org/10.1098/rsfs.2016.0061> (2016).

- 56 Velasco, D., Tumarkin, E. & Kumacheva, E. Microfluidic Encapsulation of Cells in Polymer Microgels. *Small* **8**, 1633-1642, doi:10.1002/smll.201102464 (2012).
- 57 Peppas, N. A., Huang, Y., Torres-Lugo, M., Ward, J. H. & Zhang, J. Physicochemical, foundations and structural design of hydrogels in medicine and biology. *Annual Review of Biomedical Engineering* **2**, 9-29, doi:10.1146/annurev.bioeng.2.1.9 (2000).
- 58 Khabaz, F., Mani, S. & Khare, R. Molecular Origins of Dynamic Coupling between Water and Hydrated Polyacrylate Gels. *Macromolecules*, doi:10.1021/acs.macromol.6b00938 (2016).
- 59 Johnson, D. L. Elastodynamics of gels. *The Journal of Chemical Physics* **77**, 1531-1539 (1982).
- 60 Strom, A., Larsson, A. & Okay, O. Preparation and physical properties of hyaluronic acid-based cryogels. *Journal of Applied Polymer Science* **132**, doi:10.1002/app.42194 (2015).
- 61 Utech, S. & Boccaccini, A. R. A review of hydrogel-based composites for biomedical applications: enhancement of hydrogel properties by addition of rigid inorganic fillers. *Journal of Materials Science* **51**, 271-310, doi:10.1007/s10853-015-9382-5 (2016).
- 62 Stejskal, E. O. & Tanner, J. E. Spin diffusion measurements: spin echoes in the presence of a time-dependent field gradient. *The journal of chemical physics* **42**, 288-292 (1965).
- 63 Caravan, P., Farrar, C. T., Frullano, L. & Uppal, R. Influence of molecular parameters and increasing magnetic field strength on relaxivity of gadolinium- and manganese-based T(1) contrast agents. *Contrast Media & Molecular Imaging* **4**, 89-100, doi:10.1002/cmmi.267 (2009).
- 64 Debroye, E. & Parac-Vogt, T. N. Towards polymetallic lanthanide complexes as dual contrast agents for magnetic resonance and optical imaging. *Chemical Society Reviews* **43**, 8178-8192, doi:10.1039/c4cs00201f (2014).
- 65 Hermann, P., Kotek, J., Kubicek, V. & Lukes, I. Gadolinium(III) complexes as MRI contrast agents: ligand design and properties of the complexes. *Dalton Transactions*, 3027-3047, doi:10.1039/b719704g (2008).
- 66 Russo, M., Bevilacqua, P., Netti, P. A. & Torino, E. A Microfluidic Platform to design crosslinked Hyaluronic Acid Nanoparticles (cHANPs) for enhanced MRI. *Sci. Rep.* (in press).
- 67 Collins, M. N. & Birkinshaw, C. Investigation of the swelling behavior of crosslinked hyaluronic acid films and hydrogels produced using homogeneous reactions. *Journal of Applied Polymer Science* **109**, 923-931, doi:10.1002/app.27631 (2008).
- 68 Leach, J. B., Bivens, K. A., Patrick, C. W. & Schmidt, C. E. Photocrosslinked hyaluronic acid hydrogels: Natural, biodegradable tissue engineering scaffolds. *Biotechnology and Bioengineering* **82**, 578-589, doi:10.1002/bit.10605 (2003).

- 69 Martins Shimojo, A. A., Barbosa Pires, A. M., Lichy, R., Rodrigues, A. A. & Andrade Santana, M. H. The crosslinking degree controls the mechanical, rheological, and swelling properties of hyaluronic acid microparticles. *Journal of Biomedical Materials Research Part A* **103**, 730-737, doi:10.1002/jbm.a.35225 (2015).
- 70 Wu, Y., Joseph, S. & Aluru, N. R. Effect of Cross-Linking on the Diffusion of Water, Ions, and Small Molecules in Hydrogels. *Journal of Physical Chemistry B* **113**, 3512-3520, doi:10.1021/jp808145x (2009).
- 71 Yoshida, R. *et al.* Comb-type grafted hydrogels with rapid deswelling response to temperature changes. *Nature* **374**, 240-242 (1995).
- 72 DeMello, J. & DeMello, A. Microscale reactors: nanoscale products. *Lab on a Chip* **4**, 11N-15N, doi:10.1039/b403638g (2004).
- 73 Wells, L. A., Furukawa, S. & Sheardown, H. Photoresponsive PEG-Anthracene Grafted Hyaluronan as a Controlled-Delivery Biomaterial. *Biomacromolecules* **12**, 923-932, doi:10.1021/bm101233m (2011).
- 74 Kottapalli, A. G. P. *et al.* Nanofibril scaffold assisted MEMS artificial hydrogel neuromasts for enhanced sensitivity flow sensing. *Scientific Reports* **6**, doi:10.1038/srep19336 (2016).

Main Conclusions and Perspectives

A microfluidic-based process has been proposed to design a new class of Magnetic Resonance Imaging (MRI) Contrast Agents (CAs) in form of intravascularly-injectable and biocompatible hydrogel nanostructures able to impact on the relaxometric properties of MRI CAs for potential application in diagnosis and therapy.

In the *first part of the thesis*, the tunability of the hydrogel nanostructures, able to entrap rationally a clinically-relevant Gd-based CA, Gd-DTPA, through a microfluidic flow focusing method, is exploited and monodisperse crosslinked Hyaluronic Acid Nanoparticles (cHANPs) under 50 nm are produced by a controlled nanoprecipitation, overcoming the limits of common batch processes, and guaranteeing an instantaneous formulation and absence of purification step.

The proposed microfluidic method allows a strict control of the physicochemical properties of the nanoparticles and the entrapping of the Gd-DTPA, achieving a low polydispersity of nanoparticles and a high encapsulation efficiency of the metal compound within the nanoparticles. Our findings are interesting to investigate how the microfluidic environment determines the NPs size and stabilization, to facilitate also the further application of this rapidly growing technique.

Furthermore, a crosslinking reaction is studied and performed, simultaneously to the nanoprecipitation, to improve the stability of the

polymer matrix, increase loading capability and reduce swelling effects. Interferences of the CA in the flow focusing behaviour are reported for the first time, and different strategies are proposed to optimize the entrapment of the metal compound. In addition, the encapsulation efficiency of the metal inside the nanoparticles could be adaptable according to needs, and a perfect formulation of the involved species is obtained.

In the *second part of the thesis*, the relaxometric performances are assessed in terms of longitudinal relaxivity r_1 as a function of the crosslinking degree and loading conditions. In *in vitro* and *in vivo* analysis, the r_1 relaxivity of the Gd-loaded cHANPs is shown to increase up to 12 times at specific formulations, without the chemical modification of the relevant clinical chelate. This observation is crucial to lead potentially to a significant reduction of the administration dosage on clinical usage of the CAs and to gain advantages in the imaging modalities based on nanotechnologies. Indeed, the nanoparticles are widely used for the improvement of imaging techniques and the adjustable features reported for our system can potentially reduce limitation linked to a fast clearance from the bloodstream and low detection due to the dependence on the concentration. In fact, Gd-loaded cHANPs ensure an improvement of the time window for clinical imaging acquisitions due to the reduction of long scan time and rapid renal clearance. Finally, readily

functionalized, proposed cHANPs could improve tissue specificity to reach a specific organ or tissue.

It is important to highlight that further benefits of our study are the use of completely biocompatible and FDA approved products, the ease of the synthesis and the scalability of the proposed process.

In the *last part of the thesis*, also a theoretical explanation of how the hydrogel structural parameters can impact on the relaxometric properties of MRI CAs is studied and the key role of the water, which acts at the interface between polymer chains and metal-chelates determining both the relaxation enhancement and the polymer conformation, is investigated. In this scenario, I could observe that by changing structural parameters of a hydrogel matrix containing a CA, through a Microfluidic Flow Focusing approach, it is possible to affect the dipolar coupling between the electronic magnetic moment of the metal ion and the nuclear magnetic moment of the water nuclei (relaxation rate). This effect could result from a complex equilibrium established by the elastic stretches of polymer chains, water osmotic pressure and hydration degree of GdCAs. I have proved how the presence of Gd-DTPA can modify the specific interactions between water and intramolecular hydrogen bonds, inducing a change in polymer conformation, and how, at the same time, the attainment of the aggregated status of the water can improve the relaxometric properties of the Gd chelates, as called *Hydrodentecity*.

In conclusion, I suppose that the proposed approach for characterizing polymer-based CAs could be applied to study the mechanisms involved in several combinations of different types of polymers and metal ions. In fact, our work bridges different disciplines across Material Science, Physics and Engineering and could provide a coherent framework for studying and realizing polymer structures and devices with potential applications in medical diagnostics and therapy. For this reason, I strongly believe that it is likely to be of great interest to the vision of scientists who are involved in the study, the modeling or the development of novel biomaterials and CAs. These findings could be useful to deepen the knowledge of hydrogel-CA systems and to achieve an advanced comprehension of the fundamental mechanisms that rule the interaction between MRI CAs and hydrogel matrices, and are responsible for the relaxation enhancement. Our findings could contribute significantly to the prompt introduction of new advances in the MRI medical devices and could be apply into personalized medicine for each patient, overcoming drawbacks of the commonly used CAs, as well as in the comprehension of the dynamics and properties characterizing magnetic polymer-based materials. In these perspectives, through the tunability of the hydrogel structural parameters, future outlook are addressed to the ability to build a library of functional nanostructures on the needs of a particular pathology, field and material properties. Results could lead to the identification of a personalized diagnostic window that can define the range of

optimal properties between the hydrogel matrix and the CAs, being more efficient in treating a particular disease, avoiding toxic effects and increasing the performance of the MRI acquisitions. Next steps are also addressed to optimize in vivo study for a specific pathology and to perform an active targeting of cHANPs to reach a particular tissue. Furthermore, our efficient, straightforward and scalable developed microfluidic strategies are easy to move to the encapsulation of several drugs for a multimodal imaging or also for application in diagnostics and therapy, simultaneously.

V. Appendix

V.1 ICP-MS Results

Tables below report the detailed results obtained at ICP-MS instrument regarding the three analyzed mice.

Sample ID	Gd 158 (ppb)	g/L	Dil. ratio	tq	Gd-DTPA (MW.)	Molarity (M)	μM
Standard 1	0,100	0,0000001	100	0,00001	547,57	1,82625E-08	0,018262505
<i>RSD</i>	5,5%						
Standard 2	0,499	4,99287E-07	100	4,99287E-05	547,57	9,11823E-08	0,091182302
<i>RSD</i>	9,9%						
Standard 3	0,997	9,9693E-07	100	9,9693E-05	547,57	1,82064E-07	0,182064363
<i>RSD</i>	0,6%						
Standard 4	5,006	5,00647E-06	100	0,000500647	547,57	9,14307E-07	0,914306847
<i>RSD</i>	1,0%						
Standard 5	10,141	1,01414E-05	100	0,001014143	547,57	1,85208E-06	1,852079173
<i>RSD</i>	1,0%						
Standard 6	99,858	9,98581E-05	100	0,009985811	547,57	1,82366E-05	18,23659205
<i>RSD</i>	1,1%						
Standard 7	499,614	0,000499614	100	0,04996139	547,57	9,1242E-05	91,24201489
<i>RSD</i>	3,3%						
Calibration Curves							
T1 liver	0,567	5,66999E-07	100	5,66999E-05	547,57	1,03548E-07	0,103548263
<i>RSD</i>	1,5%						
T1 liver 1	0,562	5,61731E-07	100	5,61731E-05	547,57	1,02586E-07	0,102586086
<i>RSD</i>	2,4%						
T1 liver 2	0,185	1,84868E-07	100	1,84868E-05	547,57	3,37616E-08	0,033761588

<i>RSD</i>	2,0%						
T1 liver 3	0,051	5,09233E-08	100	5,09233E-06	547,57	9,29986E-09	0,009299863
<i>RSD</i>	1,4%						
T1 kydneys 1	0,045	4,51889E-08	100	4,51889E-06	547,57	8,25262E-09	0,008252618
<i>RSD</i>	0,6%						
T1 kidneys 2	0,046	4,60571E-08	100	4,60571E-06	547,57	8,41119E-09	0,008411188
<i>RSD</i>	0,8%						
T1 kydneys 3	0,048	4,78368E-08	100	4,78368E-06	547,57	8,7362E-09	0,008736195
<i>RSD</i>	1,5%						
T1 brain 1	0,027	2,6936E-08	100	2,6936E-06	547,57	4,91919E-09	0,004919188
<i>RSD</i>	4,4%						
T1 brain 2	0,027	2,67781E-08	100	2,67781E-06	547,57	4,89035E-09	0,004890351
<i>RSD</i>	6,3%						
T1 brain 3	0,029	2,87905E-08	100	2,87905E-06	547,57	5,25787E-09	0,005257867
<i>RSD</i>	1,2%						
T1 lungs 1	0,040	4,00208E-08	100	4,00208E-06	547,57	7,3088E-09	0,007308798
<i>RSD</i>	0,3%						
T1 lungs 2	0,043	4,33447E-08	100	4,33447E-06	547,57	7,91582E-09	0,007915819
<i>RSD</i>	2,6%						
T1 lungs 3	0,043	4,33039E-08	100	4,33039E-06	547,57	7,90837E-09	0,007908372
<i>RSD</i>	0,8%						
T1 heart 1	0,163	1,63223E-07	100	1,63223E-05	547,57	2,98086E-08	0,029808608
<i>RSD</i>	0,9%						
T1 heart 2	0,153	1,53475E-07	100	1,53475E-05	547,57	2,80283E-08	0,02802832
<i>RSD</i>	1,4%						
T1 heart 3	0,153	1,52707E-07	100	1,52707E-05	547,57	2,78882E-08	0,027888173
<i>RSD</i>	2,0%						
T1 spleen 1	0,064	6,3958E-08	100	6,3958E-06	547,57	1,16803E-08	0,01168033
<i>RSD</i>	0,7%						
T1 spleen 2	0,081	8,13354E-08	100	8,13354E-06	547,57	1,48539E-08	0,01485388
<i>RSD</i>	1,0%						

T1 spleen 3	0,089	8,92857E-08	100	8,92857E-06	547,57	1,63058E-08	0,016305806
<i>RSD</i>	<i>1,6%</i>						
T2 lungs 1	0,028	2,84027E-08	100	2,84027E-06	547,57	5,18705E-09	0,00518705
<i>RSD</i>	<i>1,9%</i>						
T2 lungs 2	0,070	7,01198E-08	100	7,01198E-06	547,57	1,28056E-08	0,01280564
<i>RSD</i>	<i>0,4%</i>						
T2 lungs 3	0,035	3,4673E-08	100	3,4673E-06	547,57	6,33216E-09	0,006332155
<i>RSD</i>	<i>4,9%</i>						
T2 heart 1	0,021	2,11902E-08	100	2,11902E-06	547,57	3,86985E-09	0,003869854
<i>RSD</i>	<i>3,9%</i>						
T2 heart 2	0,026	2,61761E-08	100	2,61761E-06	547,57	4,78041E-09	0,004780411
<i>RSD</i>	<i>2,1%</i>						
T2 heart 3	0,025	2,53678E-08	100	2,53678E-06	547,57	4,6328E-09	0,0046328
<i>RSD</i>	<i>1,7%</i>						
T2 kydney 1	0,033	3,34313E-08	100	3,34313E-06	547,57	6,1054E-09	0,006105396
<i>RSD</i>	<i>5,0%</i>						
T2 kydney 2	0,038	3,7724E-08	100	3,7724E-06	547,57	6,88934E-09	0,006889342
<i>RSD</i>	<i>4,6%</i>						
T2 kydney 3	0,038	3,82603E-08	100	3,82603E-06	547,57	6,98729E-09	0,006987287
<i>RSD</i>	<i>7,5%</i>						
T2 spleen 1	0,058	5,75705E-08	100	5,75705E-06	547,57	1,05138E-08	0,010513813
<i>RSD</i>	<i>1,7%</i>						
T2 spleen 2	0,067	6,65695E-08	100	6,65695E-06	547,57	1,21573E-08	0,012157251
<i>RSD</i>	<i>3,0%</i>						
T2 spleen 3	0,062	6,24191E-08	100	6,24191E-06	547,57	1,13993E-08	0,011399287
<i>RSD</i>	<i>1,1%</i>						
T2 brain 1	0,020	1,96202E-08	100	1,96202E-06	547,57	3,58314E-09	0,003583138
<i>RSD</i>	<i>1,9%</i>						
T2 brain 2	0,021	2,05003E-08	100	2,05003E-06	547,57	3,74386E-09	0,003743861
<i>RSD</i>	<i>1,0%</i>						
T2 brain 3	0,031	3,13312E-08	100	3,13312E-06	547,57	5,72186E-09	0,00572186

<i>RSD</i>	1,4%						
T2 liver 1	0,077	7,67027E-08	100	7,67027E-06	547,57	1,40078E-08	0,014007836
<i>RSD</i>	5,3%						
T2 liver 2	0,088	8,84826E-08	100	8,84826E-06	547,57	1,61591E-08	0,016159136
<i>RSD</i>	2,1%						
T2 liver 3	0,089	8,88013E-08	100	8,88013E-06	547,57	1,62173E-08	0,016217344
<i>RSD</i>	1,0%						
T3 heart 1	0,023	2,2778E-08	100	2,2778E-06	547,57	4,15983E-09	0,004159828
<i>RSD</i>	2,3%						
T3 heart 2	0,026	2,55011E-08	100	2,55011E-06	547,57	4,65715E-09	0,004657148
<i>RSD</i>	3,1%						
T3 heart 3	0,040	3,99796E-08	100	3,99796E-06	547,57	7,30127E-09	0,00730127
<i>RSD</i>	7,2%						
T3 lungs 1	0,025	2,50653E-08	100	2,50653E-06	547,57	4,57755E-09	0,004577548
<i>RSD</i>	2,0%						
T3 lungs 2	0,026	2,59208E-08	100	2,59208E-06	547,57	4,7338E-09	0,004733796
<i>RSD</i>	1,4%						
T3 lungs 3	0,023	2,32789E-08	100	2,32789E-06	547,57	4,2513E-09	0,004251304
<i>RSD</i>	1,2%						
T3 kydneyes 1	0,046	4,61644E-08	100	4,61644E-06	547,57	8,43078E-09	0,008430775
<i>RSD</i>	2,1%						
T3 kydneyes 2	0,049	4,91646E-08	100	4,91646E-06	547,57	8,97869E-09	0,008978694
<i>RSD</i>	4,1%						
T3 kydneyes 3	0,046	4,62307E-08	100	4,62307E-06	547,57	8,44288E-09	0,008442877
<i>RSD</i>	4,9%						
T3 spleen 1	0,137	1,37454E-07	100	1,37454E-05	547,57	2,51026E-08	0,025102568
<i>RSD</i>	4,3%						
T3 spleen 2	0,140	1,39908E-07	100	1,39908E-05	547,57	2,55507E-08	0,02555068
<i>RSD</i>	1,2%						
T3 spleen 3	0,141	1,41037E-07	100	1,41037E-05	547,57	2,57568E-08	0,025756827
<i>RSD</i>	2,2%						

T3 brain 1	0,022	2,1835E-08	100	2,1835E-06	547,57	3,98762E-09	0,003987624
<i>RSD</i>	2,9%						
T3 brain 2	0,023	2,30956E-08	100	2,30956E-06	547,57	4,21783E-09	0,004217833
<i>RSD</i>	1,1%						
T3 brain 3	0,023	2,32796E-08	100	2,32796E-06	547,57	4,25143E-09	0,004251433
<i>RSD</i>	1,6%						
T3 liver 1	0,124	1,24019E-07	100	1,24019E-05	547,57	2,2649E-08	0,022649
<i>RSD</i>	2,0%						
T3 liver 2	0,126	1,25577E-07	100	1,25577E-05	547,57	2,29335E-08	0,022933511
<i>RSD</i>	3,0%						
T3 liver3	0,127	1,27082E-07	100	1,27082E-05	547,57	2,32084E-08	0,023208377
<i>RSD</i>	3,7%						
T1 blood 1	1,947878188	1,94788E-06	100	0,000194788	547,57	3,55731E-07	0,355731356
<i>RSD</i>	13,3%						
T1 blood 2	0,655	6,54747E-07	100	6,54747E-05	547,57	1,19573E-07	0,119573256
<i>RSD</i>	3,7%						
T1 blood 3	0,642	6,4184E-07	100	6,4184E-05	547,57	1,17216E-07	0,117216082
<i>RSD</i>	1,4%						
T2 blood 1	0,365	3,64506E-07	100	3,64506E-05	547,57	6,65679E-08	0,06656793
<i>RSD</i>	0,2%						
T2 blood 2	0,248	2,48365E-07	100	2,48365E-05	547,57	4,53578E-08	0,045357757
<i>RSD</i>	2,6%						
T2 blood 3	0,377	3,77385E-07	100	3,77385E-05	547,57	6,892E-08	0,068919953
<i>RSD</i>	0,5%						
T3 blood 1	0,316	3,15648E-07	100	3,15648E-05	547,57	5,76453E-08	0,057645291
<i>RSD</i>	0,7%						
T3 blood 2	0,343	3,43006E-07	100	3,43006E-05	547,57	6,26415E-08	0,062641512
<i>RSD</i>	1,2%						
T3 blood 3	0,375	3,75271E-07	100	3,75271E-05	547,57	6,85339E-08	0,068533943
<i>RSD</i>	0,9%						

V.2 Calculations of the hydrogel network parameters

As previously described, studies on the swelling behavior of the nanoparticles are conducted in water at room temperature and the obtained results, in terms of swelling ratio, are used to estimate the following hydrogel structural parameters of the cHANPs:

- $\overline{M}c$: molecular weight between crosslinks (g/mol);
- ν_e : effective crosslink density (mol/cm³);
- ξ : mesh size (nm).

In order to compute the above mentioned parameters, a simplified version of the Flory-Rehner equations are used.

Firstly, the average molecular weight between crosslinks ($\overline{M}c$) are computed using the following equation:

$$Q_v^{5/3} = \frac{\bar{v} \overline{M}c}{V_1} \left(\frac{1}{2} - \chi \right) \quad (2)$$

where Q_v is the volumetric swelling ratio, \bar{v} is specific volume of polymer (0.814 cm³/g for HA)¹, V_1 is molar volume of solvent (18 mol/cm³ for water)², χ is polymer-solvent interaction parameter (0.473 for HA)³. The volumetric swelling ratio, Q_v , is estimated based on the approximate diameter ratio, determined experimentally by comparing the diameters of the swelled cHANPs with the cHANPs' diameters in Ethanol, i.e. before the hydration of the nanoparticles in water.

Differently from the previous works²⁻⁴, in which the volumetric swelling ratio is estimated from the mass swelling ratio by dividing the sample mass after swelling by the dry sample mass, no dehydration of the nanoparticles is performed in order to keep unchanged the

structure and the shape of the Gd-DTPA loaded cHANPs. Therefore, the nanoparticles' diameter measured in Ethanol is used as the reference value to compute the volumetric swelling ratio. This allows us to avoid the alteration of the Gado-Mesh network and the release of the entrapped Gd-DTPA caused by the dehydration process, making us able to properly investigate the relationship between the cHANPs' hydrogel structure and the relaxivity values, which strictly rely on the encapsulation of the contrast agent and on the hydrogel parameters. After \overline{M}_c is estimated, the effective crosslink density, ν_e , is determined from the following equation:

$$\nu_e = \frac{\rho_p}{\overline{M}_c} \quad (3)$$

where ρ_p is the density of polymer (1.229 g/cm³ for HA)⁴.

The water swollen hydrogels mesh size, ξ , is calculated by the following equation:

$$\xi = Q_v^{1/3} \sqrt{\overline{r}_o^2} \quad (4)$$

where $\sqrt{\overline{r}_o^2}$ is the root-mean square distance between crosslinks, specifically reported for HA by Collins et al.³ as follows:

$$\sqrt{\left(\frac{\overline{r}_o^2}{2n}\right)} \cong 2.4 \text{ (nm)} \quad (5)$$

where n is the number of monomer units for HA. For HA with a molecular weight (M_n) of $\sim 4 \cdot 10^5$, n is ~ 100 , which gives the following estimation of $\sqrt{\overline{r}_o^2}$:

$$\sqrt{r_o^2} = 0.035 \sqrt{M_n} \quad (6)$$

Finally, the mesh size can be calculated by combining equations (4) and (6) as follows:

$$\xi = 0.035 \sqrt{M_c} Q_v^{1/3} \quad (7)$$

Estimated values of all swelling study parameters, Q_v , $\overline{M_c}$, v_e and ξ should be considered as approximate values on account of certain assumptions considered in Flory-Rehner calculations and for our specific systems. However, these values can be used for making comparisons between various network features of different hydrogel nanoparticles.

The following tables report all the computed values for swelled cHANPs after 48 hr.

Table 6. cHANPs network parameters. Hydrogel network parameters of cHANPs after 48 h of swelling, obtained by adding DVS a) in the middle channel and b) in the side channels.

a)

<i>DVS</i> [% <i>v/v</i>]	Volumetric swelling ratio		Molecular mass between two crosslinked points [$\cdot 10^3$ g/mol]		Effective crosslink density [$\cdot 10^{-5}$ mol/cm ³]		Mesh size [nm]	
	<i>Q_v</i>		\bar{M}_C		<i>v_e</i>		$\bar{\epsilon}$	
	<i>mean</i>	<i>SD</i>	<i>mean</i>	<i>SD</i>	<i>mean</i>	<i>SD</i>	<i>mean</i>	<i>SD</i>
0.00	9.00	0	31.9	0	3.85	0	13.00	0
1.00	10.23	2.87	39.5	18.5	3.11	1.46	15.09	4.94
2.00	4.63	1.06	10.5	4.04	11.7	4.47	5.99	1.61
2.50	4.63	1.04	10.5	3.93	11.7	4.35	5.99	1.56
3.00	4.34	0.99	9.47	3.60	13.0	4.94	5.56	1.48
4.00	1.49	0.43	1.58	0.760	77.6	37.2	1.59	0.53
4.50	1.51	0.34	1.64	0.619	75.1	28.4	1.63	0.43

b)

<i>DVS</i> [% <i>v/v</i>]	Volumetric swelling ratio		Molecular mass between two crosslinked points [*10 ³ g/mol]		Effective crosslink density [*10 ⁻⁵ mol/cm ³]		Mesh size [nm]	
	<i>Q_v</i>		\bar{M}_C		<i>v_e</i>		Ξ	
	<i>mean</i>	<i>SD</i>	<i>mean</i>	<i>SD</i>	<i>mean</i>	<i>SD</i>	<i>mean</i>	<i>SD</i>
0.00	9.00	0	31.9	0	3.85	0	13.00	0
0.40	6.00	1.69	16.2	7.60	7.57	3.55	8.10	2.66
0.60	4.00	0.91	8.26	3.14	14.9	5.67	5.05	1.35
0.80	2.03	0.46	2.66	1.00	46.2	17.4	2.29	0.60
1.00	2.03	0.49	2.66	1.07	46.2	18.5	2.29	0.64
1.20	2.20	0.53	3.05	1.21	40.3	16.1	2.51	0.70
1.60	25.71	7.36	183	87.5	0.670	0.319	44.25	14.77

V.3 References

- 1 Wells, L. A., Furukawa, S. & Sheardown, H. Photoresponsive PEG-Anthracene Grafted Hyaluronan as a Controlled-Delivery Biomaterial. *Biomacromolecules* **12**, 923-932, doi:10.1021/bm101233m (2011).
- 2 Leach, J. B., Bivens, K. A., Patrick, C. W. & Schmidt, C. E. Photocrosslinked hyaluronic acid hydrogels: Natural, biodegradable tissue engineering scaffolds. *Biotechnology and Bioengineering* **82**, 578-589, doi:10.1002/bit.10605 (2003).
- 3 Collins, M. N. & Birkinshaw, C. Investigation of the swelling behavior of crosslinked hyaluronic acid films and hydrogels produced using homogeneous reactions. *Journal of Applied Polymer Science* **109**, 923-931, doi:10.1002/app.27631 (2008).
- 4 Kottapalli, A. G. P. *et al.* Nanofibril scaffold assisted MEMS artificial hydrogel neuromasts for enhanced sensitivity flow sensing. *Scientific Reports* **6**, doi:10.1038/srep19336 (2016).

List of Abbreviations

MRI	Magnetic Resonance Imaging
PET	Positron Emission Tomography
CAs	Contrast Agents
Gd	Gadolinium
Gd-DTPA	Gd – diethylenetriaminepentacetate
GdCl₃	gadolinium chloride
SPIO	superparamagnetic iron oxide
FDA	Food and Drug Administration
NPs	Nanoparticles
HA	Hyaluronic Acid
DVS	Divinyl Sulfone
HANPs	Hyaluronic Acid Nanoparticles
cHANPs	crosslinked Hyaluronic Acid Nanoparticles
HFF	Hydrodynamic Flow Focusing
PEG	poly(ethylene glycol)
DLS	Dynamic Light Scattering
PDI	Polydispersity
FE – SEM	Field Emission - Scanning Electron Microscopy
TEM	Transmission Electron Microscopy
STED	Stimulated Emission Depletion
FR²	Flow Rate Ratio
C_{HA}	Hyaluronic Acid concentration

C_{CA}	Contrast Agent concentration
C_{DVS}	DVS concentration
wt/v	weight/volume
v/v	volume/volume
ICP-MS	Induced Coupled Plasma mass spectrometry
HLB	Hydrophilic-lipophilic balance
PBS	Phosphate-buffered saline
HPLC	High-performance liquid chromatography
HA-SH	Hyaluronate Thiol
PEG-VS	poly(ethylene glycol) – vinyl sulfone
EDC	1-Ethyl-3-(3-dimethylaminopropyl)-carbodiimide
NHS	N-hydroxysuccinimide

Communications to Congress/Conferences:

- “*Comparison of Engineered Nanostructures for Multimodal In vivo Imaging*” **Poster session** at 4th International Conference on Nanotechnology in Medicine. Warsaw, Poland. 7-9 November 2016
- “*Microfluidic Platform to design crosslinked Hyaluronic Acid Nanoparticles for application in MRI modality*” **Oral presentation** at 4th International Conference on Nanotechnology in Medicine. Warsaw, Poland. 7-9 November 2016
- “*Comparison of Engineered Nanostructures for Multimodal In vivo Imaging*” **Poster session** at European Foundation for Clinical Applications CLINAM. Basel, Switzerland. 26-29 June, 2016
- “*Microfluidic Platform to design crosslinked Hyaluronic Acid Nanoparticles for enhanced MRI*” **Oral presentation** at European Foundation for Clinical Applications CLINAM. Basel, Switzerland. 26-29 June, 2016
- “*Microfluidic platform to entrap Gd-DTPA in crosslinked Hyaluronic Acid nanoparticles for enhancing MRI sensitivity*” **Poster session** at V Congress GNB Gruppo Nazionale Bioingegneria. Napoli, Italy. 20-22 June, 2016.
- “*Modulation of hydrogel nanostructures confining Gd-DTPA by a microfluidic flow focusing approach to improve MRI signal*” **Poster session** at European Materials Research Society EMRS Lille, France. 2-6 May, 2016

- “*Design of nanostructures to improve properties of paramagnetic contrast agents*” **Poster session** at 3rd International Conference on Nanotechnology in Medicine. Manchester, UK. 23-25 November, 2015
- “*Micro-and Nano-fluidics for Biomedical Applications*” **Poster session** at ITN SNAL Summer School on Biomaterials, Cell Membranes and Lipid Bilayers (24 July - 2 August 2015) Roccalumera (Sicily), ITALY
- “*Design of nanostructures to improve properties of paramagnetic contrast agents*” **Poster session** at 3rd International Conference on Nanotechnology in Medicine. Manchester, UK. 23-25 November, 2015
- “*Design of novel carriers to improve properties of paramagnetic contrast agent*” **Poster session** at Applied Nanotechnology and Nanoscience International Conference (ANNIC). Parigi, France. 5-7 November, 2015

Publications along three years

- Patent PT150265 “*Un processo di preparazione di nanoparticelle utili come agenti di contrasto nella risonanza magnetica per immagini*”. (December 2015). Extension to International patent on December 2016.
- Russo, M. et al. “*A Microfluidic Platform to design crosslinked Hyaluronic Acid Nanoparticles (cHANPs) for enhanced MRI*”. Sci. Rep. 6, 37906; doi: 10.1038/srep37906 (2016)
- Ponsiglione, A., Russo, M., Netti, P. & Torino, E. “*Impact of biopolymer matrices on relaxometric properties of contrast agents*”. Interface Focus 20160061, doi: <http://dx.doi.org/10.1098/rsfs.2016.0061>(2016).
- Russo, M., Bevilacqua, P., Netti, P., Torino, E. Autocommentary to “*A Microfluidic Platform to design crosslinked Hyaluronic Acid Nanoparticles (cHANPs) for enhanced MRI*”. Molecular Imaging. 2017
- Russo, M., Ponsiglione, A., Forte, E., Netti, P. & Torino, E. “*Hydrodenticity to enhance relaxivity of Gd-DTPA within crosslinked Hyaluronic Acid Nanoparticles (cHANPs)*.” Under Revision (2017).
- Russo, M., Netti, P. & Torino, E. “*PEGylated crosslinked Hyaluronic Acid nanoparticles (cHANPs) designed through a microfluidic platform for nanomedicine*”. Under revision (2017).
- Russo, M., Netti, P. & Torino, E. “*Gd-DTPA loaded cHANPs for enhanced in vitro and in vivo MRI analysis*”. Under preparation (2017).

Publications

- Russo, M., Netti, P., Torino. “A *Microfluidic Platform to design hydrogel nanoparticles for MRI*”. JOVE Video Journal. Under preparation 2017

Project Activities

This Research activity has been partially developed in the framework of the projects:

- "BERSAGLI - Bersagli, sonde e segnali in terapia diagnostica" financed by POR Campania 2007/2013 Obiettivo Operativo 2.1 - BANDO PER LA REALIZZAZIONE DELLA RETE DELLE BIOTECNOLOGIE IN CAMPANIA (2014- 2016).
- "CeSMemo - PONa3_00173". Project contributed to the development of biomedical products, in particular of novel nanosystems for diagnostics and therapy. (June 2014 – December 2016)

Collaborations

- IRCCS SDN Gianturco Street, 113 -80143-Naples.

In vivo MRI analysis are performed in the Diagnostic Center, SDN, Diagnostics and Nuclear Research Institute, that it is an integrated group of specialist clinics in the diagnostic laboratory and imaging.

Other Activities

This microfluidic technology, developed during the Ph.D. course, has been patented (Patent PT150265) and presented as a business idea entitled “KYME”, leading to several awards.

- Award at StartCup Campania with the project “KYME”, Regione Campania, Naples. (October 2016)



KYME: First classified in Bio&Nano category

***KYME** is a spin-off project of the “Center for Advanced Biomaterials for Healthcare” of Istituto Italiano di Tecnologia (IIT) of Naples in collaboration with the University of Naples “Federico II”.*

The project aims to produce injectable medical devices for Magnetic Resonance Imaging (MRI). Using nanotechnology, KYME aims to improve clinically used Contrast Agents (CAs) and to ensure a more effective early diagnosis, thus contributing to the improvement of diagnostic Imaging.

Public Links to media reporting about KYME:

<http://openinnovation.startupitalia.eu/55278-20170311-bioupper-kyme-esami-meno-tossici-piu-dettagliati>

<http://mobile.ilsole24ore.com/solemobile/main/art/impresa-e-territori/2017-02-27/digitale-campania-rincorre-223212.shtml?uuid=AEsYJSe>

<http://www.ilmattino.it/innovazione/biotecnologie/bioupper-team-campano-kyme-migliori-idee-business-nanotecnologia-diagnostica-medica-2279797.html>

<http://www.rainews.it/dl/rainews/TGR/basic/PublishingBlock-d2203e2e-1690-4898-839d-f712cdab8eb1.html>

<http://ildenaro.it/impres-e-mercati/168-impres-e-mercati/79240/kyme-il-team-campano-tra-i-10-progetti-in-finale-a-bioupper>

<https://biomedical.closeupengineering.it/startup-kyme-crea-contrasto-per-rmn/8881/>

<http://ingegneriabiomedica.org/news/diagnostica/startup-campania-2016-la-diagnostica-medica-trova-nuova-luce-grazie-kyme/>



It is

all

in the
detail



- Participation to Premio Nazionale Innovazione PNI. (November 2016)
<http://www.pni2016.unimore.it/>

- Attendance at Bioupper Startup Accelerator, Milan.
 - First selection (21 June – 16 October 2016)
 - Training Week (12-17 December 2016)
 - Acceleration Program (26 January – 6 April 2017)
 - Award Ceremony (12 April 2017)<http://www.bioupper.com/news/selezionati-10-progetti-accedono-finale.shtml>

- Elevator pitch to event “Unione Centenario Industriali”. (February 2017).